COMPUTATIONAL ANALYSIS OF FLUID STRUCTURE INTERACTION IN ARTIFICIAL HEART VALVES

by

Han Hung Yeh

B.A.Sc., The University of British Columbia, 2011

A THESIS SUBMITTED IN PARTIAL FULFILLMENT OF

THE REQUIREMENTS FOR THE DEGREE OF

MASTER OF APPLIED SCIENCE

in

THE FACULTY OF GRADUATE AND POSTDOCTORAL STUDIES

(Biomedical Engineering)

THE UNIVERSITY OF BRITISH COLUMBIA

(Vancouver)

August 2013

Abstract

The development of heart valve stenosis and sclerosis can lead to the development of fatal complications such as congestive heart failure. Therefore, severe valve stenosis requires a surgical operation with artificial heart valve replacement. Given that the geometrical differences between artificial valves would significantly influence hemodynamic performance around the implanted valve, additional knowledge for the interactions between blood flow and the artificial valve is necessary. Therefore, in order to proceed, this study proposes an advanced computational fluid dynamics (CFD) simulation using a fluid-structure interaction (FSI) technique to investigate artificial valve leaflet motion under different physiological conditions.

Among various FSI technique, it is proposed to simulate the motion of the artificial heart valve with a fully-coupled algorithm and arbitrary Lagrangian-Eulerian formulation (ALE) using a monolithic solver. Models are constructed using a realistic aortic root for both the bileaflet and bioprosthetic valves with additional modifications and considerations for the flexible arterial wall. Normal physiological blood pressure and conditions are used to simulate healthy scenarios, which are compared with experiments. Validation is conducted by analysing particle image velocimetry (PIV) experimental data from ViVitro Lab. Hemodynamic performance analyses are conducted and found that both velocity and maximum von Mises stress are higher if calculated using a rigid wall model. The leaflet dynamics, on the other hand, is relatively the same for rigid or flexible wall model. Clinically relevant scenarios are also simulated for both mechanical and bioprosthetic valves. The clinical focus for the mechanical valve is on the malfunction of the valve due to leaflet restrictions. In addition, the clinical focus for the bioprosthetic valve is on the systolic deficiency due to different tissue properties.

Preface

The thesis was prepared under the supervision and guidance of Dr. Dana Grecov, who provided the research topic of simulating artificial heart valve hemodynamics with advanced computational methods.

Dr. Satya Karri (ViVitro Lab, Inc.), provided supervision and guidance for the information regarding to artificial heart valve.

A section of Chapter 2 and a section of Chapter 3 was presented at the 36th Annual Conference of the Canadian Medical and Biological Engineering Society (CMBES36) jointed with l'Association des physiciens et ingénieurs biomédicaux du Québec (APIBQ42). A paper was written for the conference and an additional publication invitation was offered by the Journal of Medical and Biological Engineering.

A version of Chapter 3 and the validation section of Chapter 2 will be submitted for publication.

Table of Contents

List of Tables

List of Figures

Glossary

CFD   Computational fluid dynamics

FSI   Fluid-structure interaction

DNS   Direct numerical simulation

ALE   Arbitrary Lagrangian-Eulerian formulation

PIV   Particle image velocimetry

FDA   U.S. Food and Drug Administration

RANS   Reynolds-average Navier-Stokes

Acknowledgements

I would like to express my most sincere gratitude and appreciation to my supervisor Dr. Dana Grecov for offering me the chance exploring and extending my interesting in biomedical research. Additional thanks to Dr. Grecov for her patiently guidance and support throughout the whole project.

Additional sincere gratitude and appreciation to Dr. Satya Karri, the Director of ViVitro Lab, for the guidance regarding to the computational simulation on artificial heart valves. Dr. Karri also offered insightful comments and technical information on artificial heart valve assessments.

Additional appreciation to ViVitro Lab Inc. for the initiation and the collaboration of artificial heart valve research.

I would like to express my appreciation to my thesis committee members Dr. Hongshen Ma and Dr. Robert Rohling for their time and advice.

The experimental data is kindly provided by ViVitro Lab Inc. and The University of Victoria for bileaflet mechanical valve verification and validation.

To my family and friends for their endless support

Chapter 1

Introduction

The primary function for cardiovascular system is to transport nutrient and waste throughout the body via blood vessels with a continuously pulsing pump-the heart. On average, assuming a constant heart rate of 72 beats per minute, the heart would pulse roughly 2.65 billion times when one reached an age of 70 years old. Given the functional importance of the heart, a surgical operation, either conventional or interventional cardiology, would typically require for a patient with cardiovascular disease, especially if the disease is related to the heart valve. According to Rizzoli et al., the overall survival rate for patients who received an artificial valve replacement drop from 75% to 29% at year 5 to 25, respectively[1]. They further found that with a total number of 3014 operations, there were approximately 11% (334 operations) of the cases belong to reoperations. Among the 11% of reoperations, there were approximately 75.1% (251 operations) were due to mechanical valve malfunction[1]. Furthermore, inspecting a series of data retrieved from U.S Department of Health & Human Service, Agency for Healthcare Research and Quality, that the U.S national heart valve procedures during the past decade have revealed a steady increase in number of patient discharged, shown in Figure 1.1; therefore, an improved understanding of artificial heart valve hemodynamic is beneficial for future studies.

US National Heart Valve Procedure Total Number Discharged
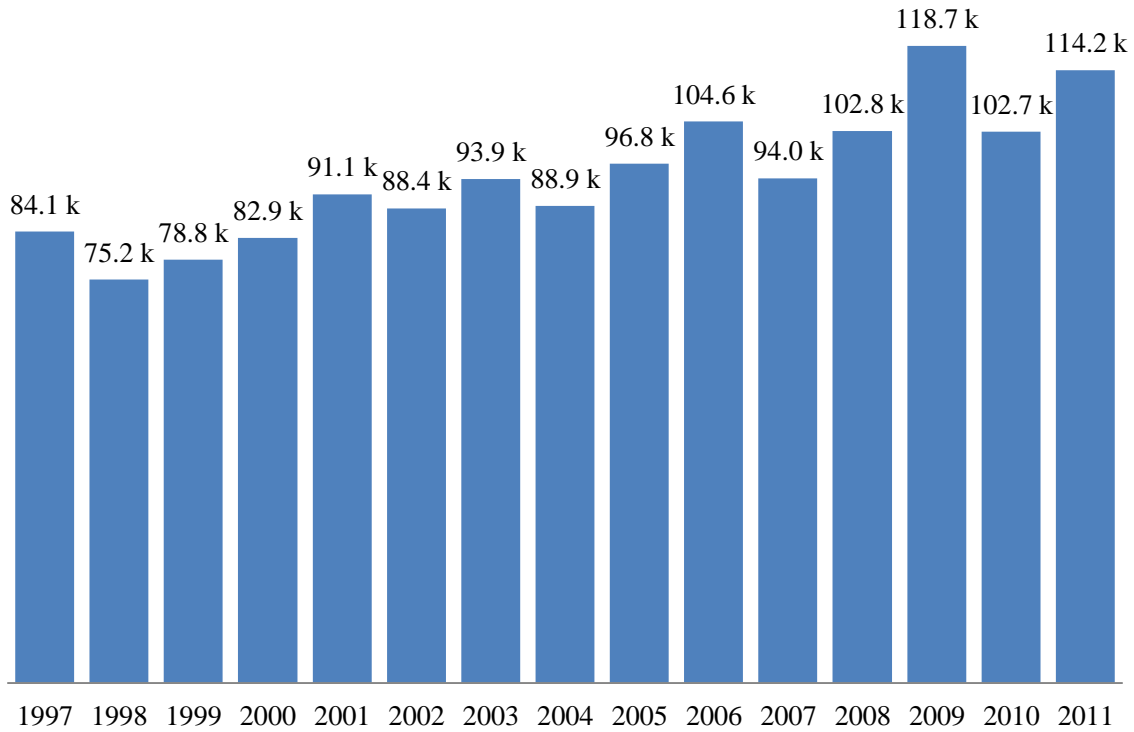
Figure 1.1 Total Number of Discharges for U.S National Heart Valve Procedure from 1997 to 2010

1.1 Background

During clinical practices, a patient would require to undergo an iterative selection process with both the surgeon and the cardiologist in order to determine the appropriate type of implants for artificial heart valve replacement. The selection procedure is heavily depended on the patient's physical conditions such as anatomy, drug intake, or age. The following two sections briefly present the background information regarding to heart anatomy and artificial heart valve implants.

1.1.1 Anatomy and Physiology

The heart is located within thoracic cavity, between the lungs and enclosed by pericardial sac. The heart is divided into four chambers: the left atrium, the left ventricle, the right atrium and the right ventricle. There are four valves within the heart, each serves the common function to maintain unidirectional flow and prevents back flow of the blood, shown in Figure 1.2. Since the contraction of left ventricle would produce greatest blood pressure in order to send the blood into ascending aorta through aortic valve, it would be the primary selection to investigate aortic heart valve hemodynamic and valve performance. There are usually three leaflet cusps that made up of aortic valve: the left and right coronary cusps and the non-coronary cusp. The junction between the leaflet cusps and left ventricle is known as annulus, which is made of fibrous tissue. Several major complications that may lead to heart valve failures are aortic stenosis, valve leaflet calcification, or regurgitation.
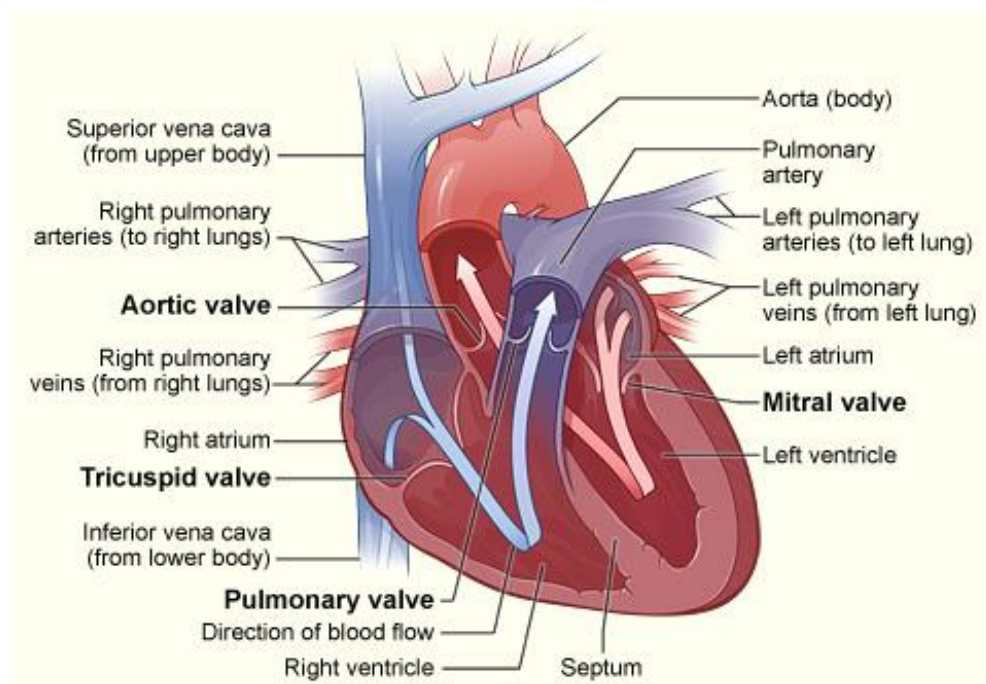
Figure 1.2 Cross Sectional Anatomy of the Heart[2]

1.1.2 Types of Artificial Heart Valve

There are multiple approved products for artificial heart valves due to different design philosophies, including maximizing durability or performance, or minimalizing damage done to blood tissue. The following three sub sections are going to discuss briefly on artificial valves based on three main categories.

1.1.2.1 The Mechanical Valve

Since the first ball and cage mechanical valve was successfully replaced the aortic valve affected by aortic stenosis performed by Dr. Harken in 1960, the development of artificial heart valve has accelerated due to the invention of the heart-lung bypass machine and created more than 70 different prosthetic valves[3]. An artificial mechanical valve is typically comprised of three main parts: a suturing ring for securing the artificial valve to annulus, a set of valve leaflet for preventing reversed blood flow, and a control mechanism for controlling the motion of the valve leaflet, such as shown in Figure 1.3. Besides the early design of ball and cage mechanical valve, there are two major types of valve introduced into market: tilting disk mechanical valve and bileaflet mechanical valve.

Since the mechanical heart valves have superior life expediency and the risk for structure failure, the mechanical heart valve remained one of the selections for valve replacements [3][4][5]. However, several regions of mechanical heart valve are known to have stagnant blood flow that may be the site that originated thrombosis. This is the primary reason for patients receiving artificial mechanical valve to take anticoagulation medications for the rest of their life[3][4][6][7]. Moreover, hinge mechanisms of the mechanical heart valve have also been investigated and found to be prone for thrombosis and may require further improvements; therefore, the development of an artificial heart valve that could mimics the native heart valve without the increase of thrombogenic risk is considered as an alternative approach[3][4].

Figure 1.3 Commercially Available Bileaflet Mechanical Heart Valve[8]

1.1.2.2 The Bioprosthetic Valve

As the desired approach is to replace the diseased valve with one that mimics the native valve, a Ross procedure could be performed using autograft pulmonary valve in order to replace the diseased aortic valve and followed by another allograft procedure to replace the transplanted pulmonary valve. Although it is concluded that the Ross procedure has a low risk for thrombosis and endocarditis while maintaining a high survival rate, the necessity of reoperation limits the technique to younger patients[9]. A bioprosthetic aortic valve, as one of the alternative, is usually constructed with animal pericardium and developed for superior hemodynamic, such as shown in Figure 1.4. Due to the same trileaflet geometry from native aortic valve for the bioprosthetic aortic valve, the improvements in hemodynamic performance could be simply depended on minor design modifications of the commissure between each model. However, given that a bioprosthetic valve has superior hemodynamic performance than mechanical valves, the mortality rate is higher for patients who received a bioprosthetic valve[10][11]. The primary cause for a bioprosthetic valve failure or reoperation is due to structure deterioration, which might be caused by the decellularized valve leaflet under cyclic loading[5][10][12]. Therefore, the bioprosthetic valve is often selected for patients who are older given its outstanding hemodynamic performance without the requirement of

5

antithrombotic therapy even though the overall durability is less than mechanical valve[6][10].

Figure 1.4 Commercially Available Bioprosethetic Tissue Valve[13]

1.1.2.3 The Transcatheter Valve

Provided that both mechanical valves and bioprosthetic valves would require an open heart procedure in order to replace the diseased valve, there are numerous patients who cannot proceed with an open heart surgery due to a relatively high or prohibitive surgical risk. The transcatheter valve, a newly developed interventional cardiology technique that adopted from stents, delivers the bioprosthetic valve to the diseased valve through a catheter in order to restore valve function[14][15]. A transcatheter valve would comprise the same components with a bioprosthetic valve with the exception that the suturing ring from bioprosthetic valve is replaced with a stent frame, such as shown in Figure 1.5. Given that the transcatheter valve is mainly deployed to patients with high risk of surgery, such as elderly patients with an increased risk, the clinical data and outcome available is limited. However, it is concluded that the short term result after the implementation of transcatheter aortic valve has shown to improve and maintain aortic valve function[16].

Figure 1.5 Commercially Available Transcatheter Aortic Valve[17]

1.2   Literature Review

To investigate a biomedical engineering problem, one typical method is to conduct controlled physical experiments while another approach is to conduct numerical experiments. Given that both methods would mimic one or more physiological conditions of human anatomy and physiology, the benefit of a physical experiment is that the result could easily be verified and validated compare with a real world scenario at a cost of experimental repeatability. Numerical experiment, on the other hand, may not easily be verified and validated; however, it benefits from identical experimental conditions and potential optimization by controlling the model parameters. Since flow around heart valve has complex behaviour that would depend on multiple testing conditions such as flow pressure and surrounding geometry, the following three sections are going to review briefly on the numerical methods for heart valve simulations with a focus on aortic valve, which is the valve with the most common valvular disease[18].

1.2.1 Clinical Evaluation on Aortic Stenosis and Artificial Heart Valve

The Gorlin equation, introduced by Gorlin and Gorlin in 1951, has been used in clinical practice for the evaluation of effective orifice area (EOA) [19]. The EOA is a quantity relating pressure gradient and volumetric flow rate for the estimation of heart valve efficiency [19]. The use of EOA is to estimate the effective area where heart valve opened during systole to assess aortic stenosis. Since Gorlin equation, shown in Eq 1 − 1, is derived from Bernoulli equation, additional assumptions and modifications are made in order to improve the accuracy[20][21][22][23][24].

$$EOA = \frac{Q_{mean}}{C \cdot \sqrt{2g} \cdot \sqrt{\Delta p}} \qquad\qquad Eq\ 1-1$$

Where Q_{mean} represents the volumetric flow rate through the orifice created by heart valve, with a unit of centimetre square per minute. Constant C represents the discharge coefficient. The gravitational acceleration, represented by g, has a value of $981\ \frac{cm}{s^2}$. Δp represents the pressure gradient across the valve orifice with a unit of millimeter of water or mercury.

As mentioned above, Gorlin equation provides a crude estimation of heart valve performance based on the volumetric flow rate and pressure gradient across a valve; therefore, in order to obtain additional information to assess valve hemodynamics, such as flow velocity or shear stress distribution, a more advanced model, such as Navier-Stoke equations, should be applied.

1.2.2 General Computational Fluid Dynamics for Artificial Heart Valve

With the dramatically improvements in computational power for current devices, several researches have investigated the hemodynamics around bileaflet mechanical valve intensively using computational fluid dynamics (CFD). Given this increase in computational resources, the construction of an advanced heart valve model for evaluating the hemodynamic performance could be achieved with the use of

computational codes. Provided with the high feasibility of solving relevant parameters for the hemodynamic performance of whole flow domain around heart valve, a well-established software could potentially replace the use of Gorlin equation as standard evaluation. Furthermore, with customizable and parameterizable CFD software, the computational modeling may be used to evaluate the hemodynamics on specific prototypes or patients. The outcomes of such computations are that the results could potentially be used as an assessment for U.S. Food and Drug Administration (FDA) pre-market evaluation. Therefore, the general approaches and advanced methods for CFD for both mechanical and bioprosthetic valve are going to be discussed briefly in the following two subsections.

1.2.2.1 Laminar and Turbulent Model

Since the leaflet motion of artificial heart valve is highly depended on blood flow, various CFD simulations may be conducted based on different phases of the valve motion such as fully closed, opening, fully opened, and closing phase. Depending on the scope of the problem investigated, a simulation that assumed a fully opened valve leaflets may be conducted in order to determine shear stress generated throughout a cardiac cycle[25][26][27][28][29]. More specifically, Grigioni et al. investigate a three dimensional laminar pulsatile flow integrated with a fully opened bileaflet mechanical valve and a realistic aortic root; however, the computational period only covers a portion of systolic cycle until peak systole[25]. Hsu, on the other hand, conducts a three dimensional Reynolds-average Navier-Stokes (RANS) using the two-equation k-ε turbulent model and concludes that wall shear stress significantly decrease with a modified suturing ring[28]. Moreover, Sirois and Sun conduct k-ε turbulent model for a fully opened bioprosthetic valve to evaluate the platelet activation due to shear stress[29]. Finally, Sun et al. investigate transcatheter valve deformation and distortion with a steady back flow, which applies to a fully closed valve with rigid wall assumption[30]. Although the flow around artificial valve might enter from transition to turbulent regime under high pressure gradient, a laminar or turbulent model would provide estimation on flow properties such as flow velocity and shear stress.

1.2.2.2 Direct Numerical Simulation Model

Given that the laminar model can accurately compute solutions for the overall hemodynamics within the domain, the model has only minor ability to capture and predict small scale vortices generated by transition flow. In addition, the existing turbulent model would result in an averaging of the fluctuations and loss of transition flow information; therefore, the alternative for simulating complex hemodynamics would be using direct numerical simulation (DNS) in order to capture flow vortices and fluctuations. The main differences between a laminar model and a DNS model are the scales for time and length such that a DNS model would significantly increase computational resource required by refining the distribution of allowable mesh and time step. Dasi et al. preform a three dimensional DNS with physiological conditions and validated against experiments using particle image velocimetry (PIV) for bileaflet mechanical valve [31]. Their DNS results have revealed flow instability and vortex streets during flow acceleration and peak systole while the deceleration phase showed a diminishing of coherent structures. However, with their leaflet dynamics approximated using probability density function that is determined and analysed from experiments for the entire cardiac cycle, the interactions between valve leaflets and surrounding flow remain open to uncertainty[31].

1.2.3   Advanced CFD with Fluid Structure Interaction Method

As mentioned above, neither laminar, turbulent, nor DNS model along could resolve the uncertainty regarding to interactions between artificial valve leaflet and surrounding fluid. Therefore, an advanced fluid structure interaction (FSI) method should be applied to general CFD algorithm to address the needs for precise interactions between different physical boundaries within domain. With the addition of FSI to general CFD algorithm, it is possible to compute leaflet motion and deformation based on the solution from fluid domain within the same time step. The following two subsections are going to discuss different approaches for conducting FSI simulations.

1.2.3.1 Fixed and Moving Mesh

For a fluid problem, the computational domain is typically described with Eulerian method for the motion of fluid; therefore, the mesh for fluid domain is fixed. Whereas the structural problem requires the computational domain to move with the motion and deformation of the structure; hence, the Lagrangian method is applied such that the mesh can be moved due to structure motion. Since the fixed mesh method does not require remesh and mesh refinement and that the method is able to handle large structure displacement, the fixed mesh method has been adopted by several researchers for conducting FSI simulation on artificial heart valve[32][33][34][35][36]. However, since the fluid domain has a fixed background mesh while structure domain is on a separate grid, it is necessary to have high mesh resolution in order to produce an accurate simulation. On the other hand, moving mesh method, also known as Arbitrary Lagrangian-Eulerian formulation (ALE) , ensures a higher solution accuracy due to simultaneous boundary displacement for both fluid and structure domain[32]. Although, ALE method might require conducting mesh reconstructions during the simulation in order to maintain high mesh quality with higher computational cost and difficulty[32]. Due to higher accuracy with the application of ALE, researchers have adopted this method to solve FSI problems around the artificial bileaflet mechanical heart valve[37][38][39][40][41][42][43] and address different clinically relevant issues such as thrombogenic performance[38], experimental validation[39], and subaortic stenosis[41]. A few researchers also apply the ALE methodology and target computational problems related to bioprosthetic tissue valve[44][45].

1.2.3.2 Partitioned and Monolithic Solver

In terms of solver options, partitioned approach[37]-[45] is widely used in literature since the solver computes the solution for fluid and structure separately, which could be further differentiated into strong coupled and loose coupled methods. The benefit of applying partitioned approach is that the computational cost could potentially decrease depending on the coupling method of the solver[32]. Specifically, a loose coupled partitioned solver

only required one iteration per time step using the solution from previous time, which solves the FSI boundary explicitly. The strong coupled partitioned solver solves FSI boundary implicitly using the solution at current time step, which might require more sub iterations in order to achieve a converged solution[32]. The partitioned approach, either explicitly or implicitly coupled, however, could create solver instability; therefore, it is required to introduce a relaxation factor to stabilize the solver for convergence. Furthermore, the stability is depended on the level of interaction between fluid and structure boundary. It is possible for a high level of sensitivity for interaction boundary that neither strong coupled nor loose coupled method could achieve a converged solution, which also depended on the relaxation factor[32]. The monolithic approach solves the entire problem at one single time step within one solver, which avoid stability issue created by partitioned solve. The computational cost and accuracy for monolithic approach, compare with partitioned approach, is higher due to a unified algorithm that solve the entire system simultaneously; thus, the approach is less attractive[46].

1.2.4 Summary of Gaps in Existing Knowledge

Table 1.1 Summary on Current Computational Methods Applied to Artificial Heart Valve

Computational Techniques	Method / Mesh / Solver	Rigid Wall Assumption				
		Fluid	Fluid-Structure Interaction			
			Fixed		ALE	
			Monolithic	Partitioned	Monolithic	Partitioned
Mechanical	Laminar	√		√		√
	Turbulent	√				
	DNS	√		√		√
Bioprosthetic	Laminar	√		√		√
	Turbulent	√		√		
	DNS					

As discussed previously, several improvements could be made in order to model the hemodynamics of heart valves more accurately. The possible improvements for the simulation of heart valve can be summarized as follows:

- Simulation methods refinement

  With current computational methods summarized in Table 1.1, overall progress on the simulations of heart valve hemodynamics has showed that the main computational solver applied is the use of partition solver. However, the partitioned solver requires a delicate configuration in order to maintain solver stability. The monolithic solver, although is more accurate and stable, is not commonly used due to higher computational resource requirement.

- Complete cardiac cycle

  Given that there is large difference between the aortic and ventricular pressure across a heart valve during one cardiac cycle, an accurate and repeatable solution might not always available. Therefore, simulations on partial cardiac cycle, either systole or diastole, are often conducted given the large pressure difference.

- Flexibility of arterial wall

  The modeling focus of flexible arterial wall using FSI methods is on the investigation of arterial aneurysm or ventricular compression, the complex interactions between blood, heart valve, and arterial wall are not considered[50][51]. Specifically, the modeling of artificial valve hemodynamic performance using FSI technique assumes the surrounding arterial wall to be rigid[33]-[45].

- Clinically relevant problems

  Complications, such as leaflet malfunction or calcification, could be investigated based on the modification of existing models. Given that additional information will be available after a FSI simulation is conducted; physical parameters that have effects on the artificial valve hemodynamic performance can be evaluated.

1.3   Proposed Study

Given that ViVitro Lab., our collaborator who is specialized in third party testing for artificial heart valve manufacturers, is interested in the investigation of numerical experiments on the design parameters affecting the hemodynamic performance of artificial valves, a thorough literature review on state-of-the-art numerical simulation using general CFD and FSI is conducted. With the brief introduction on the current computational methods of artificial heart valve, the proposed study is organized with the following three sections: the motivation, the experimental validation, and the objectives.

1.3.1   Motivation

As previously discussed, numerical experiments could potentially be useful when conducting parameterized experiments with identical testing conditions. Given that simulations conducted with general CFD cannot maintain high accuracy and physical results due to the strong interaction between artificial heart valve leaflet and surrounding fluid, an advanced approach, FSI, should be incorporated. One advantage with the use of FSI is to conduct numerical experiments that could reflect and relate to clinical issues and improve current understanding of problems in different types of artificial heart valves with different causes. Furthermore, different approaches for conducting an FSI simulation have been reviewed without an evidence of accurate and robust modeling for different clinical situations with different artificial heart valves. Therefore, a generalized modeling scheme that could apply to different clinically related problems is necessary. More specifically, the proposed method for conducting hemodynamics studies is based on FSI with ALE and monolithic solver for both mechanical and bioprosthetic valves under laminar assumption. Moreover, with the investigation on the hemodynamics of artificial valve using FSI models, additional needs regarding artificial heart valve assessment using CFD results are proposed by ViVitro Lab. Given that the customizable and parameterizable model will be available, it can be potentially used by ViVitro Lab, the third party evaluation body, and FDA, the regulatory body, as an additional analysis tool for artificial heart valve designs and evaluations.

1.3.2 Experimental Validation

In order to verify and validate the proposed models with simulated results for artificial valve, the FDA standard evaluations on heart valves are conducted at ViVitro Lab Inc. located in Victoria, BC. The experimental apparatus has both aortic and mitral valve implemented with realistic ventricle that controls cardiac output. The verification and validation is conducted with controlled physiological pulse for artificial valves using PIV data acquisition to process flow velocity field.

1.3.3 Research Objectives

The research objectives are listed as follows:

Primary objective: To construct a CFD model using FSI method in order to evaluate the hemodynamics of artificial heart valve in idealized aortic root geometry

Secondary objective: To assess heart valve performance between numerical and experimental result with ViVitro Lab

Tertiary objective: To address clinical concerns with model built in primary objective and numerically experiment the influence of different parameters affecting the hemodynamics across aortic valve

Chapter 2

Generalized Computational Procedure

As discussed previously in the introduction, there are multiple approaches to simulate the hemodynamics of artificial valve with advanced CFD; however, the numerical experiments conducted by different approaches would most likely generate results deviated away from one to another, even with the same numerical approach applied to identical problem. A CFD performance assessment conducted by Stewart et al., researchers from FDA, has revealed the CFD results deviations by different laboratories given that the laboratories have the freedom to select the computational software and methods of own choice[47]. Therefore, this study is using a commercial software package in order to obtain accurate, stable, and repeatable numerical solution with FSI method. Provided that many commercially available software have the potential to obtain accurate and repeatable solution, COMSOL Multiphysics is selected due to its additional flexibility to modify physics and constraints to existing model without comprehensive remodeling while maintain general solver stability and accuracy. The flexibility of COMSOL extends the possibility to integrate additional physics on top of FSI such as thermal analysis, particle tracing, or structure fatigue. These additions, however, are beyond the scope of this study due to problem complexity and resource requirement. Given that the computational software is determined, this chapter is going to discuss the generalized computational models constructed using COMSOL starting with the discussion on geometry, governing equations, boundary conditions, solver configuration, and experimental setup.

2.1 Geometry Parameterization

Given that a three dimensional (3D) computational model was constructed and found that the model would consume the amount of computational resource that was beyond the maximum capability of the current device, the presented work is simplified to a two dimensional (2D) FSI simulation. However, the current 2D FSI model could easily be transformed into a 3D model using more advanced equipment given that all physical and geometrical parameters are maintained. The overall computational domain is modified from the domain published by Choi et al. in 2009 for the FSI simulation of bileaflet mechanical heart valve[43]. In order to parameterize the computational domain, the geometry of the aortic root is firstly established, following with mechanical valve leaflet and tissue valve leaflet declaration.

2.1.1 Fluid Domain and Aortic Wall

The computational domain consists of a pair of artificial valve leaflet and idealized sinuses located at aortic root. Both ventricular entry and aortic exit are assumed to be straight with an entrance length of $16.5\ mm$ and an overall domain length of $75\ mm$. The blood vessel diameter is assumed to be $25\ mm$ such that the computational model would correspond to an artificial valve replacement by a $25\ mm$ St. Jude Medical bileaflet mechanical heart valve. The aortic root has an approximate length of $25\ mm$ with maximum aortic width of $8\ mm$ for each sinus. The outline of aortic sinus is constructed with a rational Bézier curve, which has the general form shown in $Eq\ 2-1$. To construct the aortic root curvature, the quadratic rational Bézier curve is specifically used with three control points, shown in $Eq\ 2-2$.

$$\boldsymbol{b}(t) = \frac{\sum_{i=0}^{j} \boldsymbol{P}_i w_i B_i^j(t)}{\sum_{i=0}^{j} w_i B_i^j(t)} \qquad\qquad Eq\ 2-1$$

$$\boldsymbol{b}(t) = \frac{\boldsymbol{P}_1(1-t)^2 \times w_1 + \boldsymbol{P}_2\big(2t(1-t)\big) \times w_2 + \boldsymbol{P}_3(t^2) \times w_3}{(1-t)^2 \times w_1 + \big(2t(1-t)\big) \times w_2 + (t^2) \times w_3} \qquad Eq\ 2-2$$

Where $B_i^j(t)$ represents the Bézier curve function, t represent a positive number between zero and one in order to generate the path of Bézier curve, $\boldsymbol{P}_i$ represents the control point coordinates, and w_i represents the scalar weight coefficients for all control points.

Table 2.1 Weight Coefficient for Different Curve Profile

Curve Profile	Weight Coefficient		
	w_1	w_2	w_3
Parabola	1	1	1
Circular Arc	1	$\dfrac{1}{\sqrt{2}}$	1
Aortic Root	1	$\dfrac{3}{\sqrt{2}}$	1

By applying Eq $2 - 2$, one could parameterize the aortic root curvature by adjusting the weight coefficient independently for each control point. Summarized as an example in Table 2.1, three different curves constructed with different combinations of weight coefficient are shown. For the case of aortic root curvature, the second control point of the quadratic rational Bézier curve has been shifted proximally to the base of aortic root in order to reconstruct the approximate curvature of sinus. The overall outline of aortic root with ventricular entry and aortic exit are constructed using Bézier polygon, which links all control points with pre-defined Bézier curve to form an enclosed surface. All control points and their own coordinate are presented in Figure 2.1 with dark circles highlight the exact position of the control points.
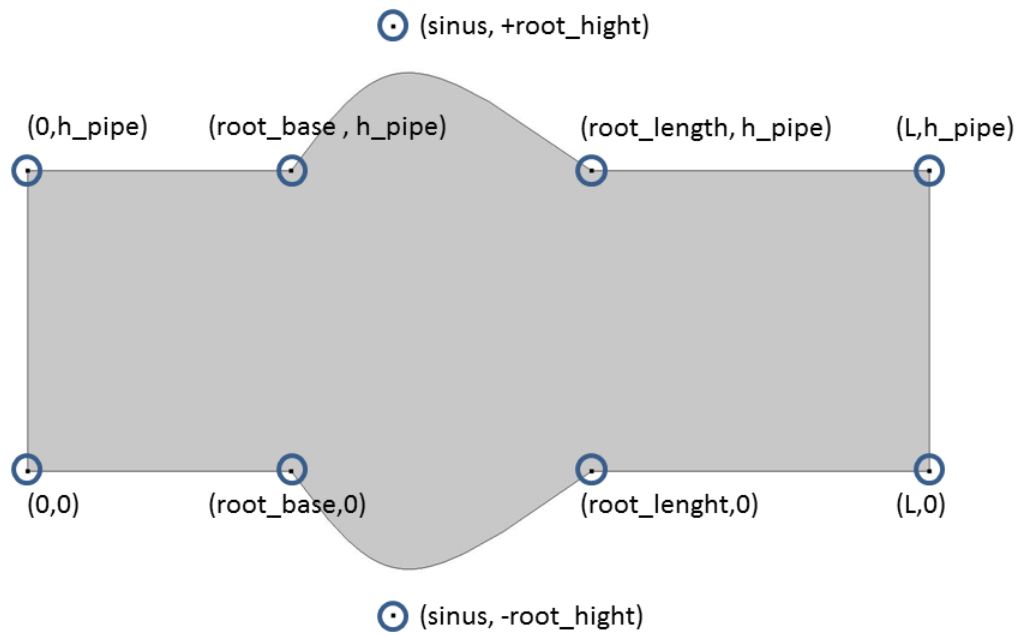
Figure 2.1 Coordinate of All Control Points of Aortic Root by Bézier Polygon

Table 2.2 List of Geometrical Parameter for Aortic Root

Parameter	Value [mm]	Parameter	Value [mm]
h_pipe	25	root_base	22
sinus	30	root_length	50
+root_hight	37	- root_hight	−12
L	75	Wall_thickness	3

The geometrical parameters, which are used to construct the aortic root, are listed in Table 2.2 in millimeter. The value of geometrical parameter for aortic root are expressed as follows: h_pipe represents the diameter of aorta; root_base represents the base of aortic root, which further depended on the position of artificial valve leaflet; sinus represents the horizontal position of the curvature control points; root_lenght represents the average aortic root length; +/- root_hight represent the vertical position of the curvature control points; L represents the overall computational domain length; and wall_thickness represent the average wall thickness of aorta. Together with the use of additional sets of Bézier polygon, the wall thickness of aorta is integrated into the geometry using an average wall thickness of $3\,mm$. The wall thickness of aorta is assumed to be nearly uniform such that all the control point for constructing the wall of blood vessel using Bézier polygon would be simply a vertical translation of all control points outline the aortic root. The finalized computational domain consists of anatomical similar aortic root curvature with a uniform vessel wall thickness in order to conduct FSI simulation without the need to assume rigid blood vessel, shown in Figure 2.2.
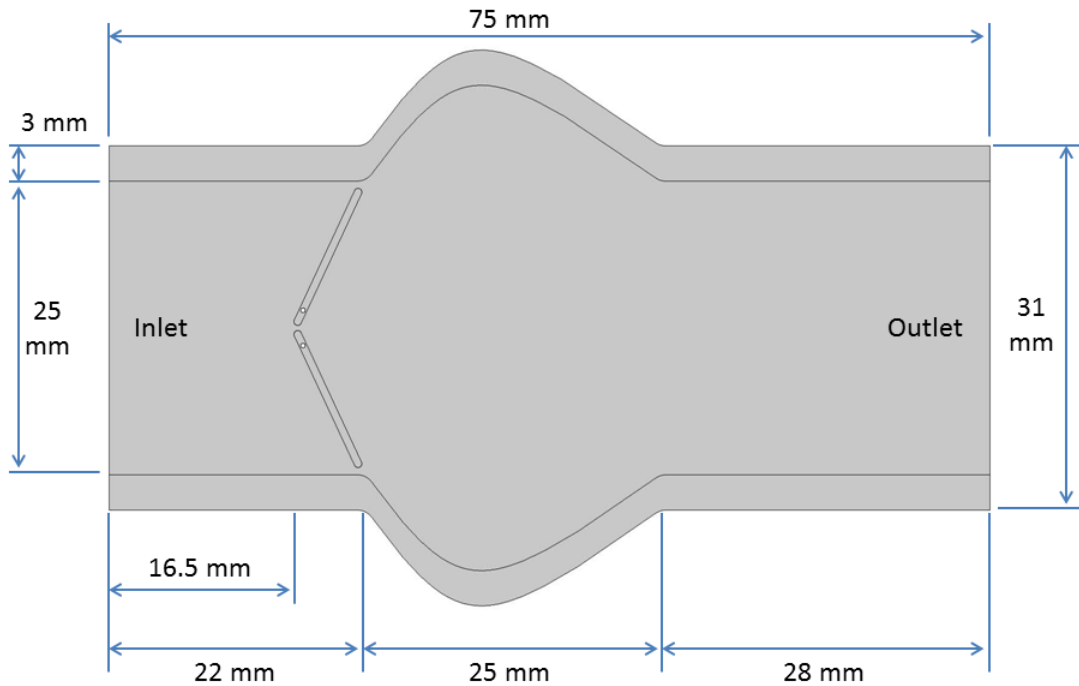
Figure 2.2 Complete Computational Domain for the Simulation of Bileaflet Mechanical Valve

Table 2.3 Material Properties for Computational Domain

Blood	
Density, ρ_{blood}	$1060 \; \dfrac{kg}{m^3}$
Viscosity, μ_{blood}	$0.0035 \; Pa \cdot s$
Aortic Wall	
Density, ρ_{wall}	$1060 \; \dfrac{kg}{m^3}$
Elastic Modulus, E_{wall}	$2 \times 10^7 \; Pa$
Poisson Ratio, ν_{wall}	0.45

With the geometry of aortic root properly parameterized, the material properties for the whole computational domain could be defined. Table 2.3 summarized all the necessary material properties of blood and blood vessel before proceeding to the next simulation step. The properties of blood are assumed to be isothermal and Newtonian with a constant density and dynamic viscosity throughout the cardiac cycle. The properties of aortic wall are assumed to be linear-elastic with an equivalent elastic modulus of $2 \times 10^7 \; Pa$, which accounts for the natural hyper-elasticity of blood vessel.

2.1.2   Mechanical Valve

The primary model of artificial heart valve is chosen to be the bileaflet mechanical heart valve since the mechanical valve remains as the primary surgical option for artificial valve replacement due to superior durability. The parameterization of mechanical valve leaflet starts with identifying the position of valve leaflet hinges. Given the geometrical scale of micro mechanism of mechanical valve hinges, the geometrical and computational complexity would be greatly increased if a geometrical simplification is not applied to the computational domain. Therefore, the hinge of mechanical valve is simplified to a pin hinge from the original butterfly hinge designed for bileaflet mechanical valve in order to avoid singularity due to sharp corners and steep transitions, such as shown in Figure 2.3.
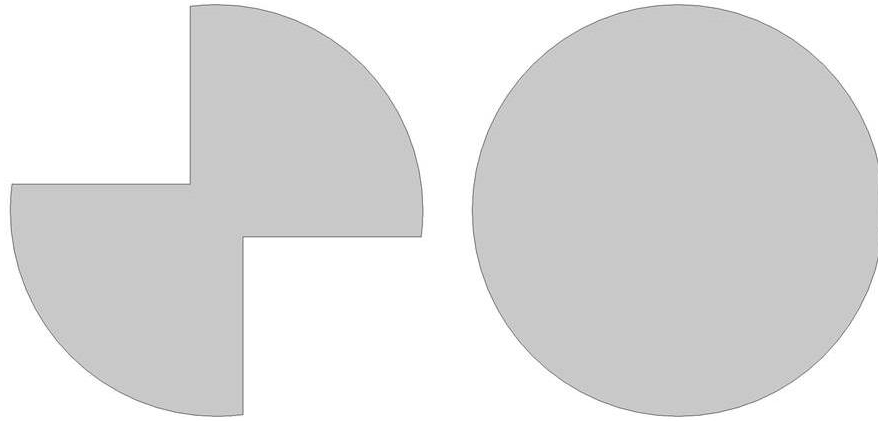
Figure 2.3 Schematic Drawing of Butterfly Hinge (Left) and Pin Hinge (Right)

Table 2.4 Material Properties of Bileaflet Mechanical Heart Valve

Density, ρ$_{mech}$	$2116 \; \frac{kg}{m^3}$
Young's Modulus, E$_{mech}$	$30.5 \times 10^9 \; \frac{N}{m^2}$
Poisson Ratio, ν$_{mech}$	0.3
Yield Strength	$407.7 \times 10^6 \; \frac{N}{m^2}$

The material properties of the bileaflet mechanical heart valve are summarized in Table 2.4. The vertical coordinate of mechanical valve hinges is governed by a fixed distant between two hinges, which is set to be $3 \; mm$ for St. Jude Medical bileaflet mechanical heart valve. The horizontal coordinate of mechanical valve hinges is governed by the physical location of the artificial heart valve implant at the location of aortic valve, which is set to be at the end of ventricular entrance length, $16.5 \; mm$. After the positions of mechanical valve hinges are determined, mechanical valve leaflets can be modeled with the additional information on valve leaflet thickness and length. The St. Jude Medical bileaflet mechanical heart valve has a leaflet thickness of $0.65 \; mm$ and length of

12.8 mm[43]. In order to remove geometrical singularity and improve solver efficiency, the short edges of mechanical valve leaflet are rounded by applying fillet operation with a radius of 0.325 mm, equivalent to half of valve leaflet thickness, to all four vortices that defined the domain of valve leaflet. Finally, the motion of mechanical valve leaflet is restricted with a fully closed angle of 25 degree and a fully opened angle of 85 degree, such as illustrated in Figure 2.4.
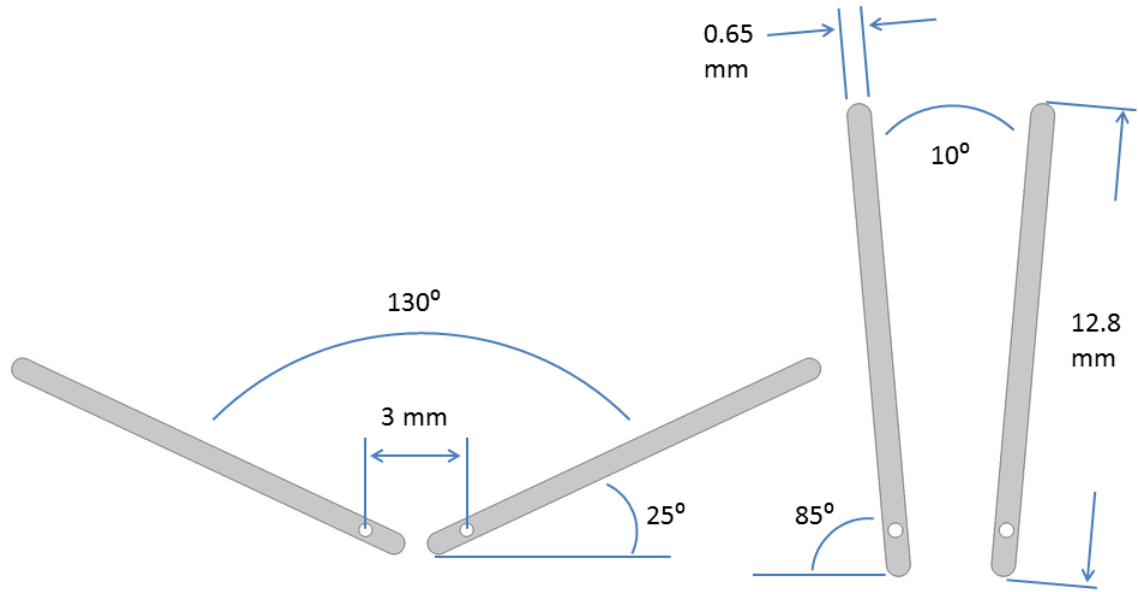
Figure 2.4 Illustration of Leaflet Constraints: Fully Closed Valve Leaflet Position (Left) and Fully Opened Valve Leaflet Position (Right)

Two separate computational domains are established by combining the mechanical valve leaflet model with aortic root model constructed previously. The complete computational domain for mechanical valve is shown in Figure 2.2. Note that when the assumption of rigid wall is applicable, the arterial wall thickness of 3 mm would decrease to 0 mm such that no arterial wall would be presented in rigid wall model.

2.1.3   Bioprosthetic Tissue Valve

The secondary model of artificial heart valve is chosen to be the bioprosthetic tissue valve since the tissue valve is considered as the secondary surgical option for artificial valve replacement due to superior hemodynamic performance. The profile and curvature of tissue valve is determined using Bézier polygon, the same technique used to construct aortic root, with different weight coefficients for the quadratic rational Bézier curve.

Table 2.5 Modeling Parameters for Bioprosthetic Tissue Valve

Density, ρ_{tissue}	$1060 \; \dfrac{kg}{m^3}$
Elastic Modulus, E_{tissue}	$2 \times 10^6 \; Pa$
Poisson Ratio, ν_{tissue}	0.45
Weight Coefficients	$3, \dfrac{1}{\sqrt{2}}, 1$
Leaflet Thickness	$0.4 \; mm$
Elastic Modulus, E_{wall}	$2 \times 10^7 \; Pa$

There are two separate tissue valve models constructed during FSI simulation where one model assumes rigid blood vessel while the other model integrates flexible vessel wall with tissue valve. Given that the modeling parameters are the same for both cases listed in Table 2.5, the only minor difference between the rigid vessel and flexible vessel model is the modification of valve leaflet base connecting to arterial wall. The complete computational domain for tissue valve is shown in Figure 2.5.
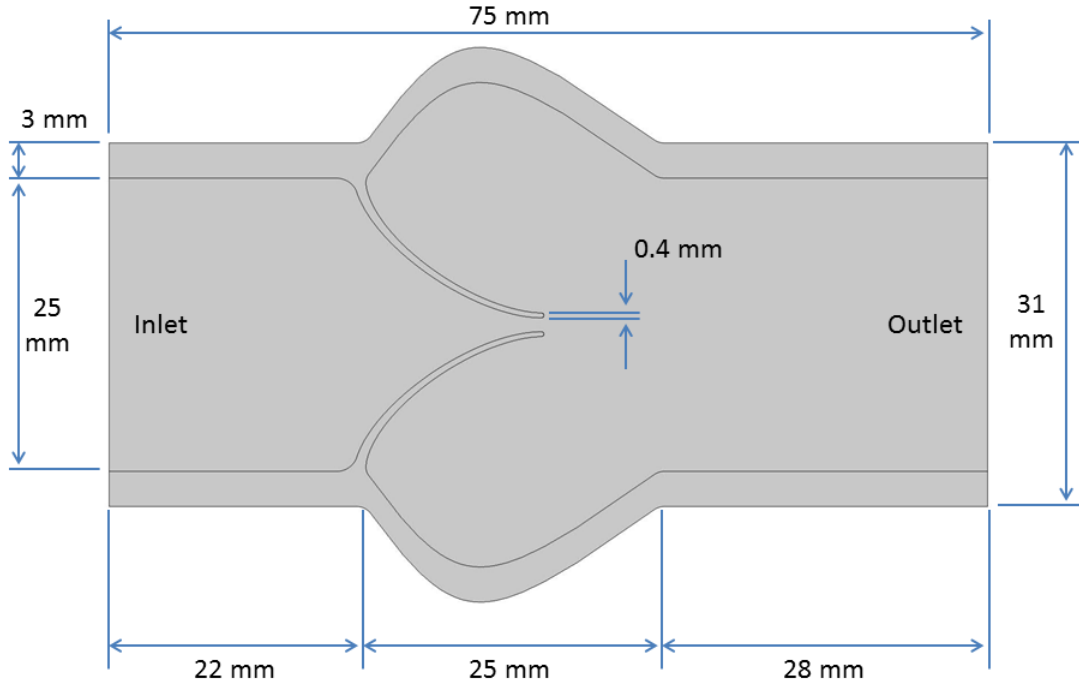
Figure 2.5 Complete Computational Domain for the Simulation of Tissue Valve

2.2   Governing Equations

With the computational domain for both blood and artificial valve leaflet described and established in previous section, the equation of motion for the computational domain would be described in the following three subsections: equations for fluid domain, equations for structure domain, and the equations for coupling both domains.

2.2.1   Governing Equations for Fluid Domain

Although the model for fluid mechanics assumption made by the majority of researchers would be to assume the blood flow in large arteries falls within laminar regime, there are reasonable investigations on artificial valve modeling with the use of different turbulent models, such as k-ε and k-ω[28][29][41][42][43].

The general equation of motion to evaluate the hemodynamics of fluid domain, in three dimension with Cartesian coordinates, are the flow continuity equation, shown in Eq 2 – 3, and the Navier-Stokes equations, shown in Eq 2 – 4 to Eq 2 – 6. For Navier-Stokes equations, the left hand side of the equation is the inertial forces, which is balanced by the right hand side of the equation: pressure force, body force, and viscous force.

$$\frac{\partial u}{\partial x} + \frac{\partial v}{\partial y} + \frac{\partial w}{\partial z} = 0 \qquad\qquad Eq\ 2-3$$

$$\rho\left(\frac{\partial u}{\partial t} + u\frac{\partial u}{\partial x} + v\frac{\partial u}{\partial y} + w\frac{\partial u}{\partial z}\right) = -\frac{\partial P}{\partial x} + \rho g_x + \mu\left(\frac{\partial^2 u}{\partial x^2} + \frac{\partial^2 u}{\partial y^2} + \frac{\partial^2 u}{\partial z^2}\right) \qquad Eq\ 2-4$$

$$\rho\left(\frac{\partial v}{\partial t} + u\frac{\partial v}{\partial x} + v\frac{\partial v}{\partial y} + w\frac{\partial v}{\partial z}\right) = -\frac{\partial P}{\partial y} + \rho g_y + \mu\left(\frac{\partial^2 v}{\partial x^2} + \frac{\partial^2 v}{\partial y^2} + \frac{\partial^2 v}{\partial z^2}\right) \qquad Eq\ 2-5$$

$$\rho\left(\frac{\partial w}{\partial t} + u\frac{\partial w}{\partial x} + v\frac{\partial w}{\partial y} + w\frac{\partial w}{\partial z}\right) = -\frac{\partial P}{\partial z} + \rho g_z + \mu\left(\frac{\partial^2 w}{\partial x^2} + \frac{\partial^2 w}{\partial y^2} + \frac{\partial^2 w}{\partial z^2}\right) \qquad Eq\ 2-6$$

Where ρ represents the density of fluid, u, v, w represents the velocity in x, y, z direction, g_i represents the body force in i-direction, and μ represents the dynamic viscosity of the fluid.

Several assumptions could be made to simplify the fundamental equations in order to approximate flow characteristic of the domain. The assumptions made for blood flow in large arteries are:

- The computational domain is set to be in two dimensional
- The fluid can be approximate to be laminar
- The density of blood is maintained to be constant, incompressible
- The rheological properties of blood are approximated to be Newtonian
- The flow, with natural pulsatile profile, is established to be time dependent
- The body forces, due to a short computational domain of $75\ mm$, could be neglected
- All other fluid properties that might influence the flow, such as temperature dependency, are defined to be constant

With the assumptions to the problem properly defined, the generalized equation of motion can be simplified to Eq 2 − 7 to Eq 2 − 9, shown as follows:

$$\frac{\partial u}{\partial x} + \frac{\partial v}{\partial y} = 0 \qquad\qquad Eq\ 2-7$$

$$\rho\left(\frac{\partial u}{\partial t} + u\frac{\partial u}{\partial x} + v\frac{\partial u}{\partial y}\right) = -\frac{\partial P}{\partial x} + \mu\left(\frac{\partial^2 u}{\partial x^2} + \frac{\partial^2 u}{\partial y^2}\right) \qquad\qquad Eq\ 2-8$$

$$\rho\left(\frac{\partial v}{\partial t} + u\frac{\partial v}{\partial x} + v\frac{\partial v}{\partial y}\right) = -\frac{\partial P}{\partial y} + \mu\left(\frac{\partial^2 v}{\partial x^2} + \frac{\partial^2 v}{\partial y^2}\right) \qquad\qquad Eq\ 2-9$$

The generalized equations shown above represent the Navier-Stokes model for determining flow pressure and velocity with the embedded assumptions that the length scale of the domain should be much greater than the inter molecule distance, which is in the order of 10^{-8} meter, and the time scale of the domain should be much greater than the molecular collision, which is in the order of 10^{-10} s. Fortunately, for the investigation of hemodynamics around aortic valve, the additional assumptions regarding to the length scale and time scale would be satisfied. Given that turbulent model would result in information averaging regarding to vortices generation, the laminar model could be used to if small scale vortices within domain are not the main focus. Although, laminar model could be refined and improved into DNS, Kolmogorov's scales must be followed in order to conduct such simulation. Since DNS would be the alternative for any CFD simulation due to the fact that results from DNS could provide all necessary information for the flow, one limitation of DNS is due to the usage of computational resources, which are heavily depended on Kolmogorov's scales, shown in Eq 2 − 10 and Eq 2 − 11 for Kolmogorov's length scale and time scale.

$$l_k = \left(\frac{v^3}{\epsilon}\right)^{\frac{1}{4}} \approx l_o \times Re_T^{\frac{-3}{4}} \qquad\qquad Eq\ 2-10$$

$$t_k = \left(\frac{v}{\epsilon}\right)^{\frac{1}{2}} \approx t_{LETOT} \times Re_T^{\frac{-1}{2}} \qquad\qquad Eq\ 2-11$$

Where l_k represents the Kolmogorov's length scale, t_k represents the Kolmogorov's time scale, ν represents the turbulent viscosity, ϵ represents the dissipation rate of turbulent kinetic energy, l_o represents the length of eddy turning in flow, t_{LETOT} represents the large eddy turn over time, Re_T represents the turbulent Reynolds number

$$where \; Re_T = \frac{\rho l_o u'}{\mu} \; and \; u' = \frac{l_o}{t_{LETOT}}$$

The feasibility of apply DNS to current study is estimated by evaluating the Kolmogorov's length scale and time scale using Eq 2 – 10 and Eq 2 – 11. To calculate the length scale, the maximum length of eddy turning in flow, l_o, can be approximated to equal the length of the computational domain, as it would be the maximum length an eddy could form for given geometry. To calculate the length scale, the maximum velocity, u', can be approximated to equal the peak velocity during systole, which would be approximately be less than $1.5 \frac{m}{s}$ in average. Given that the density of the blood is $1060 \frac{kg}{m^3}$ and the dynamic viscosity of the blood is defined to be $0.0035 \, Pa \cdot s$, the turbulent Reynolds number can be approximated as follows:

$$Re_T = \frac{\rho l_o u'}{\mu} = \frac{1060 \frac{kg}{m^3} \times 0.075 \, m \times 1.5 \frac{m}{s}}{0.0035 \, Pa \cdot s} = 34071 \approx 3.4 \times 10^4$$

Kolmogorov's length scale can then be approximated as follows:

$$l_k = \left(\frac{\nu^3}{\epsilon} \right)^{\frac{1}{4}} \approx l_o \times Re_T^{\frac{-3}{4}} \approx 0.075m \times (3.4 \times 10^4)^{\frac{-3}{4}} \approx 2.99 \times 10^{-5} m$$

Kolmogorov's time scale can then be approximated as follows:

$$t_k = \left(\frac{\nu}{\epsilon} \right)^{\frac{1}{2}} \approx t_{LETOT} \times Re_T^{\frac{-1}{2}} \approx \frac{0.075m}{1.5 \frac{m}{s}} \times (3.4 \times 10^4)^{\frac{-1}{2}} \approx 2.71 \times 10^{-4} s$$

Using Kolmogorov's length scale, the total number of mesh grid can be approximated if the computational domain is assumed to be a rectangle with dimension of $0.075m \times 0.025m$, which is the length and width of the computational domain shown above. The total number of mesh required of the domain would be:

$$\frac{0.075m}{2.99 \times 10^{-5}m} \times \frac{0.025m}{2.99 \times 10^{-5}m} \approx 2083333 \approx 2.08 \times 10^6 \; mesh \; elements$$

Similarly, the total number of time step can be calculated using Kolmogorov's time scale and the duration of one cardiac cycle of $0.8s$:

$$\frac{0.8s}{2.71 \times 10^{-4}s} \approx 2952 \; steps$$

Based on performance benchmark evaluation on FSI simulation using COMSOL with the geometry shown in section 2.1.2 for the case of mechanical valve without arterial wall, a computational domain, which consists with approximately 50000 mesh elements, would require an average 2 minutes solution time for each time step. Assuming the relationship of time consumed for each time step relative to total number of meshes is linear, a computational domain consists of 2.08×10^6 mesh element would require an average 83 minutes solution time for each time step. With a total number of time step required equals to 2952, the total solution time required to conduct DNS for one full cardiac cycle would be roughly 2.5×10^5 minutes, which is equivalent to 170 days. Although this cost approximation for DNS computational time with FSI is an over estimation due to the maximum Kolmogorov's scales chosen, it is clear that it is not feasible to conduct DNS based on the resource available. Therefore, laminar model with refined mesh distribution would be deployed in order to capture information on vortices as much as possible. Turbulent models, compare with laminar model, would require solving additional equations and consuming extra computational resource for identical mesh distribution. Therefore it was determined to use turbulent models for hypertension flow, which is out of the scope of this project.

2.2.2 Governing Equations for Structure Domain

The structure domain consist a pair of artificial valve leaflet as shown in previous section. The material properties of the leaflet are assumed to be linear elastic for blood vessel wall and for both mechanical valve and bioprosthetic valve. In order to solve for the deformation and stress distribution within the structure domain, the following governing equations for linear elastic material are shown:

For the equation of motion, Newton's second law applies:

$$\nabla \cdot \boldsymbol{\sigma} + \boldsymbol{F} = \rho\ddot{\boldsymbol{\varphi}} \qquad\qquad Eq\ 2-12$$

Where $\boldsymbol{\sigma}$ represents Cauchy stress tensor, $\boldsymbol{F}$ represents the body force per unit volume, ρ represents the material density, and $\boldsymbol{\varphi}$ represents the displacement of the material

$$where\ \ddot{\boldsymbol{\varphi}} = \frac{\partial^2\boldsymbol{\varphi}}{\partial t^2}$$

For the equation of strain-displacement relationship:

$$\varepsilon = \frac{1}{2}(\nabla\boldsymbol{\varphi} + \nabla\boldsymbol{\varphi}^T)\ or\ \varepsilon_{mn} = \frac{1}{2}\left(\frac{\partial\boldsymbol{\varphi}_m}{\partial x_n} + \frac{\partial\boldsymbol{\varphi}_n}{\partial x_m}\right) \qquad Eq\ 2-13$$

Converted in matrix form:

$$\varepsilon = \begin{bmatrix} \varepsilon_x & \varepsilon_{xy} & \varepsilon_{xz} \\ \varepsilon_{xy} & \varepsilon_y & \varepsilon_{yz} \\ \varepsilon_{xz} & \varepsilon_{yz} & \varepsilon_z \end{bmatrix}$$

Appling the general equation of Hook's Law in order to relate stress and strain:

$$\boldsymbol{\sigma} = \boldsymbol{C} : \boldsymbol{\varepsilon} \qquad\qquad Eq\ 2-14$$

Converted in matrix form:

$$
\begin{bmatrix} \sigma_{11} \\ \sigma_{22} \\ \sigma_{33} \\ \sigma_{23} \\ \sigma_{31} \\ \sigma_{12} \end{bmatrix} = \begin{bmatrix} C_{1111} & C_{1122} & C_{1133} & C_{1112} & C_{1123} & C_{1113} \\ C_{1122} & C_{2222} & C_{2233} & C_{2212} & C_{2223} & C_{2213} \\ C_{1133} & C_{2233} & C_{3333} & C_{3312} & C_{3323} & C_{3313} \\ C_{1112} & C_{2212} & C_{3312} & C_{1212} & C_{1223} & C_{1213} \\ C_{1123} & C_{2223} & C_{3323} & C_{1223} & C_{2323} & C_{2313} \\ C_{1113} & C_{2213} & C_{3313} & C_{1213} & C_{2313} & C_{1313} \end{bmatrix} \begin{bmatrix} \varepsilon_{11} \\ \varepsilon_{22} \\ \varepsilon_{33} \\ 2\varepsilon_{23} \\ 2\varepsilon_{31} \\ 2\varepsilon_{12} \end{bmatrix}
$$

where C is the elasticity matrix. Appling the generalized Hook's Law for isotropic material yields:

$$
\begin{bmatrix} \sigma_{11} \\ \sigma_{22} \\ \sigma_{33} \\ \sigma_{23} \\ \sigma_{31} \\ \sigma_{12} \end{bmatrix} = \begin{bmatrix} C_{1111} & C_{1122} & C_{1133} & 0 & 0 & 0 \\ C_{1122} & C_{2222} & C_{2233} & 0 & 0 & 0 \\ C_{1133} & C_{2233} & C_{3333} & 0 & 0 & 0 \\ 0 & 0 & 0 & C_{1212} & 0 & 0 \\ 0 & 0 & 0 & 0 & C_{2323} & 0 \\ 0 & 0 & 0 & 0 & 0 & C_{1313} \end{bmatrix} \begin{bmatrix} \varepsilon_{11} \\ \varepsilon_{22} \\ \varepsilon_{33} \\ 2\varepsilon_{23} \\ 2\varepsilon_{31} \\ 2\varepsilon_{12} \end{bmatrix}
$$

Finally, equate the strain of structure domain based on stress with the replacement of elasticity matrix using Young's modulus and Poisson's ratio:

$$
\begin{bmatrix} \varepsilon_{11} \\ \varepsilon_{22} \\ \varepsilon_{33} \\ 2\varepsilon_{23} \\ 2\varepsilon_{31} \\ 2\varepsilon_{12} \end{bmatrix} = \frac{E}{(1-v)(1-2v)} \begin{bmatrix} 1-v & v & v & 0 & 0 & 0 \\ v & 1-v & v & 0 & 0 & 0 \\ v & v & 1-v & 0 & 0 & 0 \\ 0 & 0 & 0 & \dfrac{1-2v}{2} & 0 & 0 \\ 0 & 0 & 0 & 0 & \dfrac{1-2v}{2} & 0 \\ 0 & 0 & 0 & 0 & 0 & \dfrac{1-2v}{2} \end{bmatrix} \begin{bmatrix} \sigma_{11} \\ \sigma_{22} \\ \sigma_{33} \\ \sigma_{23} \\ \sigma_{31} \\ \sigma_{12} \end{bmatrix}
$$

Where E represents the Young's modulus of the material and v represents the Poisson's ratio for the material. The final above result calculates the engineering strain of the structure domain with given stress of the domain. With finite element analysis, the deformation of the blood vessel and artificial valve can be obtained by computing the boundary stress from the fluid-structure interface, which is described in the following section.

2.2.3 Fluid-Structure Coupling Equations

With the governing equations for both fluid and structure domain established, the last set of equations for computing a FSI problems is to establish governing equations for the fluid-structure interface. Given that heart valves are passive and driven by the blood pressure difference across the valve, the initial calculation is to compute the velocity between fluid and structure interface as shown in Eq $2-15$. With the velocity of fluid and structure boundary known, Navier Stokes equation can be applied in order to calculate the pressure generated by fluid, shown on the left hand side of Eq $2-16$, balanced by the stress of within structure domain, given from the right hand side of Eq $2-16$.

$$u_{fluid} = \frac{\partial \varphi_{structure}}{\partial t} \qquad\qquad Eq\ 2-15$$

$$\left[-p\boldsymbol{I} + \mu\left(\nabla\boldsymbol{u}_{fluid} + \left(\nabla\boldsymbol{u}_{fluid}\right)^{T}\right)\right]\cdot\boldsymbol{n} = \boldsymbol{\sigma}\cdot\boldsymbol{n} \qquad\qquad Eq\ 2-16$$

Where u_{fluid} represents the velocity of the fluid domain and σ represents Cauchy stress tensor With the stress of the structure domain calculated based on fluid pressure and the structure motion based on fluid velocity, the force within structure domain can be calculated as shown in Eq $2-17$. Since domains are being deformed, Eq $2-18$ to Eq $2-20$ recalculate stress and displacement from pre-deformed state to post-deformed state in order to determine structural stress and deformation.

$$\rho\frac{\partial^{2}\boldsymbol{\varphi}_{structure}}{\partial t^{2}} - \nabla\cdot\boldsymbol{\sigma} = \boldsymbol{F}_{v} \qquad\qquad Eq\ 2-17$$

$$S_{ij} - S_{ij}{}^{o} = C(\epsilon) \qquad\qquad Eq\ 2-18$$

$$\boldsymbol{\sigma} = det(\boldsymbol{F})^{-1}\boldsymbol{F}\boldsymbol{S}\boldsymbol{F}^{T} \qquad\qquad Eq\ 2-19$$

$$\rho\frac{\partial^{2}\boldsymbol{\varphi}_{structure}}{\partial t^{2}} = \boldsymbol{f}_{v} - \nabla\sigma \qquad\qquad Eq\ 2-20$$

Where $\boldsymbol{F}_v$ represents the volume force vector prior to deformation, S represents the second Piola-Kirchhoff stress tensor, and $\boldsymbol{f}_v$ represents the force in present state with respect to the deformed volume.

2.3   Boundary Condition Declaration

To fully describe the problem given the computational domain, boundary conditions must be fully defined for all boundaries. Given that the flow around aortic valve is unidirectional, the flow inlet and outlet must be defined accordingly. Moreover, the outer boundaries of wall and fluid-structure interface should also be defined based on given geometry. Nevertheless, the physical constraints for the geometry are defined based on different types of artificial heart valve.

2.3.1   Inlet and Outlet Boundary

Given the computational domains from section 2.1, the flow direction of the blood is defined from left to right along x-axis based on the configuration of artificial heart valve orientation, such as shown in Figure 2.2.

Since blood flow within body is a pressure driven flow, the inlet boundary on the left hand side is declared with an inlet pressure boundary condition, shown in Eq $2 - 21$, while the outlet boundary on the right hand side is declared with an outlet pressure boundary condition, shown in Eq $2 - 22$, with given governing equation show below:

$$p = p_{ventricular} \qquad\qquad Eq\ 2 - 21$$

$$p = p_{aortic} \qquad\qquad Eq\ 2 - 22$$

$$\left[\mu \left(\nabla \boldsymbol{u}_{fluid} + \left(\nabla \boldsymbol{u}_{fluid} \right)^T \right) \right] \cdot \boldsymbol{n} = 0 \qquad\qquad Eq\ 2 - 23$$

The pressure of the inlet and outlet boundaries are given with physiological pulsatile pressure profile interpolated from Choi[43]. Two different methods were used for

interpolating the pressure values for the boundaries: Fourier series and cubic spline. The Fourier series for reconstructing the aortic pressure and ventricular pressure are shown in Eq 2 − 24 and Eq 2 − 25 with eleven coefficients for higher accuracy. The complete pressure profile is shown in Figure 2.6.

$$
\begin{aligned}
p_{aortic} = 96.71 &- 18.66\cos(\omega t) + 2.588\sin(\omega t) + 0.1822\cos(2\omega t) \\
&- 8.668\sin(2\omega t) + 4.406\cos(3\omega t) + 0.4626\sin(3\omega t) \\
&+ 0.05867\cos(4\omega t) + 1.393\sin(4\omega t) - 2.101\cos(5\omega t) \\
&+ 1.187\sin(5\omega t) \\
&\quad where\ \omega = 8.438
\end{aligned}
$$

Eq 2 − 24

$$
\begin{aligned}
p_{venttricular} = 44.24 &- 50.76\cos(\omega t) + 44.4\sin(\omega t) \\
&- 0.4108\cos(2\omega t) - 19.45\sin(2\omega t) - 0.3481\cos(3\omega t) \\
&- 6.66\sin(3\omega t) + 8.032\cos(4\omega t) + 2.597\sin(4\omega t) \\
&+ 0.3551\cos(5\omega t) + 2.903\sin(5\omega t) \\
&\quad where\ \omega = 8.72
\end{aligned}
$$

Eq 2 − 25
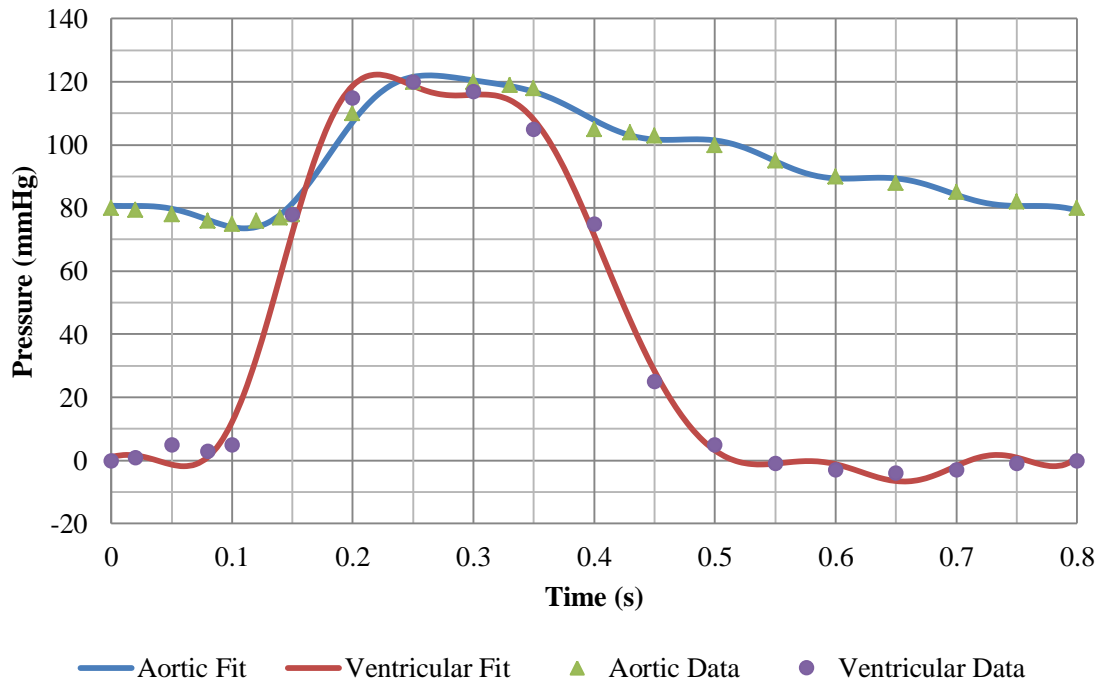
Figure 2.6 Fourier Series Interpolation of Aortic and Ventricular Pressure Profile

The advantage of applying Fourier series is that the function is well defined and continuous; therefore, the function would have a defined derivative at any point in time, which increases stability for the solver. However, since Fourier series interpolates the pressure profile based on given data series with the combination of sine and cosine function, the accuracy of profile magnitude and phase of the interpolated profile relative to the exact data series is decreased. Therefore, the final pressure profile from Fourier series would suffer from minor lag for pressure profile magnitude and time relative to the exact physiological pulsatile pressure profile with additional oscillation in pressure magnitude. In order to resolve the time lag due to the reconstruction of pressure profile using Fourier series, another method that applies cubic spline for pressure profile interpolation is deployed such that the reconstructed cubic spline function would smoothly pass through the data series obtained from exact physiological pulsatile pressure profile, shown in Figure 2.7. To reconstruct the inlet and outlet pressure profile from cubic spline, the generalized equation, shown in Eq $2 - 26$, is applied to any two adjacent data points from the exact physiological pulsatile pressure profile.

$$
\begin{aligned}
f(x) = {} & \left(1 - \frac{x - x_1}{x_2 - x_1}\right) y_1 + \left(\frac{x - x_1}{x_2 - x_1}\right) y_2 \\
& + \left(\frac{x - x_1}{x_2 - x_1}\right)\left(1 - \frac{x - x_1}{x_2 - x_1}\right)\left(C_1\left(1 - \frac{x - x_1}{x_2 - x_1}\right)\right. \\
& \left. + C_2\left(\frac{x - x_1}{x_2 - x_1}\right)\right) \\
& where\ C_1 = f'(x_1)(x_2 - x_1) - (y_2 - y_1) \\
& \qquad\quad C_2 = -f'(x_1)(x_2 - x_1) + (y_2 - y_1)
\end{aligned}
$$

$$Eq\ 2 - 26$$
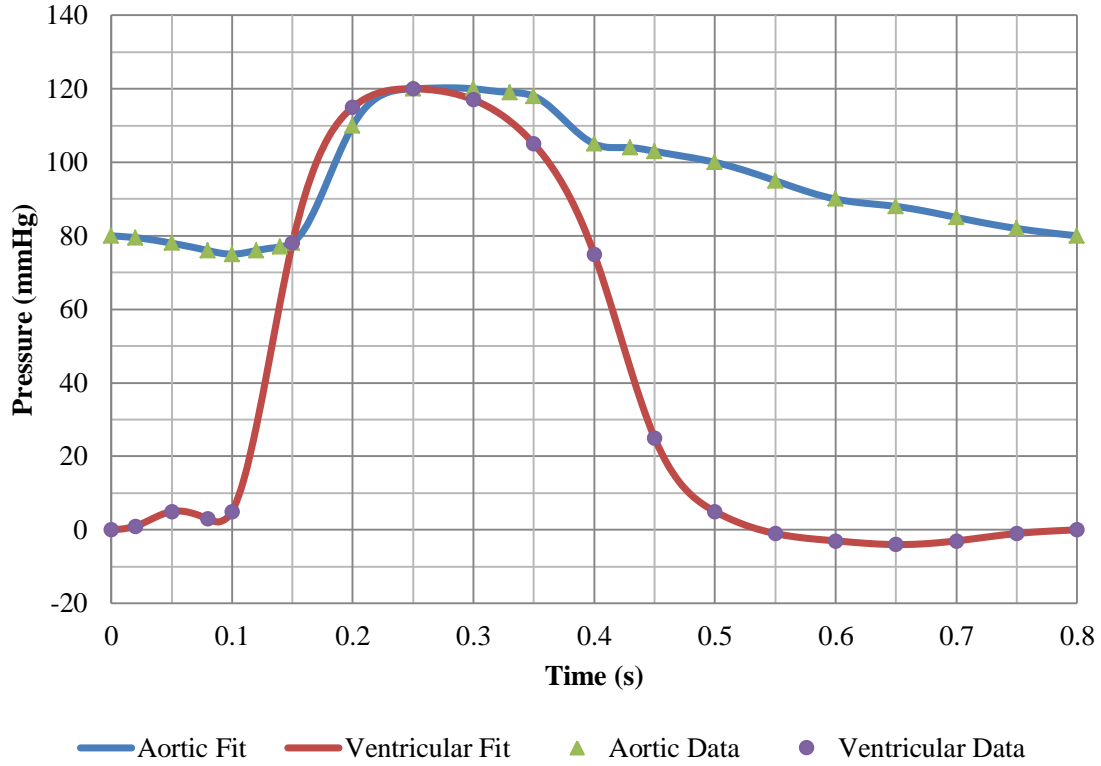
Figure 2.7 Cubic Spline Interpolation of Aortic and Ventricular Pressure Profile

2.3.2 Fluid-Structure Interface

The fluid-structure interface is defined along any interface between the fluid domain and structure domain. There are four main cases with different geometrical configuration investigated: rigid wall mechanical valve, flexible wall mechanical valve, rigid wall bioprosthetic valve, and flexible wall bioprosthetic valve. The fluid-structure interface for the rigid wall models for both mechanical valve and bioprosthetic valve have the interface deployed along the surface of the valve next to fluid domain. On the other hand, the fluid-structure interface for the flexible wall models have the interface deployed not only along the surface of the valve but also the surface of the blood vessel next to fluid domain.

2.3.3 Physical Constraints

The last piece of information required to fully define the whole computational domain is to define physical constraints for any undefined boundary. For the case of mechanical valve, it is necessary to define the boundaries to constrain valve leaflet motion correctly; therefore, the hinge of mechanical valve is defined with a free rotation boundary condition. However, since artificial mechanical valve is designed with a minimum closure angle of 25 degree and a maximum opening angle of 85 degree, the free rotation boundary condition would be insufficient to constrain the leaflet motion correctly. In order to address the minimum and maximum constrain issues, additional constraints are introduced to each leaflet joints for each opening or closing conditions. A total of four constraints are defined for the two mechanical valve leaflet joints in order to avoid the assumption of symmetrical geometry such that each joint has two independent constraints, one that controls leaflet closure and one controls leaflet opening. Since the constraints are introduce numerically, the geometrical complexity of mechanical valve leaflet joints can be simplified as mentioned in section 2.1.2. To evaluate the constraints in order to properly control leaflet motion, Eq 2 − 27 and Eq 2 − 28 are used such that a counter moment can be added to counter act the leaflet motion once the minimum or maximum leaflet angle is reached.

$$if(\alpha < 25)(K_1)(25 - \alpha)(M_{add}) = 0 \qquad\qquad Eq\ 2-27$$
$$if(\beta > 85)(K_2)(\beta - 85)(M_{add}) = 0 \qquad\qquad Eq\ 2-28$$

Where α and β represent the current angular position of the valve leaflets, K_1 and K_2 represent the control constants for adjusting magnitude of applied moment, and M_{add} represents the amount of moment added to the valve leaflet when the constrain is activated.

With the Boolean operation that controls Eq 2 – 27 and Eq 2 – 28 to be zero when the mechanical leaflets are within the free rotation range, the physical constraints for the leaflet joints are satisfied. One drawback of the Boolean operation is that it may generate convergence issues for the solver; therefore, the Boolean operation is further replaced by a step function in order to enhance solver stability.

Additional constrain that prescribe zero displacement is applied to any boundary that does not displace during the duration of cardiac cycle. The locations for this type of constrain can be found near the base of bioprosthetic valve and near end of blood vessel wall. Moreover, for the case of rigid wall models, wall boundary is applied along the inner surface of blood vessel to ensure no further deformation. Nevertheless, the constrain of free deformation is applied to the outer surface of blood vessel to ensure proper flexibility of blood vessel.

2.4   Computational Procedure Generalization

With both geometries and boundary conditions fully defined, the computational procedure can be generalized before the final calculation. To generalize the solver configurations, the mesh elements of the computational domain are necessary to be established first. Once the mesh elements are configured, the arbitrary Lagrangian-Eulerian formulation (ALE) can be applied with mesh quality limit in order to ensure solution accuracy. Finally, the selection of solver for solving the computational domain is described. The proposed model is constructed to be ALE, monolithic, strongly coupled, two-way FSI simulation.

2.4.1 Mesh Configuration

The basic mesh elements are constructed with unstructured triangular mesh for both fluid and structure domain. An additional meshing step is introduced with rectangular elements defining boundary layers in order to ensure accurate solution within boundary layers. To fully configure and distribute the mesh elements across computational domain, the mesh for structure domain and fluid domain are defined separately. For mesh element within fluid domain, density of the mesh is determined based the predefined constants given by COMSOL, which adjusts the element size for the domain. Depending on different simulated scenarios and mesh configurations, the maximum element size is configured below $3\ mm$ with minimum element size configured below $0.1\ mm$. The configured meshes result with a mesh count that range from approximately 15,000 to 100,000. Additional mesh refinements are introduced to the fluid-structure interface in order to enhance solution accuracy. Moreover, boundary layer has also been applied along fluid-structure interface for accurate streamline evaluation. Figure 2.8 shows the schematic diagram for the overall mesh construction sequence.
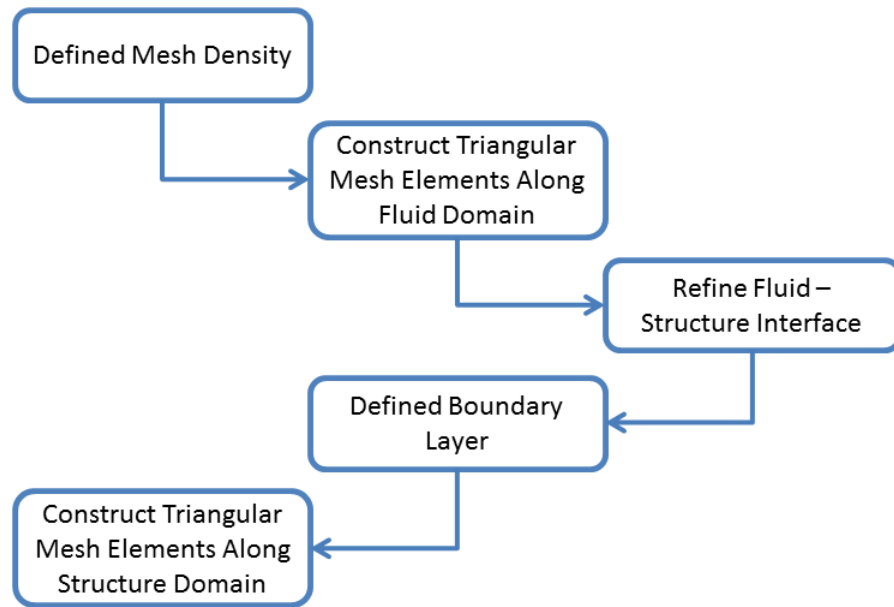
**Figure 2.8 Schematic Diagram for Mesh Construction**

2.4.2 ALE Configuration

Since a FSI problem contains both fluid and structure domain, any deformation generated by one domain would affect the other simultaneously; however, the deformation of structure is generally being described with Lagrangian frame of reference, where the frame of reference is fixed to the material, while the deformation of fluid is generally being described with Eulerian frame of reference, where the frame of reference is fixed in space. Combining the two domains for a FSI problem would require a unified method to describe the frame of reference; therefore, the arbitrary Lagrangian-Eulerian formulation, or the free mesh formulation, is applied in order to account for large mesh deformation and motion. It is required to applied ALE method for a FSI problem when the problem is described with a free mesh deformation algorithm due to the limitations from the use of either pure Lagrangian or Eulerian algorithm. If problem is to be solved with pure Lagrangian algorithm, the surface and the boundary of the problem might be able to be deformed given the deformation of the interface would be relatively small. On the other hand, if the problem is to be solved with pure Eulerian algorithm, the mesh configuration for the computational domain would require a higher resolution in order to account of mesh refinements. Given the limitations for either Lagrangian or Eulerian method, the ALE method relates the time derivative between material and referential, which further relates to material and spatial domain, such that mass, momentum, and energy would be conserved. Due to the complexity of ALE formulation, the discussions on the numerical aspects of ALE governing equations are out of scope of this study.

2.4.3 Solver Configuration

As discussed previously regarding to the advantages of applying different solver configuration for FSI problem in the literature review section from Introduction, the widely used partitioned approach provides flexibility of using segregated solver for either strongly coupled or weakly coupled solution with the cost of solver stability. On the other hand, the monolithic approach, which solves the system of equation within one step, provides a fully coupled solution with the additional cost of computational resource. Since a highly non-linear FSI problem would generate solver instability, the decision of

selecting the monolithic approach may be in favor. Given the highly non-linear properties of the problem, the time step for the solver is automatically determined by COMSOL with self-adjusting time stepping, which decrease the time step as necessary in order to obtain a converged solution for one time step. With the convergence criteria for a stable time step are set to be within one percent, a properly configured solver could calculate an accurate solution throughout the whole cardiac cycle with additional cost of computational time. Moreover, with the ALE method applied to FSI model, the mesh for the whole computational domain would be moved as the FSI interface deformed with respect to boundary load. The distorted meshes due to moving interface during the cardiac cycle would potentially create inverted mesh elements that further decrease solution accuracy and increase instability of the solver; therefore, the quality of the mesh would need to be checked and re-meshed whenever the mesh quality dropped below the mesh quality criteria. As the solution is calculated with monolithic direct solver, the overall solution procedure is presented in Figure 2.9 with schematic flow chart.
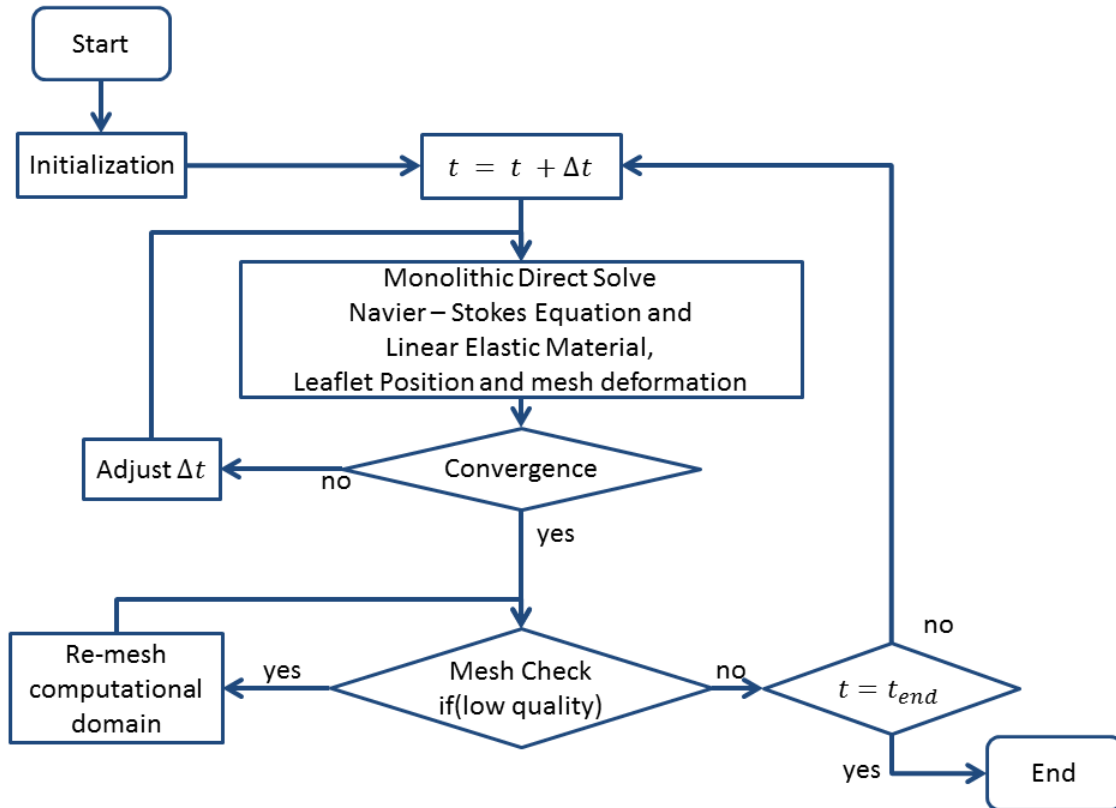
Figure 2.9 Overall Schematic Flow Chart of Solution Procedure

2.5   Experimental Setup

To verify and validate the computational model, the ViVitro Pulse Duplicator is used in order to apply physiological pulse under controlled environment, which fulfill the ISO 5840 and FDA guidance. Shown in Figure 2.10, the cardiac output is applied with realistic ventricle mounted to the piston-in-cylinder pump, which controls the designated flow rate. Different physiological waveforms can be generated by software and data acquisition system. Both aortic and mitral valve chamber is angular tilted and mounted to the ventricular chamber with clearance for flow visualization and PIV data collection.

Figure 2.10 ViVitro Pulse Duplicator for Artificial Valve Evaluation[49]

In Figure 2.11, a cross sectional schematic diagram of the ViVitro flow loop is presented. With a realistic, flexible left ventricle pressurized by some surrounding working fluid, blood flow is ejected from mitral valve to aortic valve in order to measure the hemodynamic performance of testing valves. The surrounding working fluid is precisely controlled by ViVitro Pulse Duplicator to ensure accurate cardiac output. A realistic aortic root is included in the test chamber made of rigid transparent acrylic block for the PIV visualization.
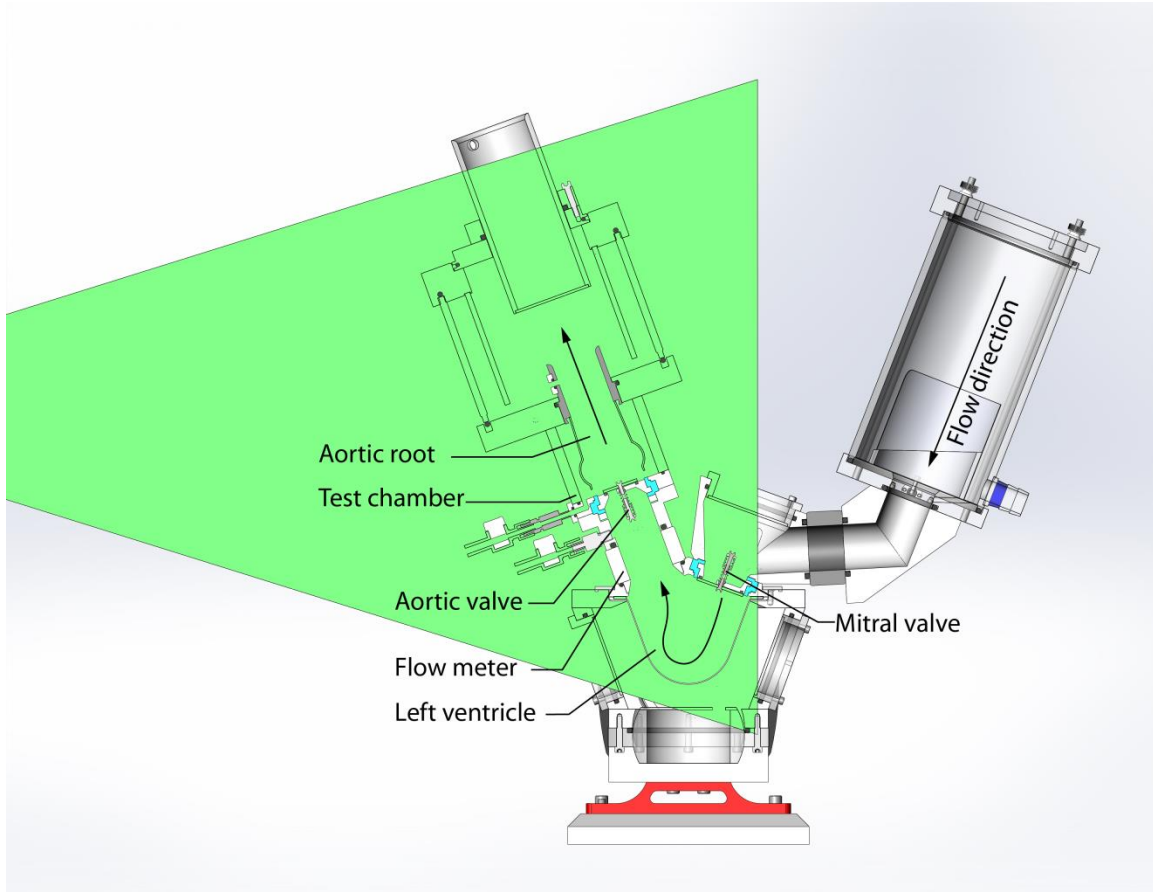
Figure 2.11 Schematic Diagram of ViVitro Flow Loop

2.6   Chapter Summary

In summary, the four two-dimensional computational domains for simulating artificial heart valve were established. The bileaflet mechanical valve models and the bioprosthetic tissue valve models were constructed with a rigid blood vessel assumption and a flexible blood vessel assumption applied to each type of valve model separately. The governing equations for fluid domain and structure domain were defined with the coupling equations for fluid-structure interface. Additionally, the configurations of the mesh elements and the solver were discussed.

Chapter 3

Results and Discussions for Bileaflet Mechanical Valve

With the computational models and simulation procedure fully established, each of the two main simulations on bileaflet mechanical valve and bioprosthetic tissue valve can be conducted. To summarize briefly regarding to the overall results from FSI simulations, the post processed results for bileaflet mechanical valve are firstly presented in this chapter. The results for bioprosthetic tissue valve would be presented in the following chapter. In order to verify and validate the numerical experiments conducted using the computational scheme discussed in Chapter Two, both literature review and PIV experimental data comparison against different computational models are conducted. Moreover, the primary results for bileaflet mechanical valve focus on the hemodynamics and shear stress around aortic valve and aortic root geometry, specifically the flow velocity distribution for valve performance and maximum shear stress for blood damage. The secondary results focus on the overall leaflet dynamics regarding the leaflet position in one complete cardiac cycle for bileaflet mechanical valve and the maximum von Mises stress distributed within the valve leaflet. Furthermore, clinical applications and evaluations regarding to mechanical valve leaflet malfunction are going to be discussed.

3.1 Rigid Wall Bileaflet Mechanical Valve

The primary objective of the study is to construct CFD models with the use of FSI method in order to evaluate both the hemodynamics and the structural dynamics of the artificial heart valves. The presented results in this section are going to focus on the simulated result for bileaflet mechanical valve with rigid wall assumption. In order to discuss the results processed from the simulated models, verification of the models is firstly discussed, followed by the hemodynamics of the blood flow around mechanical valve, and the structure dynamics of mechanical valve leaflet.

3.1.1 Verification and Validation

With the results for rigid wall mechanical valve presented and discussed above, the verification and validation can be discussed by comparing the average velocity at the outlet and average downstream velocity. In order to confirm the accuracy and correctness of the constructed models, a study on mesh convergence is firstly conducted. Given that the model is solved using finite element method, a proper mesh size should be established in order to ensure solution is mesh configuration independent for accurate results. Briefly discussed in the method section, since the computational domain is in 2D and mesh is generated using triangular elements for general domain and rectangular elements for boundary layer, the configuration of different mesh is by adjusting the element growth rate and element size.

Table 3.1 Summary of Mesh Configuration for Rigid Wall Mechanical Valve

Mesh Config.	Coarse	Fine	Finer	Extra	Extreme
Mesh Count	6765	13294	18505	34986	47372
Min Quality	0.33	0.39	0.34	0.39	0.39
Max Quality	0.70	0.68	0.69	0.72	0.72
% Difference	0%	97%	174%	417%	600%

Showing in Table 3.1, five different mesh configurations are summarized using the coarse mesh configuration as baseline for comparing across different mesh configurations.

With the total mesh element difference compared between any configurations against coarse mesh, the growth of total element can be shown in percentage: the fine mesh of 97%, the finer mesh of 174%, the extra fine mesh of 417%, and the extremely fine mesh of 600%. Notice that the minimum and maximum mesh qualities remain relatively similar such that any fluctuation due to mesh quality between different mesh configurations could be minimalized. In order to study the effect on solution accuracy of different mesh configurations, the average existing velocity in x-direction is calculated for each configuration, shown in Figure 3.1.

The average U velocity profile for different configurations at outlet are plotted in time with the profiles clearly showing that solution would be independent after the extra fine mesh configuration, while the coarse, fine, and finer mesh configurations would have a varying average outlet velocity due to the increase of mesh elements. Given that the difference between extra fine mesh and extremely fine mesh in average velocity is well below 5% during the peak-opening phase and 10% during the end-opening phase, due to the delay on valve closure, it is decided that the selected mesh configuration would be configured with the extra fine mesh due to mesh independence and computational consumptions.
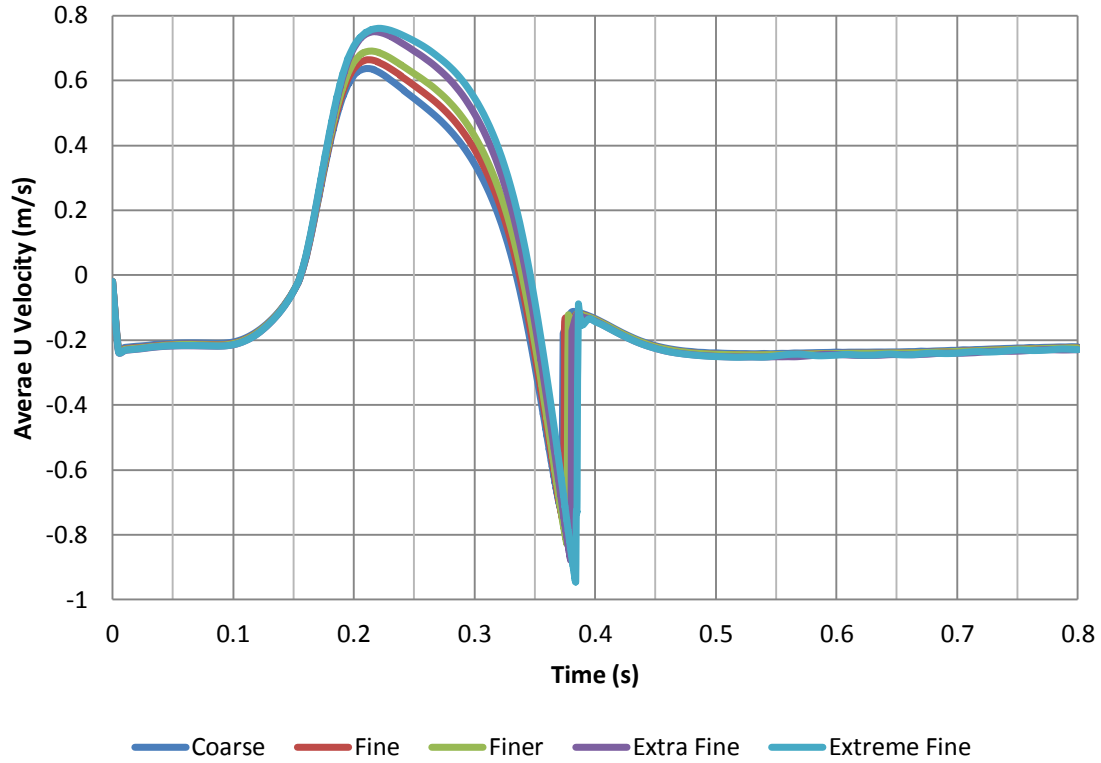
Figure 3.1 Average U Velocity at Outlet for Different Mesh Configurations

In addition to mesh convergence study for the computational model, the PIV experimental data collected by ViVitro Lab and the University of Victoria are used in order to compare the experimental hemodynamics evaluations on bileaflet mechanical heart valve against the proposed model in this study. Note that different boundary conditions are applied for PIV experiments with computer controlled volumetric flow rate and the peak systole occur at $0.15\ s$. Given that specific pressure boundary conditions and geometrical configurations are constructed for validation, the comparison is conducted for various time frames around peak systole away from bileaflet mechanical valve at approximately $9\ mm$ downstream. To validate the temporal velocity profile, experimental data are compared with simulated result, shown in Figure 3.2(a) to Figure 3.2(c). In addition, velocity profiles at different locations at peak systole are calculated to validate spatial velocity profile, shown in Figure 3.3(a) to Figure 3.3(c).
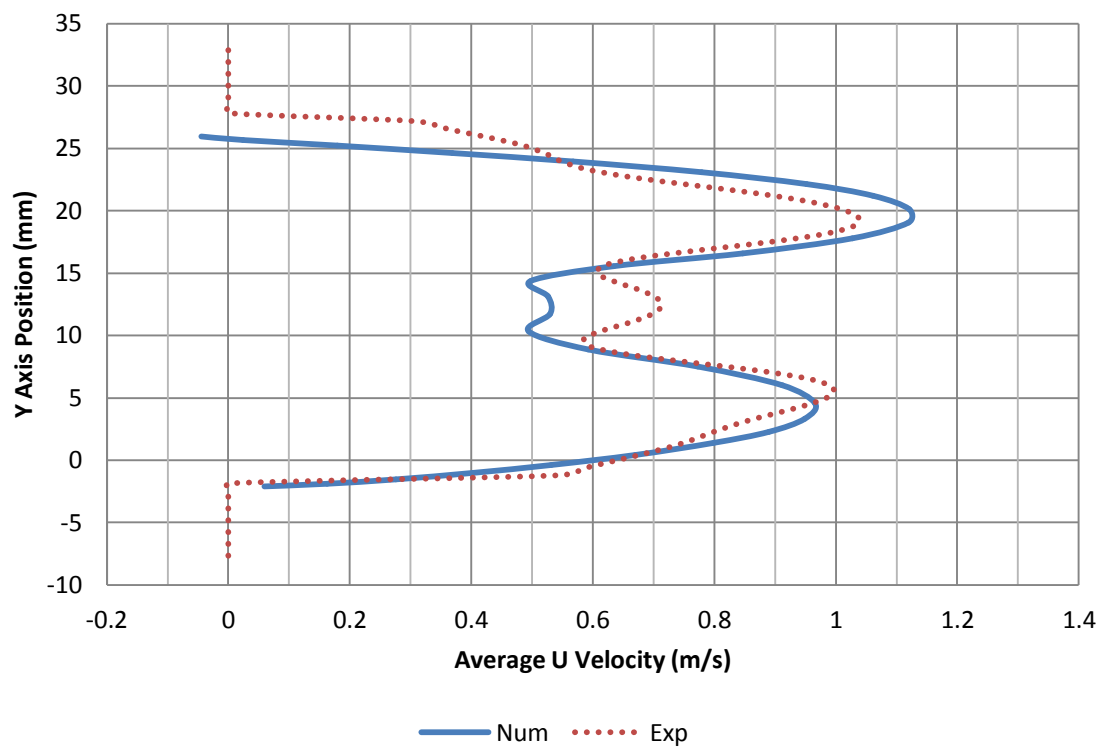
(a) 0.13 *s*
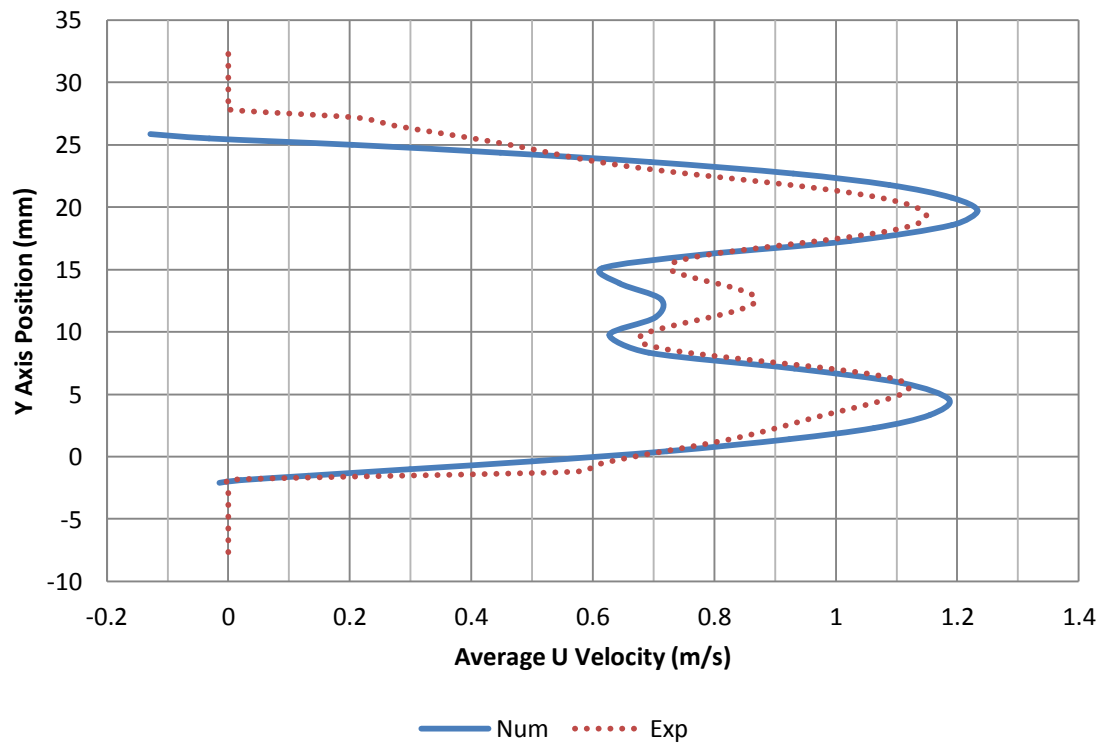
(b) 0.14 *s*
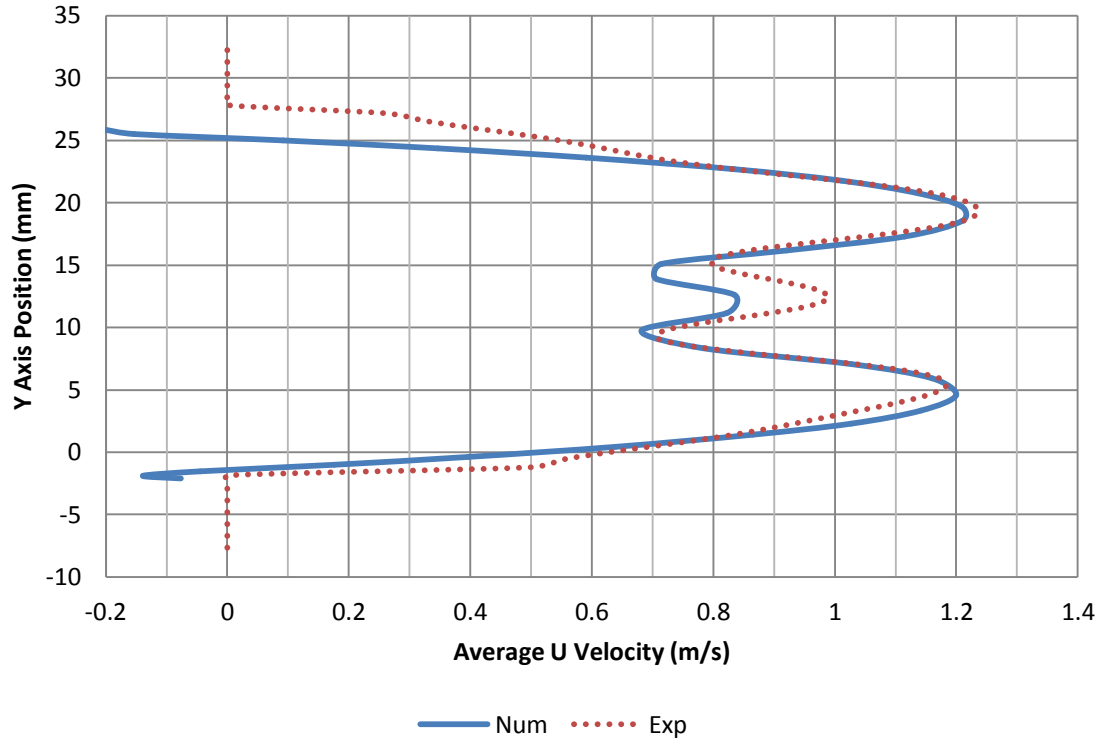
(c) $0.15\ s$

Figure 3.2 Numerical and Experimental Velocity Comparison at $30\ mm$ Downstream at Various Time Frame Near Peak Systolic

As shown in Figure 3.2, the result for average velocity around peak systole from numerical simulation has a slightly difference compare with the results obtained from experimental data. Noticeable throughout Figure 3.2(a) to (c), the central velocity jet has a relatively higher difference than the two side jets. One of the reasons causing this difference is due to the imposed initial conditions for numerical simulations; therefore, the difference decrease as the time advances from $0.13\ s$ to $0.15\ s$. During peak systole at $0.15\ s$, the maximum peak to peak velocity difference is roughly 15.6% around the central jet while the two side jets have a maximum velocity difference of 1.7%.

This difference may be caused by several experimental factors such as the frictional force within mechanical valve joints, the use of realistic ventricle for applying inlet flow, or the vertical tilting of the experimental apparatus for artificial valve. In addition to

experimental factors, the measurement conducted by PIV would also affect the result due to equipment resolution, laser reflection near the wall and the usage of glycerin-water mixture; therefore, the estimated uncertainty from PIV experiments is roughly 5% to 10%. Moreover, the experiment is controlling volumetric flow rate and targeted cardiac output such that the information on pressure gradient across the valve is measured, which is the primary boundary condition for computational model. Also, additional difference can be found at the center of the domain due to the result of no-slip boundary condition applied to the surface of valve leaflet.

In addition to temporal velocity difference, Figure 3.3(a) to Figure3.3(c) has showed that the velocity profiles are in good agreements for numerical simulation and PIV experiment. The velocity profiles at various downstream locations within computational domain are plotted in Figure 3.3 during peak systole at 0.15 s. The maximum velocity difference is located within the central velocity jet with a value of 10.5%, shown in Figure 3.3(c). Regarding to the maximum velocity difference at other locations, maximum of 15.6% difference is found in Figure 3.3(a) while maximum difference of 12.6% is found in Figure 3.3(b).

Despite of all factors influencing the final experimental data accuracy and resolution, the numerical simulations have been validated against experimental data with a slightly over estimated velocity profile around aortic valve.
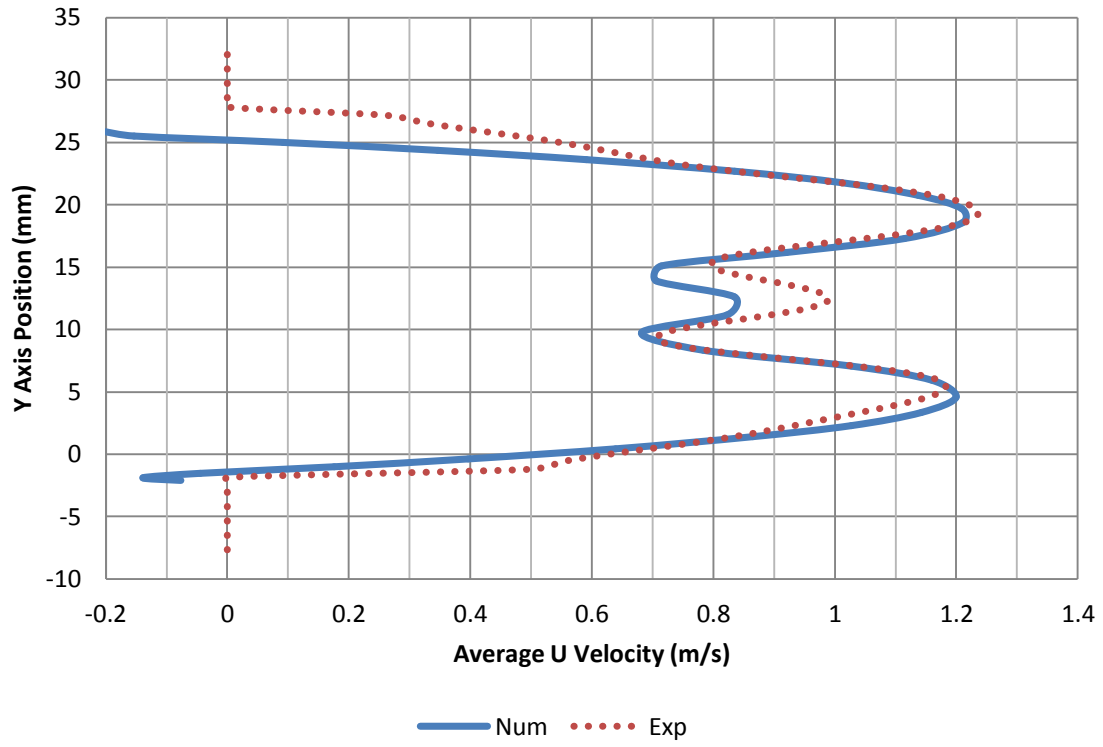
(a) 9 *mm* Downstream
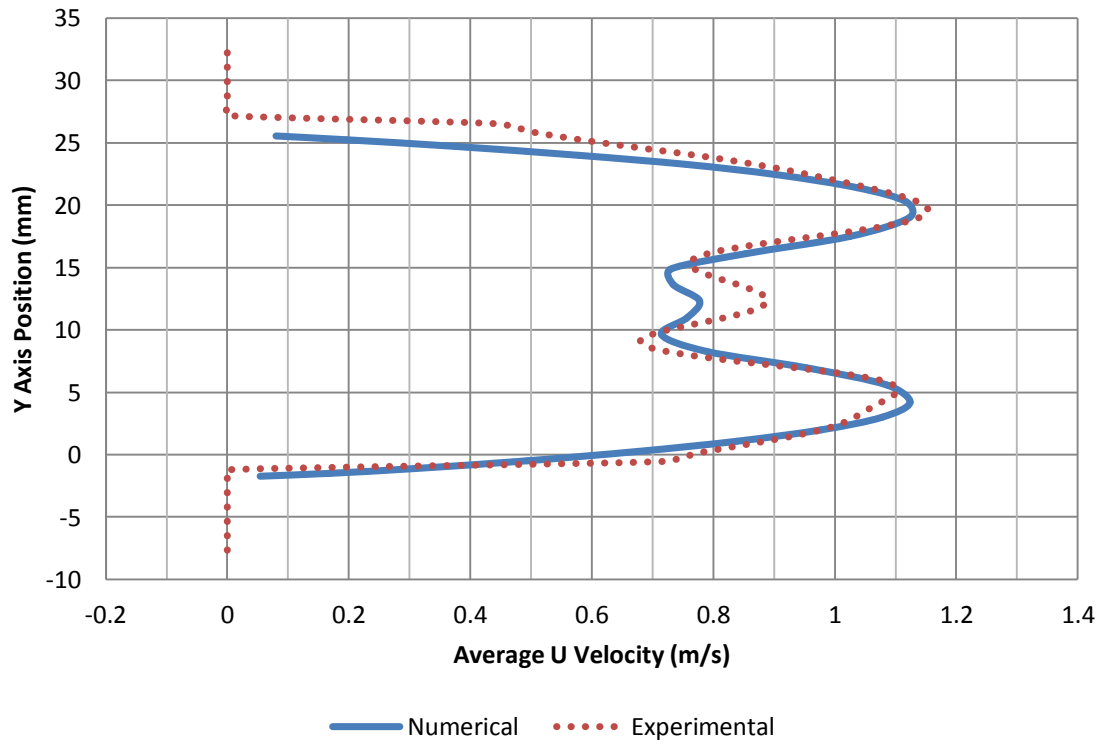
(b) 12 *mm* Downstream
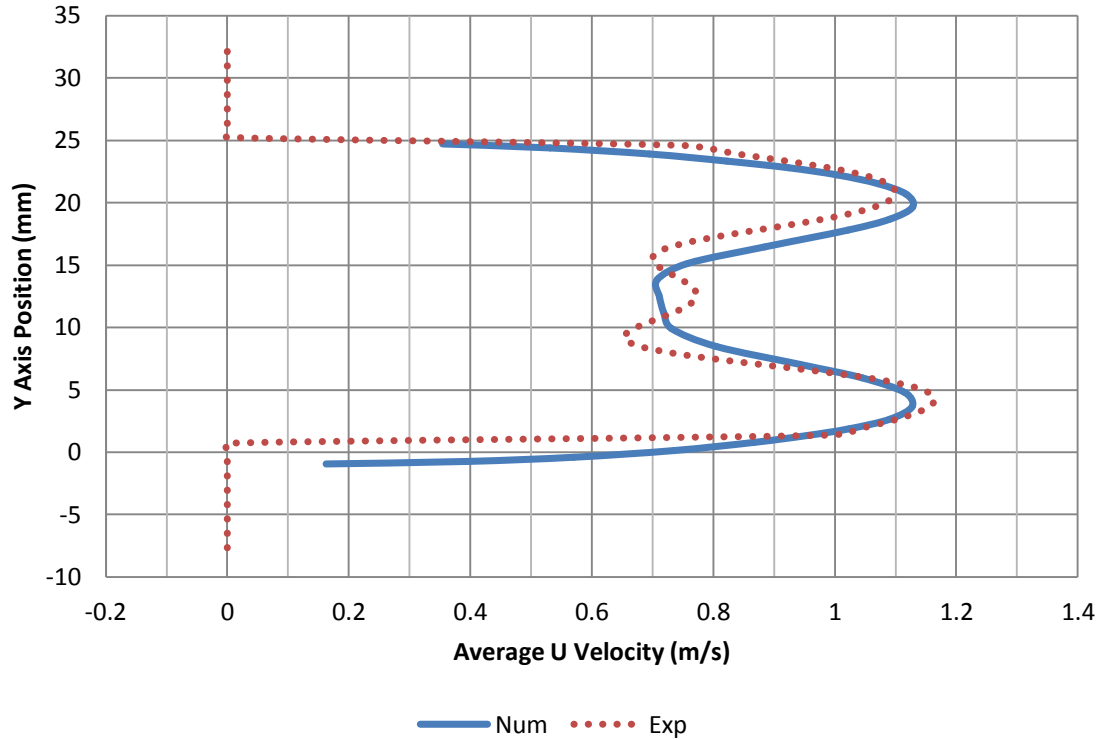
(c) $15\ mm$ Downstream

Figure 3.3 Numerical and Experimental Velocity Comparison at Various Downstream Locations during Peak Systolic

3.1.2 Blood Flow Hemodynamics

It is necessary to define several important phases during one cardiac cycle such that it would be relevant to compare across different models and different results. The identification of different cardiac phases is done relatively to the valve leaflet dynamics, which could easily be separated logically, in order to compare different simulated models. The defined cardiac phases for one cardiac cycle are differentiated as the initial-opening phase (the end-closing phase), the peak opening phase, the end-opening phase (the initial-closing phase), and the mid-closing phase. These different phases can be identified and related to the simulated time by referring to the boundary pressure profile shown in Figure 3.4: the initial-opening phase defined by the occurrence of equilibrium pressure across the valve at $0.15\ s$, the peak-opening phase defined by the occurrence of minimum pressure gradient after initial opening phase at $0.23\ s$, the end-opening phase defined by

the occurrence of mechanical valve leaflet closure at $0.38\ s$, and the mid-closing phase defined by the occurrence of steady back flow at $0.8\ s$. However, the identification of isolated time frame for different cardiac phases relative to the artificial valve are values that depended on artificial valve types, leaflet motion, and pressure profiles such that these values could only be the reference value for data comparison between different models.
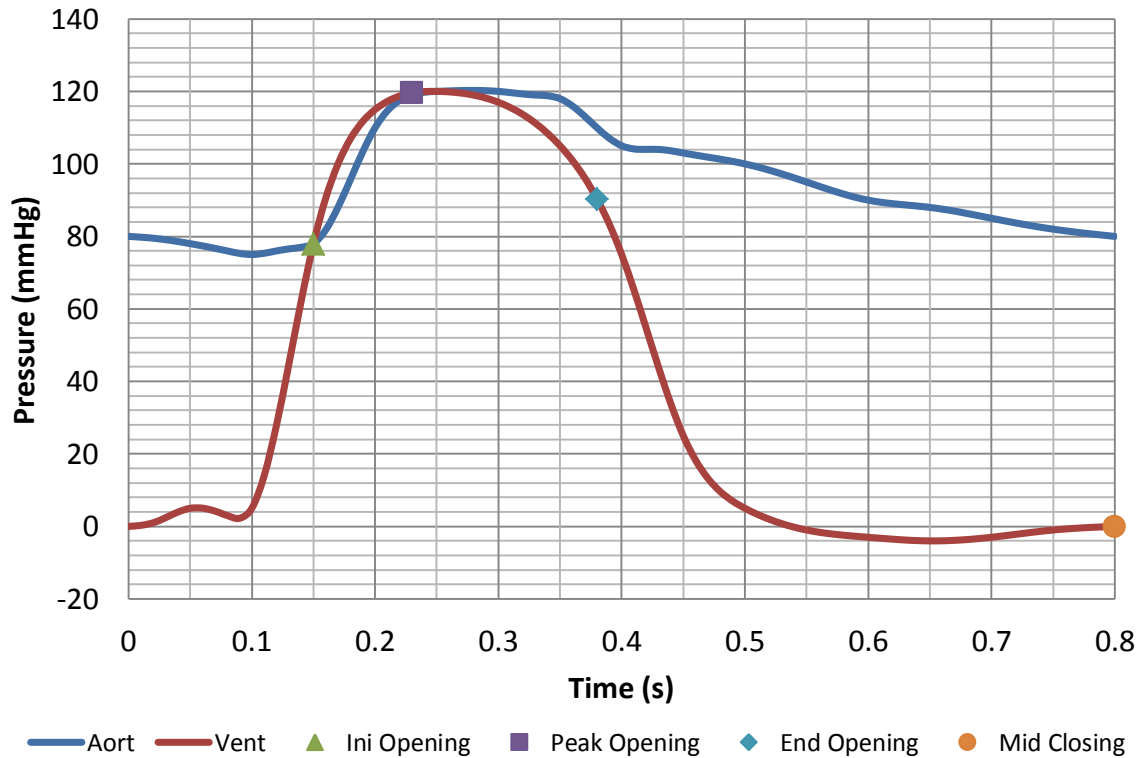
Figure 3.4 Isolated Times for Different Phases during Cardiac Cycle

Since the primary parameters that determine the performance of artificial heart valve are the pressure gradient across the valve and velocity distribution inside the domain, a series of isolated time steps for different phases of cardiac cycle is shown in Figure 3.5. The left column of Figure 3.5, (a) to (d), displays the velocity magnitude contour with the streamlines and velocity arrow vectors while the right column of Figure 3.5, (e) to (h), displays the shear stress contour, with a unit of dPa (dyn/cm^2), and reference velocity arrow vectors.

(a) 0.15 s

(e) 0.15 s

(b) 0.23 s

(f) 0.23 s

(c) 0.38 s

(g) 0.38 s

(d) 0.80 s

(h) 0.80 s
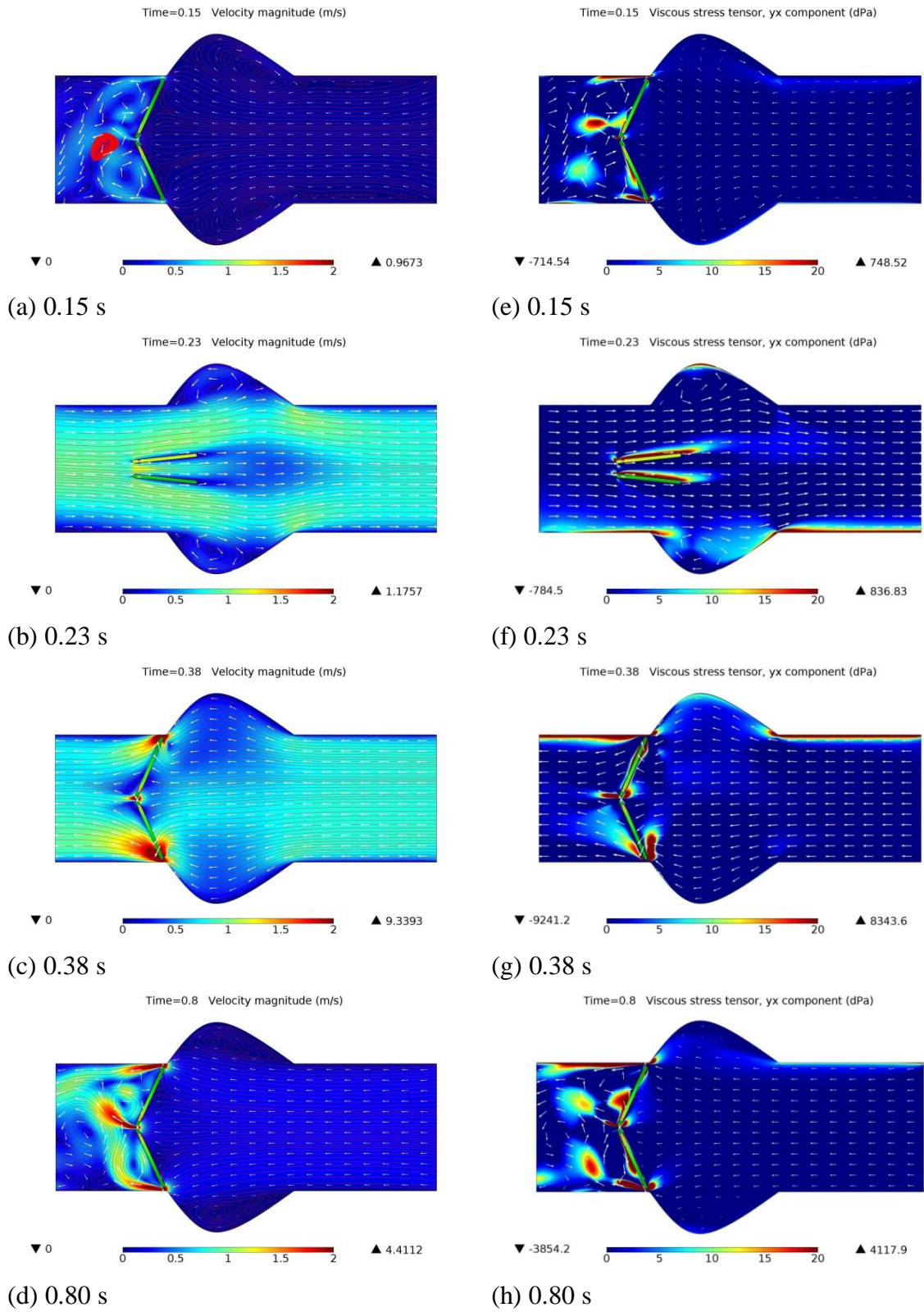
Figure 3.5 Isolated Time Frames during Different Cardiac Phases for Rigid Wall Mechanical Valve

To briefly discuss the results presented in Figure 3.5, the initial opening phase with the isolated time frame of $0.15\ s$ is firstly reviewed. Given that the pressure starts with a negative gradient at time zero, a steady leakage flow, due to the intervalvular space between valve leaflets at fully closed position, is successfully captured when reached to the initial-opening phase. At $0.15\ s$, where the pressure gradient is approximately zero, the backward flow velocity slowly reaches to zero and creates a central vortex behind the intervalvular space, shown by the concentrated streamline in Figure 3.5(a). Vortices are generated at the ventricular portion of the computational domain due to leakage jet. Since the flow around the initial-opening phase is at minimum, the area of high shear stress is concentrated near the boundary around the area where the leakage jets exist.

At the peak-opening phase, with time advanced to $0.23\ s$, where the pressure gradient reached to a minimum, the flow velocity reaches to a maximum with a velocity magnitude of $1.176\ m/s$. Given that the computational domain has a realistic aortic root geometry implemented, the result successfully reproduces the recirculation of blood flow within the aortic root, as it would be expected in native aortic valve to avoid particles deposition. As for the distribution of shear stress, a layer with higher shear stress is shown to be around the mechanical valve leaflet due to maximum forwarding blood flow. Furthermore, at the peak-opening phase, the valve leaflet reaches to a maximum opening position of 85 degree and maintains at maximum opening until the end of opening phase.

At the end-opening phase, with time advanced to $0.38\ s$, the mechanical valve leaflets are fully closed and generated a temporary peak backward flow from the mechanical valve leaflet closing. Due to the rapid change in flow direction, the distribution and the magnitude of shear stress around the artificial valve are expected to be increased to a much higher value than for previous time frames, as the shear stress contour plot identified. Interestingly, the velocity contour plot shows that high velocity magnitude only occurs near the intervalvular space at both end of mechanical valve leaflets while the high shear stress occur near the boundary of blood vessel wall due to the reverse flow.

Nevertheless, with time advanced to $0.8\ s$, the mid-closing phase of the cardiac cycle has revealed a near-zero velocity magnitude for the blood flow at the aortic side, especially within the realistic aortic root. Due to the narrow intervalvular space and a negative high pressure gradient across the valve, the leakage blood flow has a continuous high velocity magnitude, which greatly affects the distribution of shear stress. Moreover, the central leakage blood flow, located between the two leaflets at the center of the bileaflet mechanical valve, is found to have a transition oscillatory behavior under high velocity. Regarding the shear stress distribution during mid-closing phase, the shear stress contour has revealed a significant decrease in magnitude compare against the end-opening phase. In addition, the high shear stress distributed near the vessel wall on the aortic side during the end-opening phase has decreased to a near-zero magnitude, which suggests that the high wall shear stress would be temporary due to sudden valve closure. However, the shear stress near the end of mechanical valve leaflets remain as high as 4,000 dPa, which suggests a high possibility of thrombosis occurrence.

To analyse quantitatively the hemodynamics, the velocity across the diameter of the aortic root could be plotted in order to investigate the downstream velocity distribution. The selection of the exact position for the evaluation of cross sectional velocity is determined based on the maximum wall-to-wall distance within the aortic root, which could be approximated at $9\ mm$ downstream from the base of aortic root. Therefore, the overall cross sectional velocity could be calculated and the velocity within aortic root could also be fully captured. Shown in Figure 3.6, the velocity distribution at $9\ mm$ downstream is plotted with the vertical axis reflecting the y-position of the aortic root and the horizontal axis reflecting the x component of the velocity vector while the center line of the aorta is marked in order to clearly identify the center of flow. As one may expected, the velocity for the initial-opening phase at $0.15\ s$ has an approximated small reversed value of $-0.05\ m/s$ due to the leakage flow from the beginning of cardiac cycle. For the peak-opening phase at $0.23\ s$, an approximated peak velocity of $0.95\ m/s$ has found near the outer side of the two mechanical valve leaflets with a smaller velocity profile of $0.7\ m/s$ between the leaflets due to the intervalvular space of the mechanical valve.

Moreover, during the peak-opening phase, a reversed velocity of $-0.35\ m/s$ has been found to occur within the realistic aortic root, which confirmed the recirculation due to normal valve leaflet motion. For the end-opening phase at $0.38\ s$, a peak reverse velocity with an approximated value of $-0.73\ m/s$ near the center of the flow is found. Since the flow characteristic at the end-opening phase would be a total reverse flow, the velocity profile shown in the figure has confirmed that all velocities across the cross sectional plane are negative. Nevertheless, for the mid-closing phase, the reversed velocity is decrease and stabilized to an approximated value of $-0.2\ m/s$ with a small recirculation velocity of $0.06\ m/s$ within aortic root.
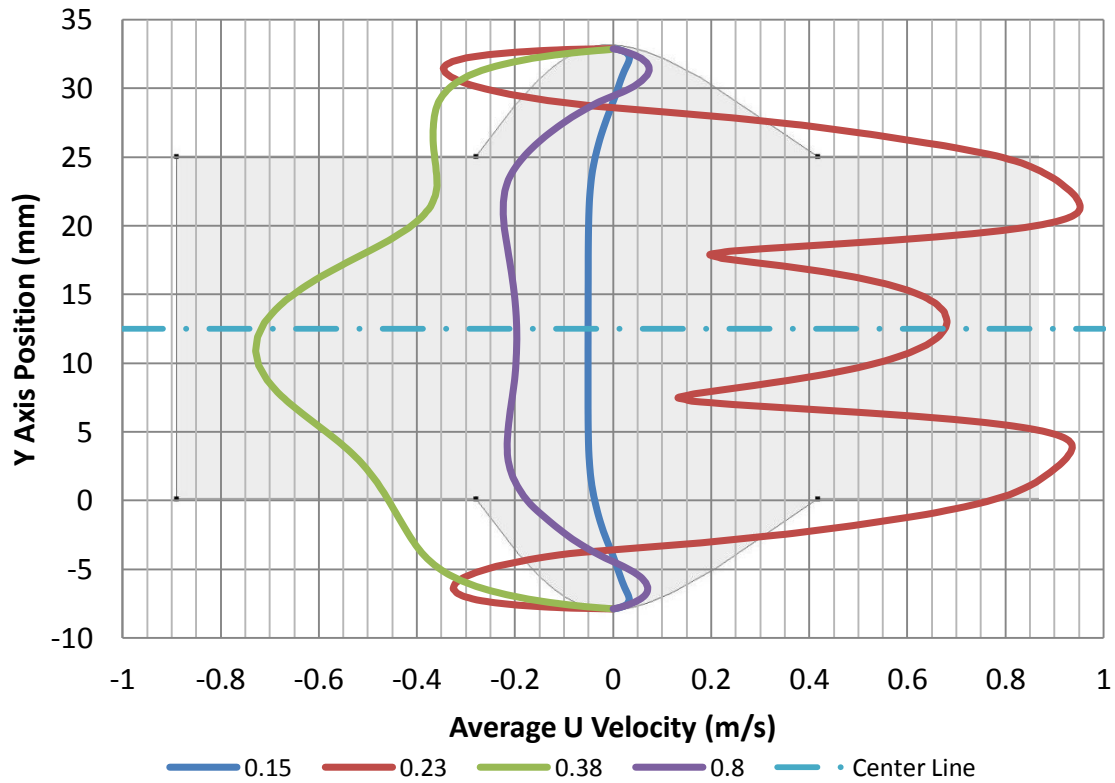
Figure 3.6 Velocity Distribution at 8 mm Downstream from the Base of Aortic Root

In addition to downstream velocity along x-direction across aortic root, the shear stress along the wall of blood vessel is investigated for the probability of blood cell damage during cardiac cycle. The maximum shear stress along the two aortic wall boundaries can be plotted in time, shown in Figure 3.7. As indicated, there are significant peaks for both top and bottom wall, for $6000\ dPa$ and $-3000\ dPa$, at 0.38 s when the valve leaflets closed. On the other hand, the shear stresses during leaflet opening phases have a magnitude near zero, while an average magnitude of $2500\ dPa$ is found during leaflet closed phase. Considering that erythrocytes may sustain a high shear stress of approximately $10^5\ dPa$ under short period of few microseconds, the average magnitude of shear stress experiencing by blood cell should be under a critical value of $1500\ dPa$ with moderate shear stress exposure time[48]. Therefore, it could be suggested, according to Figure 3.7 for maximum shear stress distribution, that blood cell damages would most likely to occur and thrombosis may be presented. In addition to shear stress calculation, simulation time steps are refined to ensure artifacts are resolved around peak shear stress.
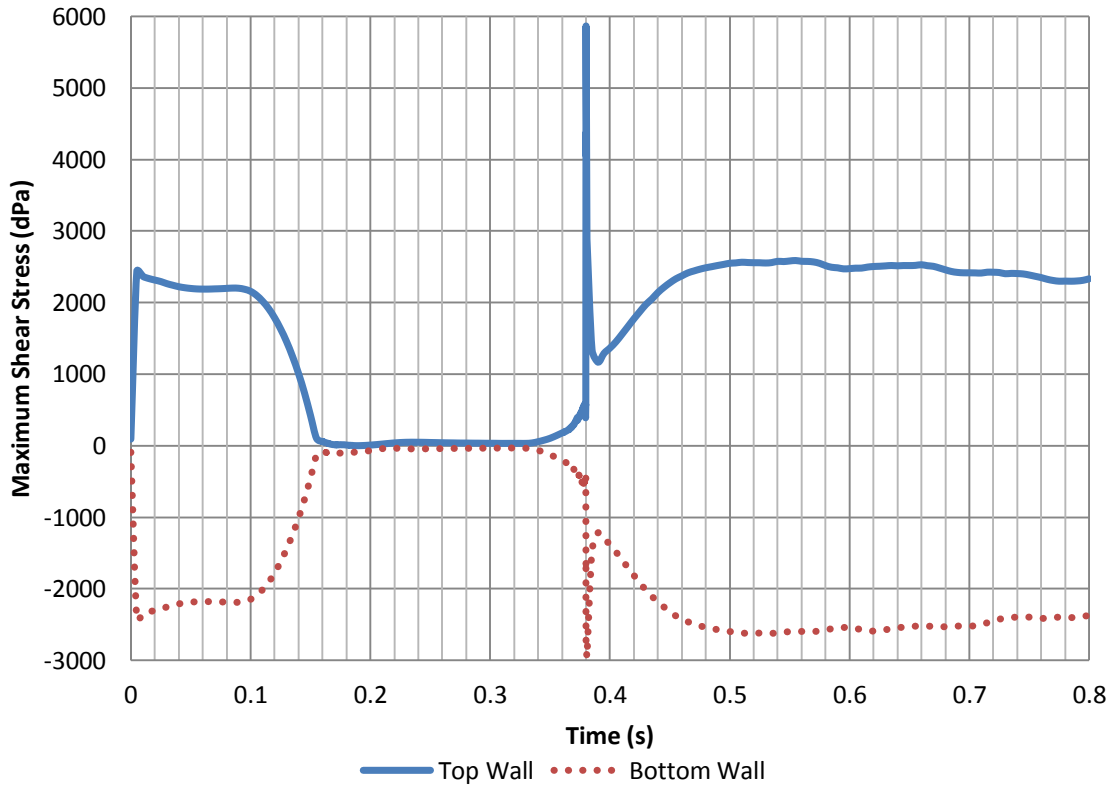

Figure 3.7 Maximum Shear Stress Along Aortic Wall for Rigid Wall Model

3.1.3 Mechanical Valve Leaflet Dynamics

Since the motion of the artificial heart valve leaflet is closely related to the performance of the artificial valve, the second set of processed results from FSI models are the determination of structure dynamics for mechanical valve leaflets throughout one cardiac cycle. As mentioned in the Method section, given that the computational domain is constructed with a geometrical symmetry, the physical constraints for the mechanical valve leaflet are defined separately in order to capture any asynchronous behavior that might be caused by the possible occurrence of transition flow during peak systole. There is, however, one limitation for the activation of physical constrain on valve leaflets. Since the method is to activate the constraints when the current angular position is beyond limitation, an overshoot in leaflet position could be observed due to the time lag in constrain activation.

With the time history for mechanical valve leaflet motion during one cardiac cycle plotted in Figure 3.8, the leaflet dynamics can be closely investigated and discussed. As the initial-opening phase starts at $0.15\,s$ when the pressure gradient across the mechanical valve is approximately equal to zero, the forward flow increase rapidly due to the sudden increase in pressure gradient from $0.15\,s$ to $0.23\,s$. Given this rapid ejection period of $80\,ms$, the valve leaflets are able to reach to maximum opening position at $0.23\,s$ from the fully closed position at $0.15\,s$. The valve leaflets are then maintained at fully opened position for approximately $110\,ms$ from $0.23\,s$ until an approximated time of $0.34\,s$. The valve leaflets are then reached to a fully closed position when the time reached to $0.38\,s$ due to large negative pressure difference across the valve forcing the leaflet to be closed rapidly for a closing period of $40\,ms$.
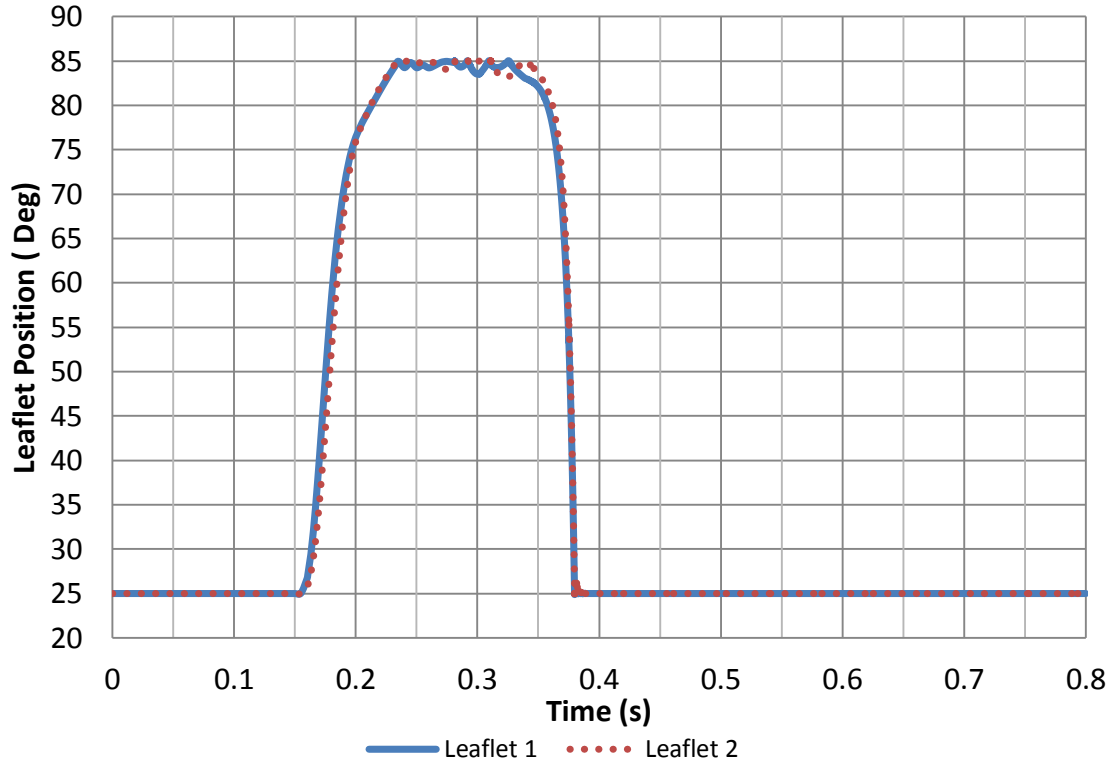
Figure 3.8 Rigid Wall Mechanical Valve Leaflet Dynamics for One Cardiac Cycle

The overall duration for the valve leaflets remain opened is approximately equal to 230 ms, from 0.23 s to 0.38 s; while the overall duration for the valve leaflets remain closure is approximately equal to 570 ms. In addition to general leaflet dynamics, Figure 3.9 shows two region of interest that reveals leaflet instability during cardiac cycle. The instability for the period when valve leaflets maintain at fully opened position, shown in Figure 3.9(a), occur after the peak-opening phase of 0.23 s as the leaflet position constraints are activated once the leaflet reached the maximum opening angle of 85 degree. Since the blood flow during the maximum leaflet opening period would be the maximum throughout the whole cardiac cycle, the instability is most likely caused by the flow entering transition region due to high central velocity jets, shown in Figure 3.6 at 0.23 s, around mechanical valve leaflet. It is noted that the instability during peak-opening phase could only be reproduced under an additional refined mesh configuration. This further suggests that small scale vortices due to transitional flow could be captured

under finer mesh grids; therefore, in order to capture vortices in all scale, a DNS model will be necessary. On the other hand, the instability around the end-opening phase shown in Figure 3.9(b) have a different cause since the flow velocity is lower right after the closure of valve leaflets at 0.38 s. Since physical constraints are applied instantaneously whenever the leaflet positions pass beyond the constrained angles in order to limit the minimum and maximum leaflet position, a large counter moment is applied to the valve leaflets such that the constrained boundaries at the joints of valve leaflet receive a large reaction force. Therefore the leaflets are modeled as striking against hard surface and resulting in leaflet rebounds, such as shown in Figure 3.9(b). As mentioned previously, this method does not require any additional geometrical complexities; however, the method introduces a small time lag in order to determine the precise time to activate counter moment. The delay of counter moment activation could be observed in both Figure 3.9(a) and (b) at the time when leaflets reach either maximum or minimum angular position. To address the concern of constrain activation delay in this study, several control parameters are properly adjusted in order to reduce the artifact of position overshoot within an absolute maximum difference of 0.1 degree.

 In addition to leaflet position in time, the stress within valve leaflets can also be calculated based on simulated results. Figure 3.10 shows the maximum von Mises stress within two mechanical valve leaflets over one cardiac cycle on a semi-log plot. It is clearly shown that a peak stress of approximately 100 MPa is generated at the time when leaflets are firstly closed; while the maximum stress for other time periods are approximately below 10 MPa. Since the yield strength of mechanical valve leaflet, which is commonly be constructed with pyrolytic carbon, is approximately 400 MPa; it may be suggested that based on the result shown in Figure 3.10 the valve leaflets are not likely to fail by yielding. Also notice that the stresses within valve leaflet change according to the leaflet instability shown in Figure 3.9(a) during leaflet opening phase.
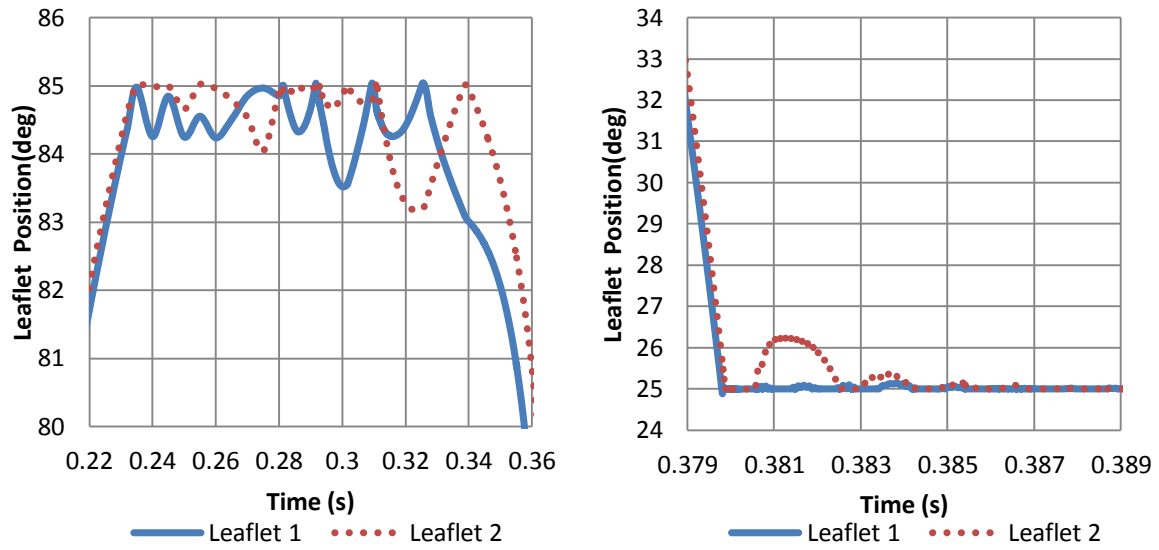
(a) Instability during Valve Fully Opened   **(b)** Instability during Valve Fully Closed

Figure 3.9 Magnified Regions of Mechanical Leaflet Instability
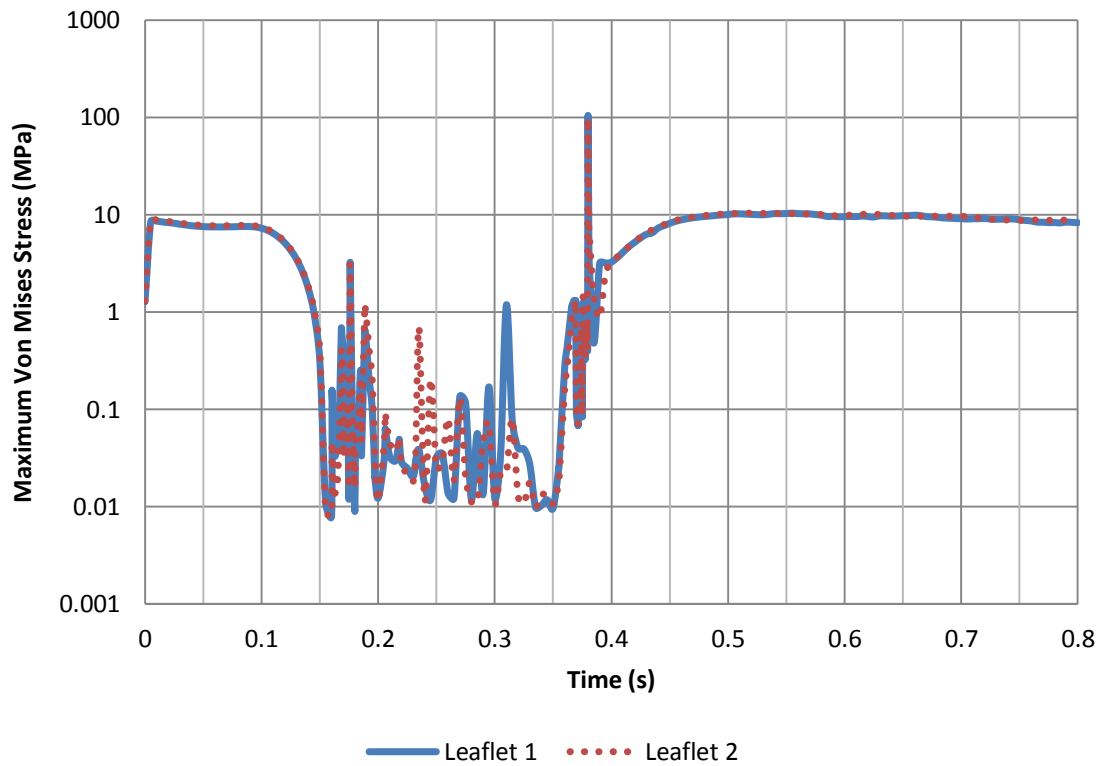
Figure 3.10 Maximum Von Mises Stress within Valve Leaflets for Rigid Wall Model

3.2 Flexible Wall Bileaflet Mechanical Valve

In addition to the rigid wall mechanical valve model presented in previous section, it is possible to extend the same technique and construct a modified model that incorporates the flexibility of arterial wall. Since blood vessel would be distorted during systole and diastole with the possibility of wall oscillations, making the assumption of rigid blood vessel may result in insufficient accuracy comparing with natural blood flow. Therefore, the addition of flexible wall model is introduced in order to estimate the difference between rigid wall model and flexible wall. Similar to previous section, the hemodynamics of the blood flow would be firstly discussed and followed by the structure mechanics of valve leaflets and model comparison.

3.2.1 Blood Flow Hemodynamics

With the identical pressure boundary profiles, shown in Figure 3.4, applied to flexible wall model, the results can also be isolated in the same time frames used in rigid wall model, shown in Figure 3.11, where Figure 3.11 (a) to (d) are velocity contours and Figure 3.11 (e) to (h) are shear stress contours.

Starting with the initial-opening phase at $0.15\ s$, due to the expansion of arterial wall at the aortic portion, the leakage jets from intervalvular space have a higher velocity magnitude compare with rigid wall model. The vortices generated by leakage jets are relatively symmetric and are clearly visible at the ventricular portion behind the valve leaflets. Since the expansion of the vessel wall enlarges the overall volume of backflow, a higher maximum velocity magnitude is presented at this phase with a value of $1.916\ m/s$, compare against with the rigid wall model. Moreover, the shear stress distribution of the computation, shown by shear stress contour plot, also presents a higher maximum shear stress of $1619.6\ dPa$, which is higher than the critical value for blood cell damage.

During the peak-opening phase at $0.23\,s$, further expansion of arterial wall is presented with a maximum flow velocity passing through valve leaflets due to the increase of pressure gradient across mechanical valve. The recirculation of blood flow within realistic aortic root during peak systole is also presented as shown in the rigid wall model. The maximum velocity magnitude is shown to be less than the rigid wall model, which implies that the expansion of arterial wall acts as a flow damper to smooth the high velocity generated by high pressure gradient. The high shear stress distribution during this phase is generally concentrated along valve leaflet surfaces and arterial wall; however, since flow during this phase is smooth without blockage of valve leaflets, the maximum shear stress is much lower than other phases with a value of $691\,dPa$.

At $0.38\,s$ during the end-opening phase, valve leaflets are closed and resulting in leakage jet formations from intervalvular space. A maximum velocity magnitude with a value of $4.112\,m/s$ is generated from leakage jets, which is much lower than the result processed from rigid wall model. The addition of the elastic arterial wall might be one of the factors for the velocity reduction since the expansion of the wall potentially allow higher pressure difference and damp down the velocity magnitude. As for the shear stress results, comparing with the rigid wall model, a lower shear stress is presented around valve leaflets with a value of $3485.5\,dPa$; however, the distribution of shear stress is relatively similar to rigid wall model.

Finally, the leakage jets are stabilized with vortices generated behind valve leaflet at the ventricle portion during the mid-closing phase at $0.8\,s$. A maximum velocity magnitude of $4.345\,m/s$ is generated from leakage jets. Flow at the aortic portion is nearly stalled with a slightly recoiled arterial wall. The vortices within aortic root are relatively small comparing with rigid wall model. The distribution of the shear stress is similar to the previous phase with a decrease of high shear stress near arterial wall; however, unlike the rigid wall model where the shear stress magnitude is decreased from the end-opening phase, the shear stress magnitude remains relatively similar from the end-opening phase with a value of $3516.4\,dPa$.
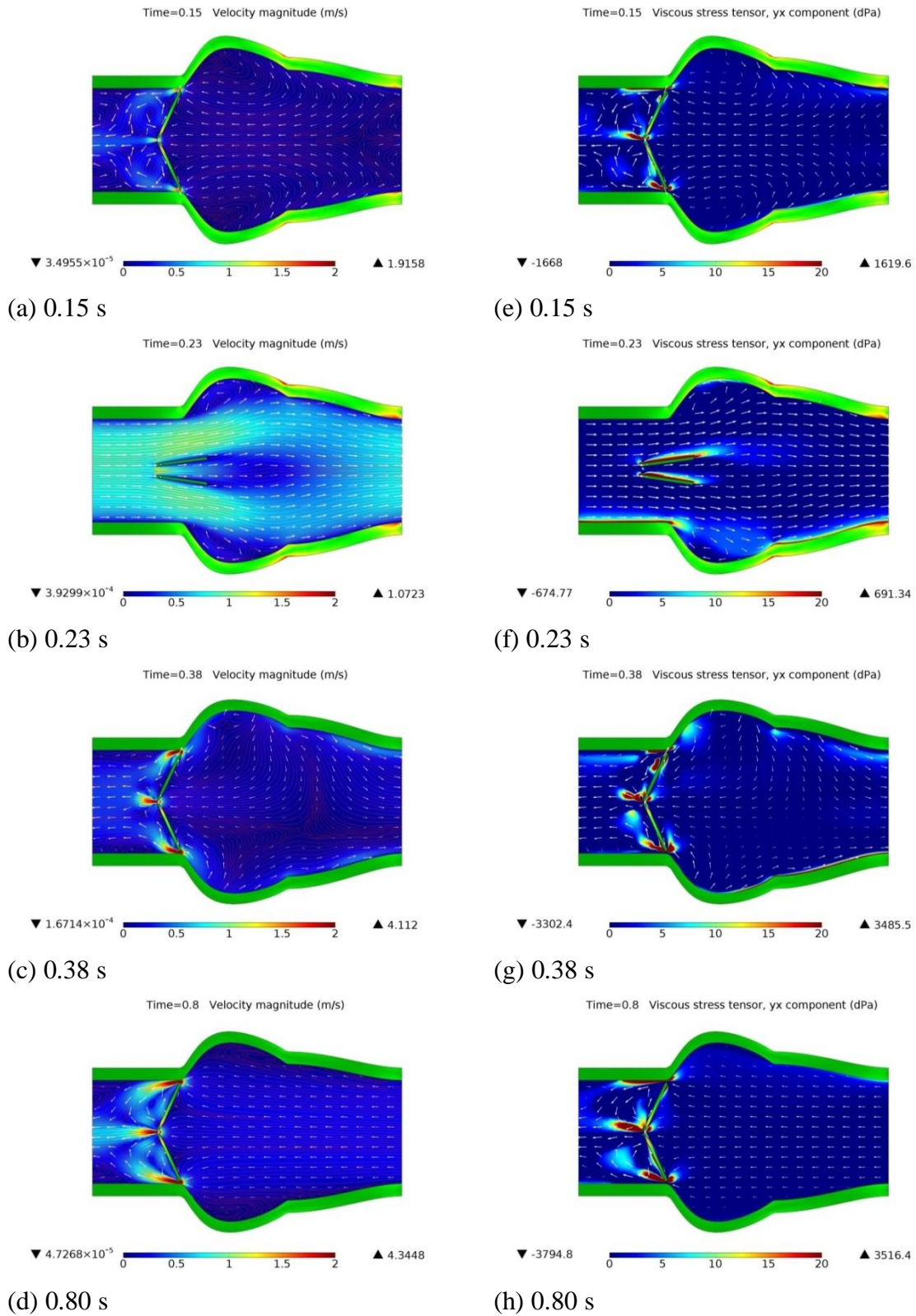
Figure 3.11 Isolated Time Frames during Different Cardiac Phases for Flexible Wall Mechanical Valve

In addition to velocity and shear stress contours for the flexible wall model, the exact velocity profile can be calculated at $9\ mm$ downstream away from the valve leaflet. Shown in Figure 3.12, a small back flow with a velocity of $-0.1\ m/s$ occurs at $0.15\ s$ during the initial-opening phase. The peak velocity occurs at $0.23\ s$ with an approximately value of $0.93\ m/s$ around the tip of valve leaflet and an approximately value of $0.45\ m/s$ between valve leaflets. The recirculating blood flow within aortic valve has a minimum velocity of $-0.25m/s$ during the peak-opening phase. During valve leaflet closure at $0.38\ s$, the unsteady velocity range from $0.1\ m/s$ within aortic root to $-0.15\ m/s$ within central leakage jet. In addition, during mid-closing phase at $0.80\ s$, a relatively steady back flow velocity with an approximate value of $-0.2\ m/s$ is generated due to back pressure from aorta. Notice that during closing phases at either $0.15\ s$ or $0.80\ s$, the recirculating blood flow within aortic root is at minimum, unlike the forward and backward unsteady flows, which generate vortices within aortic root.
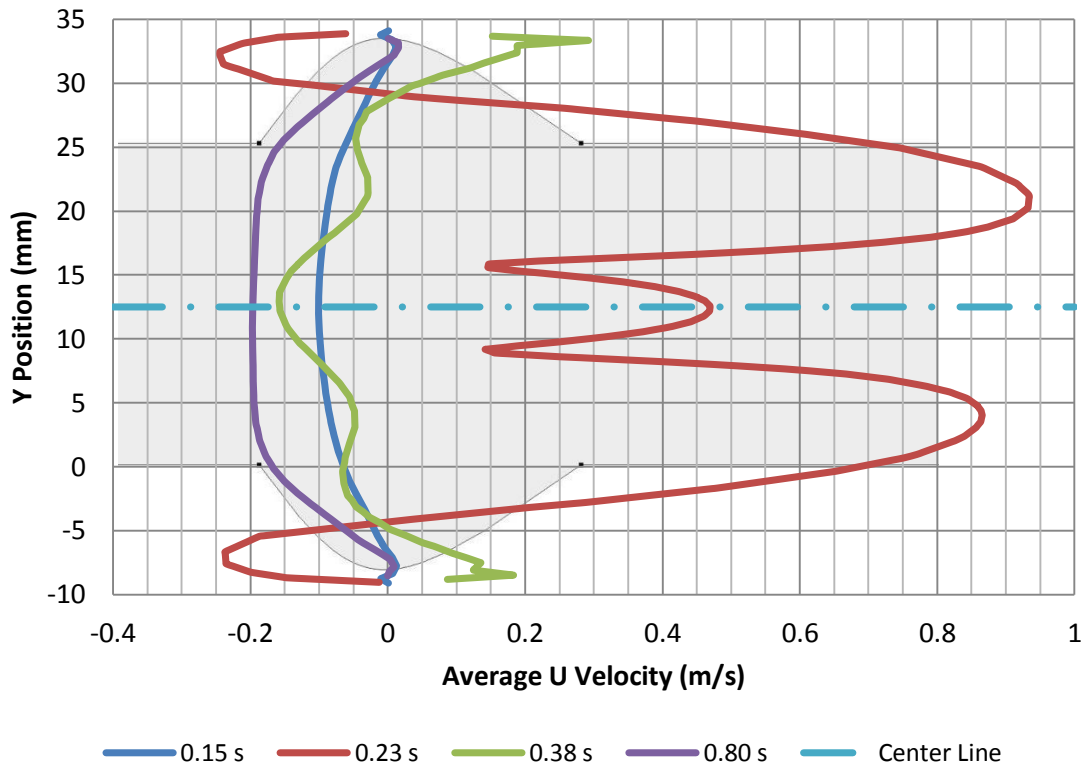
Figure 3.12 Velocity Distribution at $8\ mm$ Downstream from the Base of Aortic Root

Moreover, the shear stress along arterial wall can be calculated and analyzed in time. Plotted in Figure 3.13 is the shear stress profile along the top and bottom arterial wall for the computational domain. With a similar shear stress profile compare to the rigid wall model, higher shear stress is distributed mostly during the leaflet closing phase. However, note that the magnitude of the shear stress is slightly lower than the rigid wall model, presented in Figure 3.7, with a peak shear stress magnitude of 3000 dPa. In addition to the lower shear stress distribution for flexible wall model, the profile, shown in Figure 3.13, has some oscillatory behavior except for the fully opened phase from $0.15\ s$ to $0.38\ s$. The oscillation is caused by the deformation and vibration generated by the motion of arterial wall since a large pressure difference is introduced at the beginning of cardiac cycle and at the time when leaflet firstly closed. The first set of oscillation at the beginning of cardiac cycle could potentially be minimalized by simulating with multiple continuous cardiac cycles at a cost of computational resource such that the difference between each cycle would be minimalized.
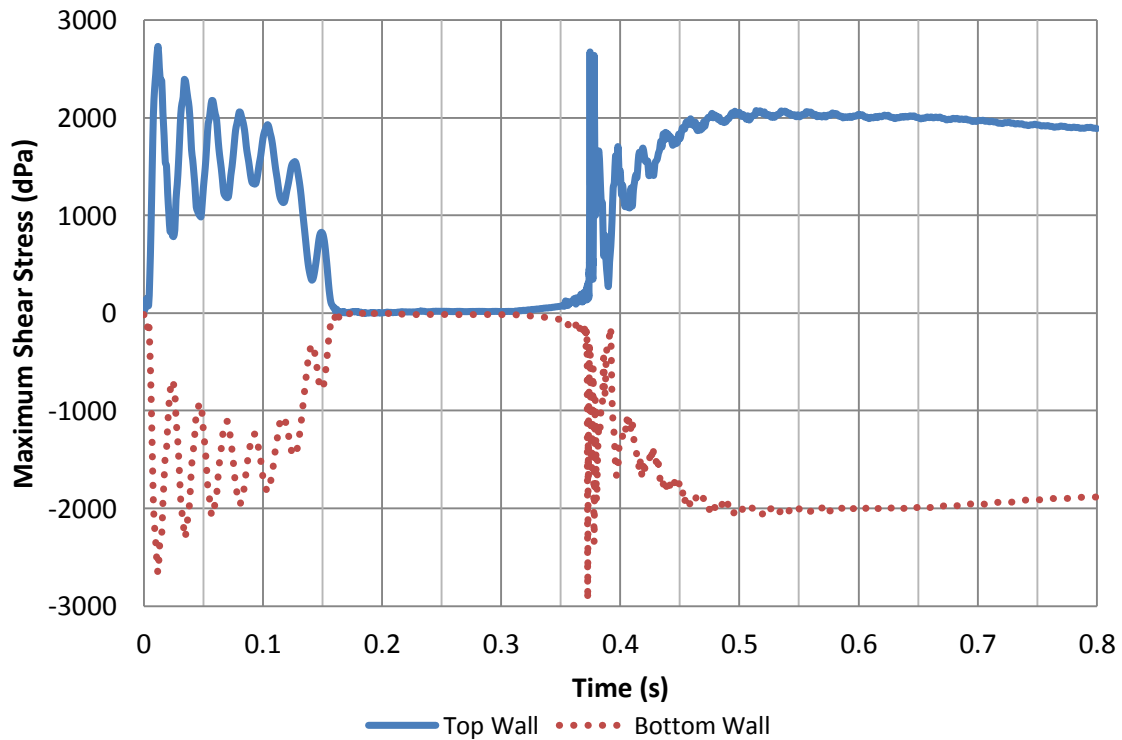
Figure 3.13 Maximum Shear Stress Along Aortic Wall for Flexible Wall Model

3.2.2 Mechanical Valve Leaflet Dynamics

As discussed previously, valve leaflet position history is related to the hemodynamics of artificial heart valve. Figure 3.14 presents the position of valve leaflets in time. Similar to the rigid wall model, the approximate time for leaflets to be fully opened is $100 \, ms$ with both leaflets start to open around $0.15 \, s$ and become fully opened around $0.25 \, s$, which is slightly slower. The approximate time for leaflet to maintain opened is $100 \, ms$ from $0.25 \, s$ to $0.35 \, s$. In addition, the approximate time for leaflet to be fully closed is $30 \, ms$ with leaflets closed at $0.38 \, s$. Finally, the time for leaflets remaining fully closed is approximately $570 \, ms$ for the rest of the cycle. Rebound is occurring when the leaflets closed at $0.38 \, s$ with an absolute maximum position overshoot of 0.03 degree, which is significantly better than rigid wall model, possibly due to lower velocity at leaflet closure.
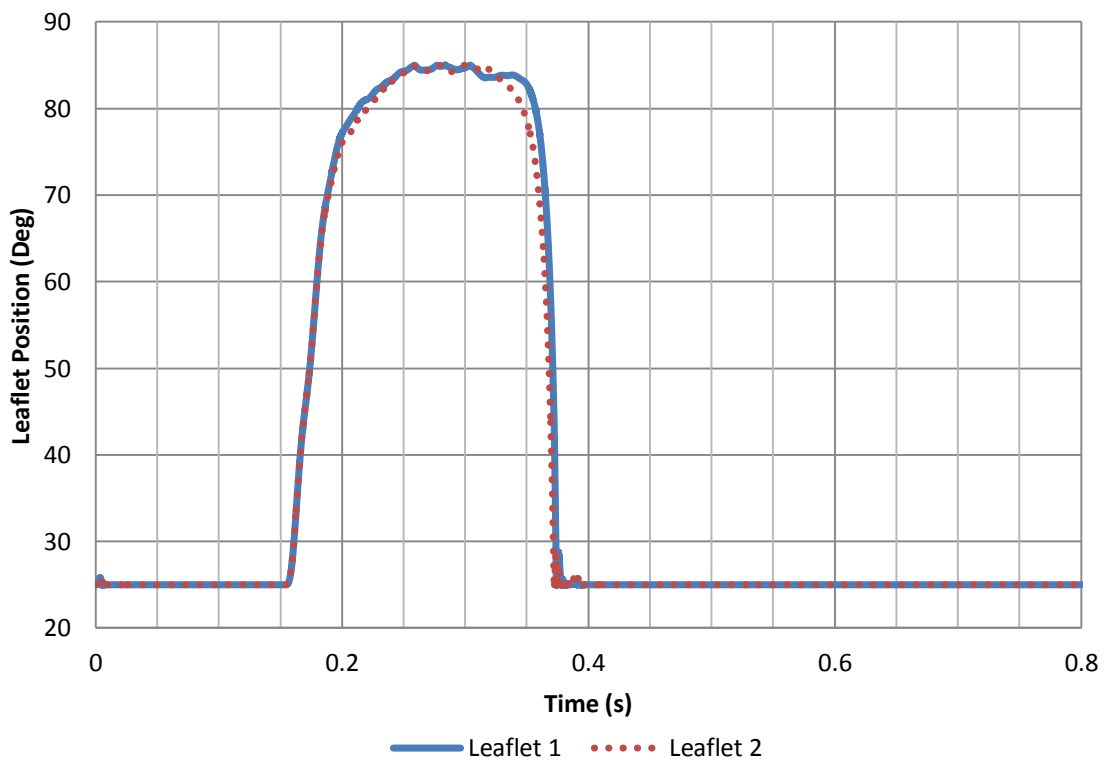
Figure 3.14 Flexible Wall Mechanical Valve Leaflet Dynamics

Regarding the stress within the valve leaflet, the stress profile is plotted in Figure 3.15 and reveals similar findings with the leaflet dynamics discussed previously. Oscillation in maximum von Mises stress, which is caused by unsteady initial pressure difference, can be found during the period when leaflets are closed. The peak maximum stress can still be found at the time when leaflets are firstly closed at $0.38\ s$ while the maximum von Mises stress maintains roughly below $10\ MPa$ throughout cardiac cycle. The magnitude of the stress is smaller compared with the rigid wall model, implying that the leaflet from the flexible wall model would be more unlikely to fail by material yielding.
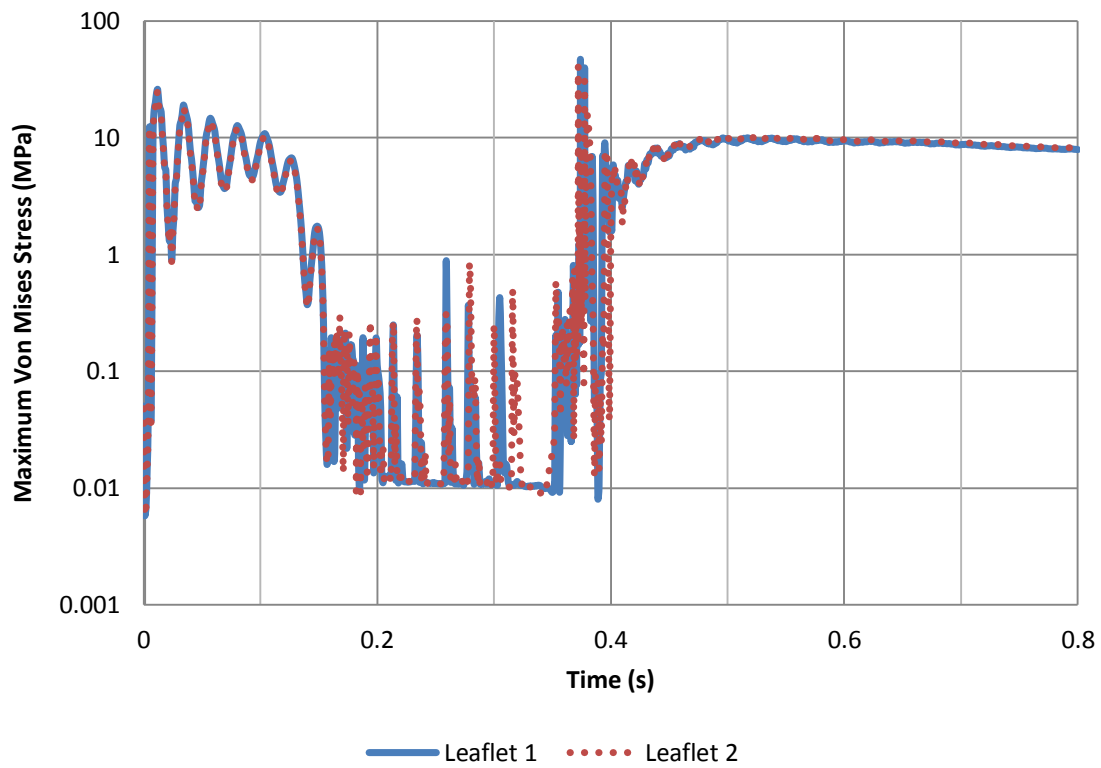
Figure 3.15 Maximum Von Mises Stress within Valve Leaflets for Flexible Wall Model

3.2.3 Model Comparison

In order to compare the hemodynamic performance between the rigid and flexible wall model, a distinct comparison is conducted by evaluating the difference between the velocity fields for each isolated time frame shown in Figure 3.16 (a) to (d). At $0.15\ s$, in Figure 3.16(a) during the initial opening period, both models have a velocity profile with a small value between $0\ m/s$ to $-0.1\ m/s$ with minor velocity difference in between. At $0.23\ s$, in Figure 3.16(b) during the peak opening period, the velocity magnitudes of the two models remain relatively similar with an approximate maximum forward velocity of $0.9\ m/s$; however, the distribution of velocity profile between the models have a significant difference. Due to the inclusion of the wall flexibility, blood recirculation within aortic root is decreased and shifted outward by wall expansion. The central velocity jet between valve leaflets for flexible wall model has a decreased width and a decreased velocity magnitude by $0.3\ m/s$ to $0.45\ m/s$; therefore, the velocity distribution is increased on the other side of the leaflets. At $0.38\ s$, in Figure 3.16(c) during the end opening period, the flexible wall model has a significantly lower velocity profile, with a peak value of $-0.15\ m/s$, compare against the rigid wall model, which has a peak velocity of $-0.72\ m/s$, along the central leakage jet. At $0.80\ s$, in Figure 3.16(d) during the mid-closing period, the difference in velocity for both models is decreased and only the rigid wall model presents minor recirculation within aortic root. Given the difference presented in Figure 3.16, it is noticed that the velocity magnitude for flexible wall model is generally less than the rigid wall model; therefore, it is possible that an over estimation in hemodynamic performance is obtained from the rigid wall model.
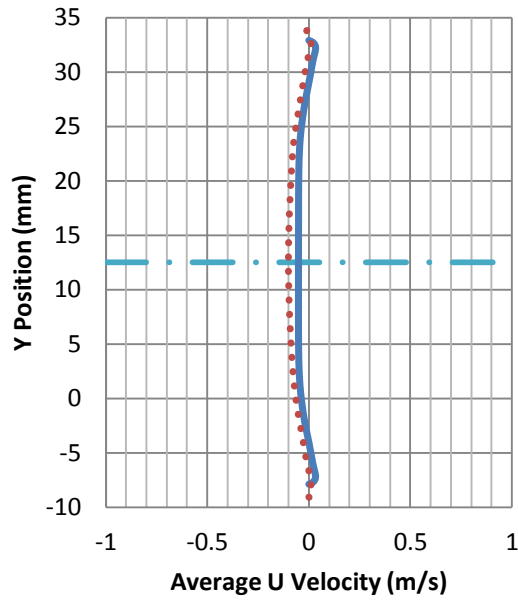
a) 0.15 s
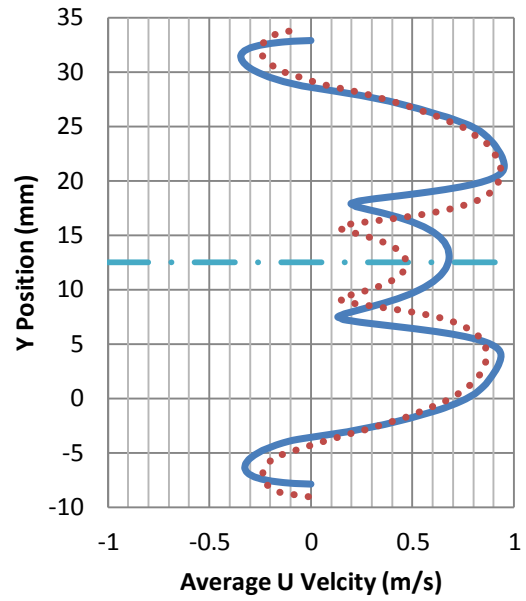
b) 0.23 s
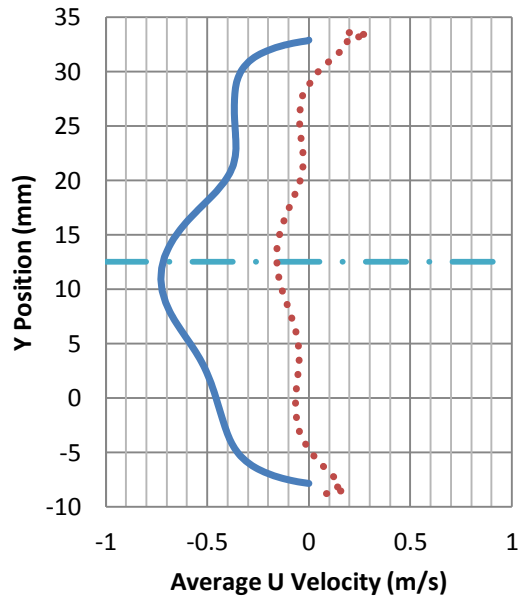
c) 0.38 s

d) 0.8 s

—Rigid —Flexible — ·Center Line

Figure 3.16 Velocity Field Comparisons Between Rigid and Flexible Wall Model
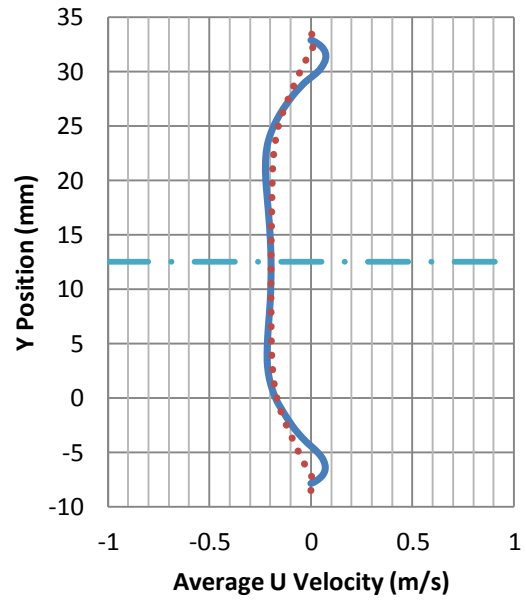
3.3 Clinical Application

Since there are two different bileaflet mechanical valve models introduced, with the flexible wall model modified from rigid wall model, a systematic comparison between two similar models has been conducted in order to investigate the significance of making rigid wall assumption. Furthermore, with the computational models on bileaflet mechanical valve fully described, the secondary objective of the study is to investigate clinical applications using the constructed CFD FSI models.

Although the bileaflet mechanical heart valve is known for its outstanding durability, there are some major clinically complications such as valve leaflet malfunctions, which would require surgical reoperation depending on the severity of each scenario. Among several different causes that lead to different severities in the decrease of hemodynamic performance for artificial heart valve due to leaflet malfunction, a total valve leaflet restriction caused by pannus formation after operation might leads to series of long term complication. Therefore, simulations could be conducted in order to investigate similar scenarios and provided additional information on flow characteristics such that the pattern of the flow could be used as supporting evidences. Shown in Figure 3.17, the rigid wall model, Figure 3.17 (a) to (d), and flexible wall model, Figure 3.17 (e) to (h), are modified with one of the valve leaflet totally constrained such that the total blockage can be simulated, which reflects the worst case scenario in valve malfunction.

Given that the only difference between the malfunction models and the normal models is the restriction of bottom leaflet, the flow profiles for the malfunction models have similar results compare against with the normal models. Presented in Figure 3.17 (a) and (e) for the initial-opening phase, two vortices are generated behind the leaflets in the ventricular portion similar to the normal models since the leaflets have not yet be opened. In Figure 3.17 (b) and (f) for the peak-opening phase, velocity jet is passing through the free rotation leaflet and generating smaller vortices due to leaflet blockage. The velocities for the malfunction models are slightly higher than the normal models due to smaller

opening of the valve. Recirculation of blood flow only occurs in the aortic root close to the opening leaflet while the aortic root near the malfunction leaflet has a minimum recirculation. There are two vortices generated in front of the malfunction leaflet in aortic portion for the rigid wall model shown in Figure 3.17 (b). The flexible wall model, shown in Figure 3.17 (f), has a third vortex generated due to the forward leakage jet produced by the intervalvular space between the malfunction leaflet and arterial wall.

(a) 0.15 s

(b) 0.23 s

(c) 0.38 s

(d) 0.80 s

(e) 0.15 s

(f) 0.23 s

(g) 0.38 s

(h) 0.80 s
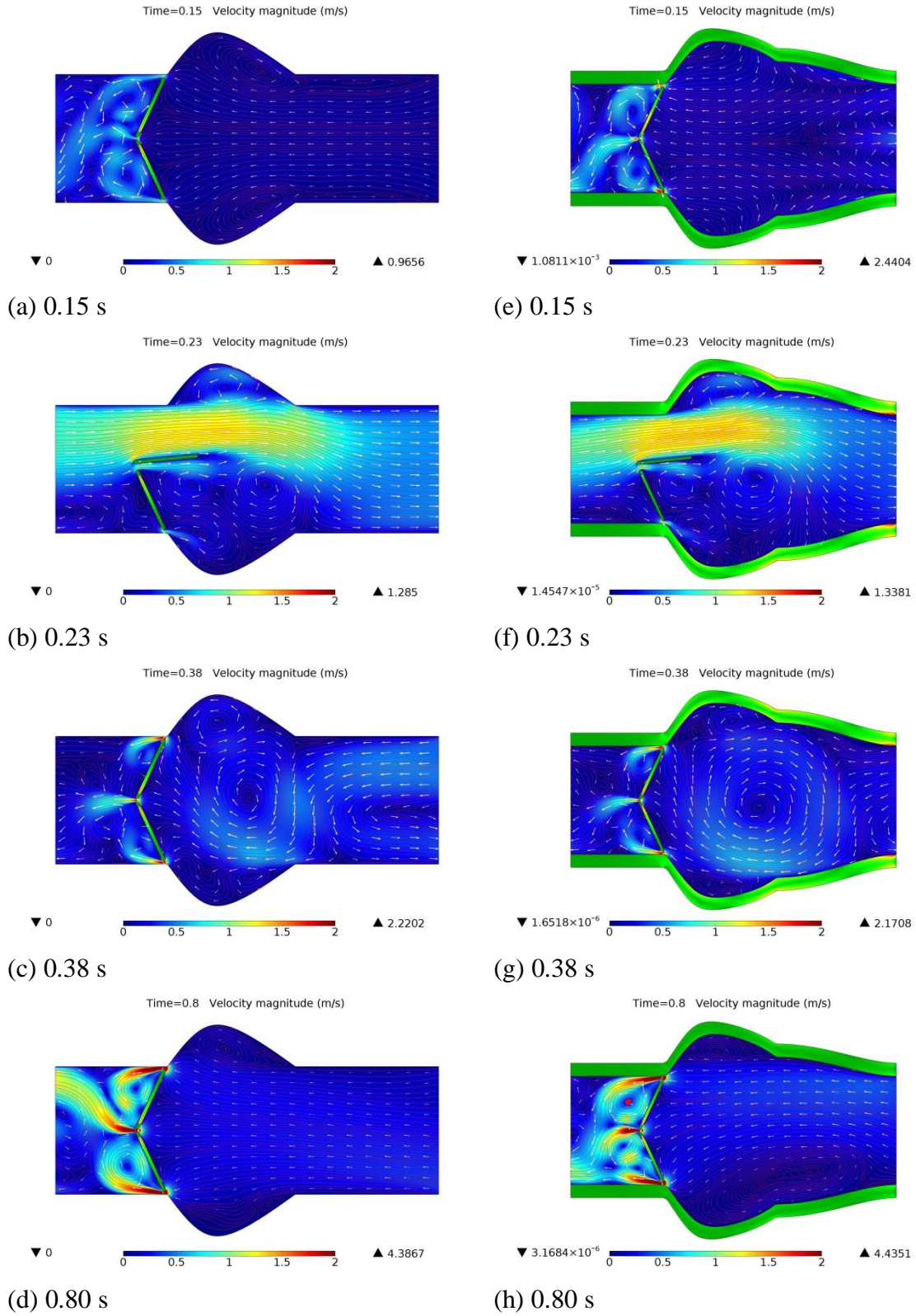
Figure 3.17 Velocity Contour for Rigid and Flexible Wall Model with Leaflet Malfunction

In addition, for the end-opening phase in Figure 3.17 (c) and (g), a large vortex is formed and sustained a non-zero velocity field at the center of aorta near aortic root with two smaller vortices located within aortic root. Comparing with the rigid wall model, the expansion of arterial wall is suppressing the two smaller vortices toward to arterial wall, which leads to wider central vortex. Nevertheless, for the mid-closing phase in Figure 3.17 (d) and (h), velocity fields generate similar distributions compare with normal model although the flexible wall model is indicating additional vortices formation behind the valve in ventricular portion. Overall, the simulations on malfunction valve have identified additional vortices formation during cardiac cycle due to asymmetric leaflet position.

3.4   Chapter Summary

In summary, two distinct FSI models are constructed in order to gain additional information with the use of CFD. Furthermore, experimental validation and mesh convergence studies are conducted in order to ensure solution accuracy and relevance. The first model is built with the assumption of rigid arterial wall, which is widely assumed in various articles and the second model is built without applying the assumption of rigid wall. Velocity and shear stress contours are firstly plotted in order to identify several flow features such as vortices. Specific velocity profiles and shear stress distributions are then presented with additional details and discussions. Additionally, the studies of structure dynamics on valve leaflets are also completed with leaflet position history for valve performance and maximum internal stress distribution for failure analysis. Nevertheless, comparisons between the rigid wall and the flexible wall model are conducted by investigating the hemodynamic performance given the same location and time. Based on the results processed, it is suggested that mechanical valve model with rigid wall assumption calculates a higher velocity profile for all four isolated time frames investigated in this study. Therefore, the hemodynamic performance for rigid wall model might conclude with an over estimated results. Finally, a major clinically relevant scenario is investigated by rebuilding the computational model with a total one-leaflet malfunction mechanical valve.

Chapter 4

Results and Discussions for Bioprosthetic Valve

In addition to the bileaflet mechanical valve discussed in previous chapter, FSI simulations for bioprosthetic tissue valves are also conducted with both rigid and flexible wall models presented in this chapter. The flow characteristic and hemodynamic performance, including flow velocity and shear stress distribution, is firstly discussed. In addition to the hemodynamic performance, leaflet position and maximum structure stress profile regarding the leaflet structure dynamics for each model are going to be discussed. Moreover, an investigation of the difference in hemodynamic performance due to the change of material properties caused by sclerosis, which is the hardening of valve leaflet and blood vessel, is conducted. Isolated changes in tissue valve stiffness and arterial wall stiffness are conducted separately. Given that the simulation is conducted using FSI technique that required a consistent computational domain for both fluid and structure, few severe computational limitations, such as maintaining overall geometrical topography and domain continuity, must be satisfied. Therefore, the simulations on bioprosthetic valve would focus on systolic period of the cardiac cycle.

4.1 Rigid Wall Bioprosthetic Tissue Valve

Starting with the hemodynamic performance and followed by structure dynamics, the results for tissue valve model with the assumption of rigid arterial wall are firstly discussed.

4.1.1 Blood Flow Hemodynamics

Given the computational limitations, only the peak-opening phase and end-opening phase is investigated for the models of tissue valve, shown in Figure 4.1. The velocity contours, plotted in Figure 4.1 (a) and (b), and shear stress contours, plotted in Figure 4.1 (c) and (d), are presented with isolated time frames at peak-opening phase and end-opening phase. The maximum velocity magnitude for peak-opening phase at $0.23\,s$ is $1.31\,m/s$, which is slightly higher than mechanical valve model. There are also two recirculation vortices generated within aortic root with the vortex center shifted further downstream. The shear stress distribution, on the other hand, is lower than mechanical valve model with an approximate maximum magnitude of $410\,dPa$. The maximum velocity magnitude for end-opening phase at $0.35\,s$ is approximately $0.88\,m/s$, which is lower than mechanical valve model, around backward flow with lower velocity distributed in aortic root. The two recirculation vortices are shifting toward the base of aortic sinus and further enhancing blood circulation. Furthermore, the shear stress distribution during this period has a lower value than peak-opening phase with an approximate magnitude of $180\,dPa$. Overall, based on the contour plots, the velocity during peak opening period of the cardiac cycle is higher than mechanical valve while the shear stress distribution is much less. Provided that the difference in velocity and shear stress between mechanical valve and tissue valve, the hemodynamic performance for tissue valve is better than mechanical valve.

(a) 0.23 s

(c) 0.23 s

(b) 0.35 s

(d) 0.35 s
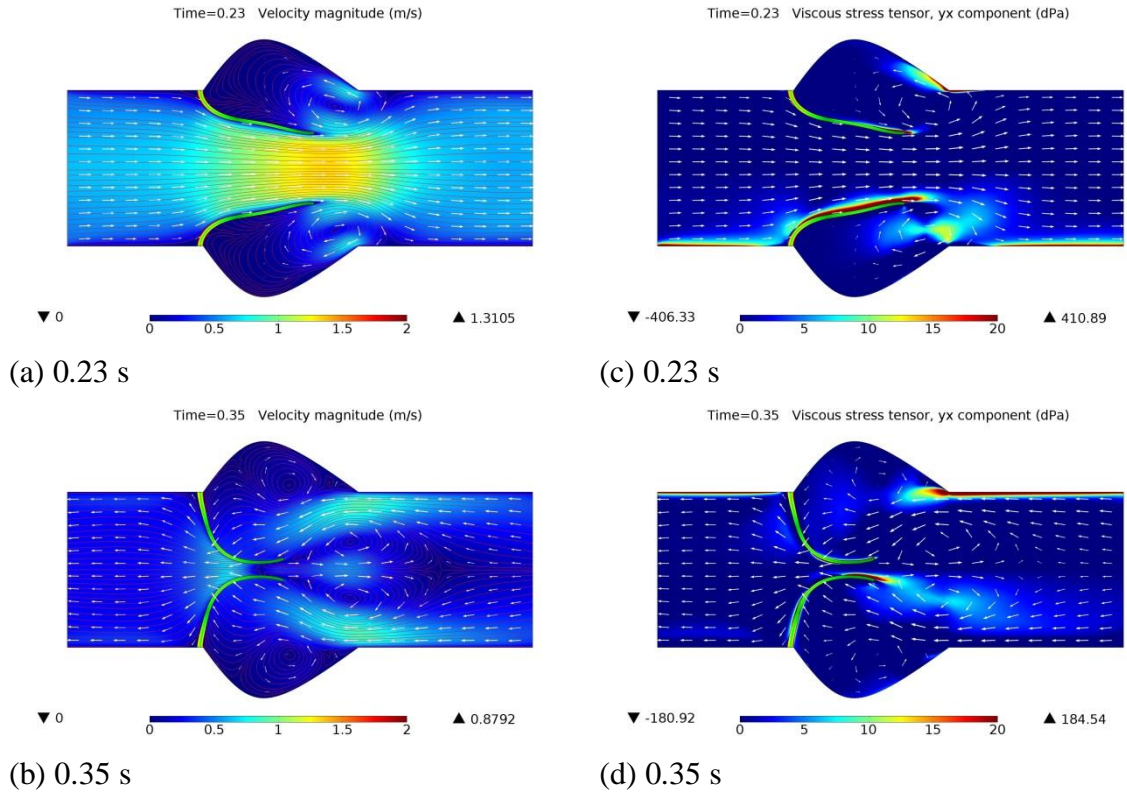
Figure 4.1 Isolated Time Frames during Different Cardiac Phases for Rigid Wall Tissue Valve

In addition to contour plots shown in Figure 4.1, the exact downstream velocity profiles can be calculated, shown in Figure 4.2. The maximum velocity at $0.23\ s$ is approximately $1.05\ m/s$ given that a concentrated central velocity jet with a diameter of $15\ mm$ is ejected. This diameter of central velocity jet can be defined as the ejection width in order to conduct comparison between different models. Minimum recirculation is found during this period, as shown in Figure 4.1, that vortex centers are shifted further downstream. The maximum velocity at $0.35\ s$ is approximately $-0.34\ m/s$, which is slightly higher due to two tissue valve leaflets collapsing at the center of the flow. A minor recirculating velocity is present during this period as the vortex centers are moving into aortic root due to backward flow. Comparing the velocity profile between tissue valves against mechanical valve, it can be notice that although tissue valve produces higher central velocity, the velocity distribution is highly depended on the maximum

78

opening of tissue valve leaflets, which is related to material properties and leaflet thickness.
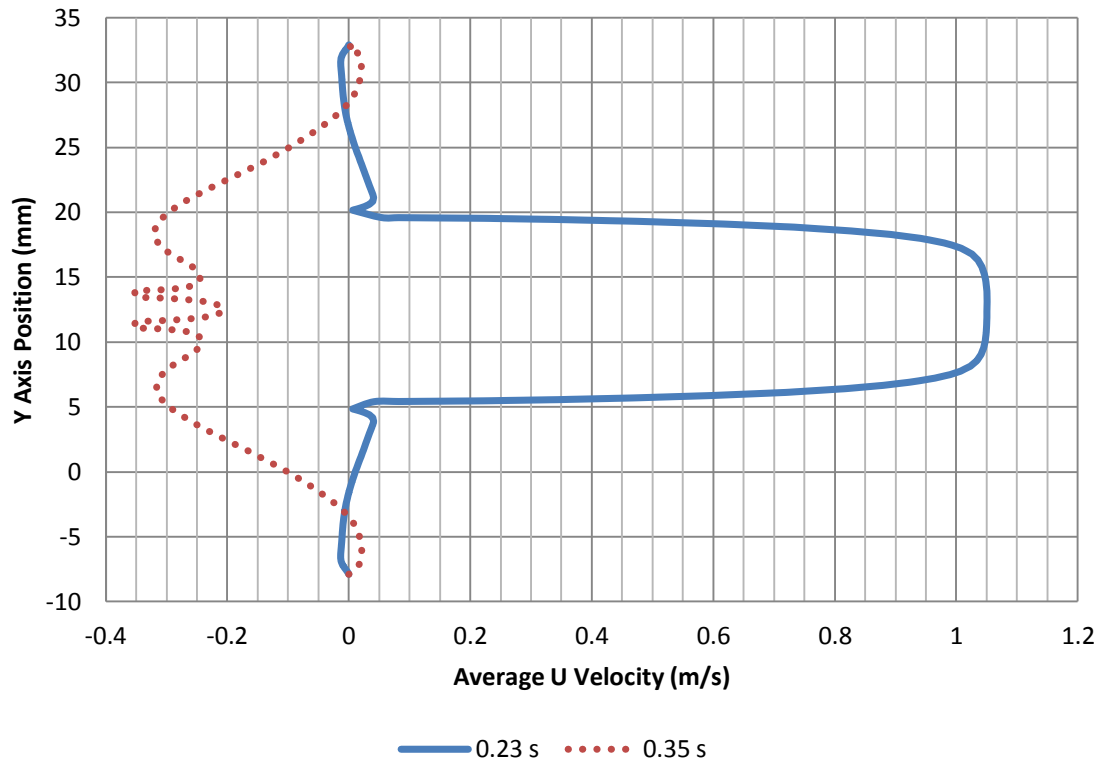
Figure 4.2 Velocity Distribution at 8 mm Downstream for Rigid Wall Tissue Valve

Nevertheless, the maximum shear stress along the wall can be plotted in order to investigate the possibility of blood cell damage, shown in Figure 4.3. The shear stress calculated for tissue valve is significantly lower with a maximum magnitude of $460\ dPa$ instead of $6000\ dPa$ in mechanical valve model, which implies that the anticoagulant therapy might not be necessary as the critical shear stress of $1500\ dPa$ is not reached. However, given that only systolic period is simulated for tissue valve model, the actual maximum stress throughout the whole cardiac cycle might be higher.
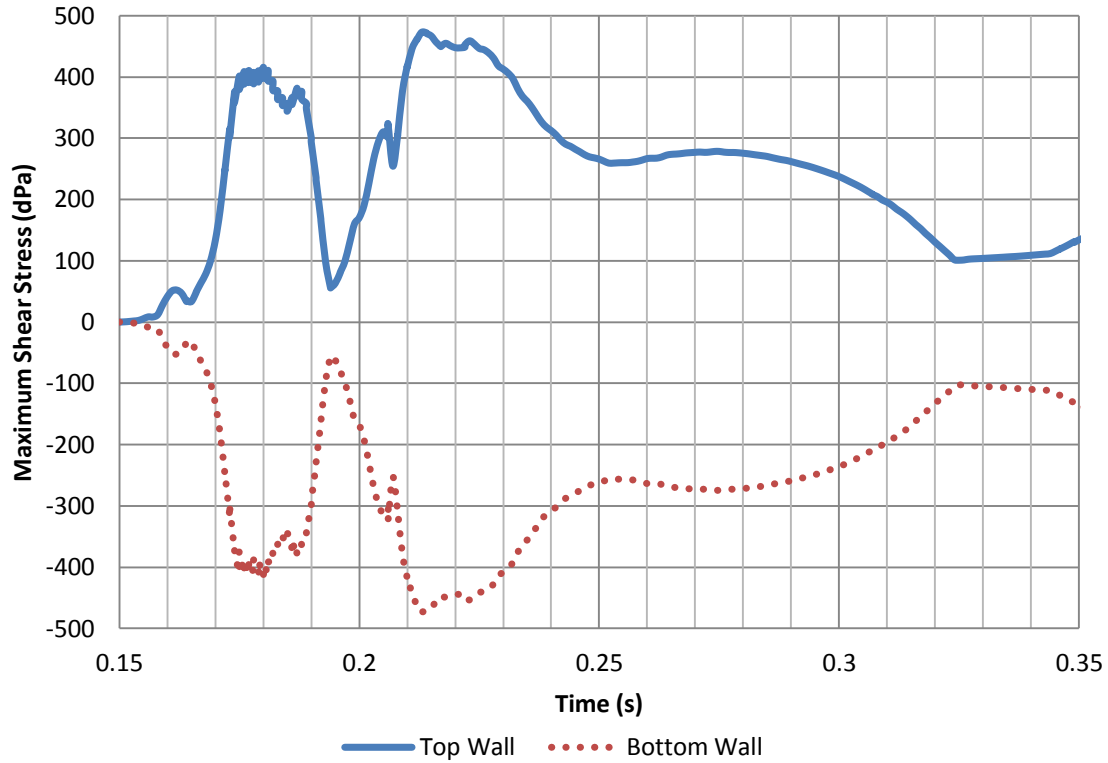
Figure 4.3 Maximum Shear Stress Along Aortic Wall for Rigid Wall Tissue Valve Model

4.1.2   Tissue Valve Leaflet Dynamics

Unlike the bileaflet mechanical valve model which has a well-defined leaflet dynamics in terms of degree of rotation, the leaflet motion for tissue valve model is based on leaflet displacement. Therefore, to characterize tissue valve dynamics, the maximum displacement for valve leaflets away from the center of the computational domain is plotted in Figure 4.4. It is shown that both leaflets take approximately $50\ ms$ in order to reach a maximum displacement of $9.6\ mm$ at $0.2\ s$. The displacement is decreased and maintained at approximately $5\ mm$ until $0.27\ s$ after the peak leaflet displacement. Finally, the leaflets are returning to initial position and closed at approximately $0.35\ s$; however, the actual time of closure will be several milliseconds later and cannot be simulated with presented technique since solution would diverge with inverted mesh element when leaflet displacement approaches to zero.
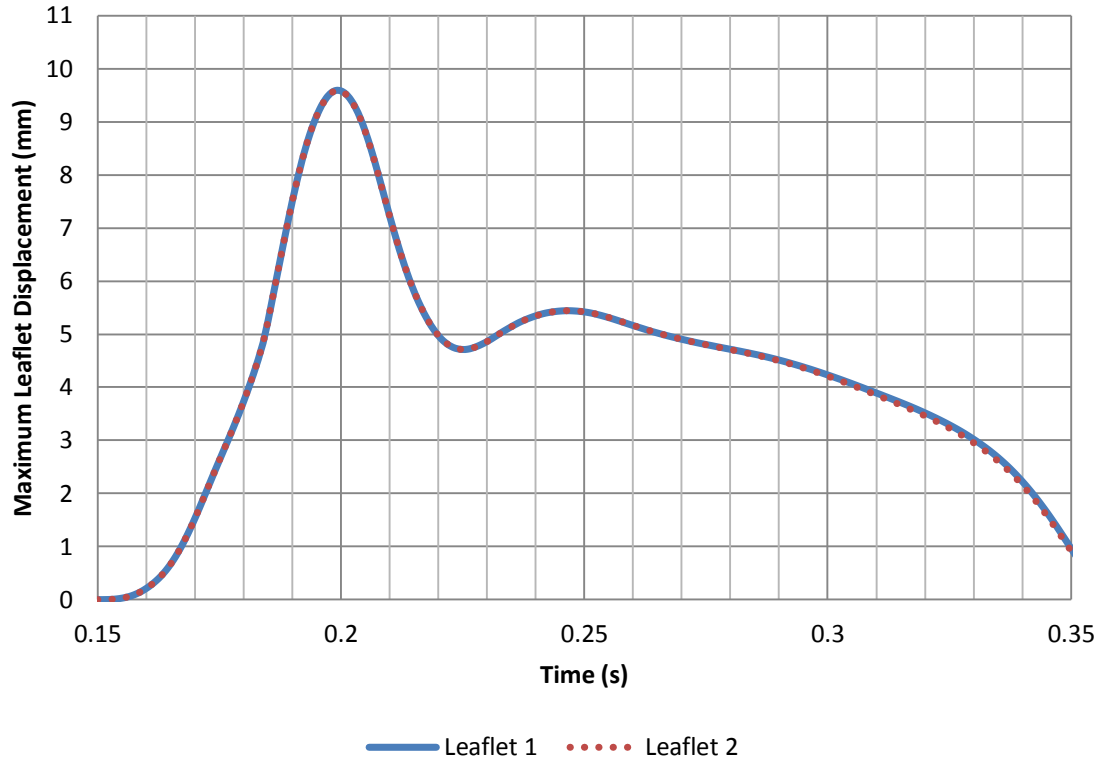
Figure 4.4 Rigid Wall Tissue Valve Leaflet Dynamics

Additional investigation regarding to structure stress within valve leaflet is presented in Figure 4.5. The overall von Mises stress during the systolic period, prior to leaflet closure at $0.32\ s$, is roughly below an approximate magnitude of $0.1\ MPa$ with peak stress of 0.112 MPa at $0.18\ s$. Although the absolute maximum von Mises stress cannot be calculated for whole cardiac cycle, the maximum value during systolic period is calculated to be approximately $0.139\ MPa$ at leaflet closure. Given that tissue valve model is conducted only for systolic period, comparison against with the mechanical valve model can be conducted with the same time frame. Since tissue valve is experiencing much larger deformation then mechanical valve due to smaller Young's modulus, the maximum stress for tissue valve is slightly higher than the averaged maximum stress for mechanical valve due to material bending at the base of valve leaflets.
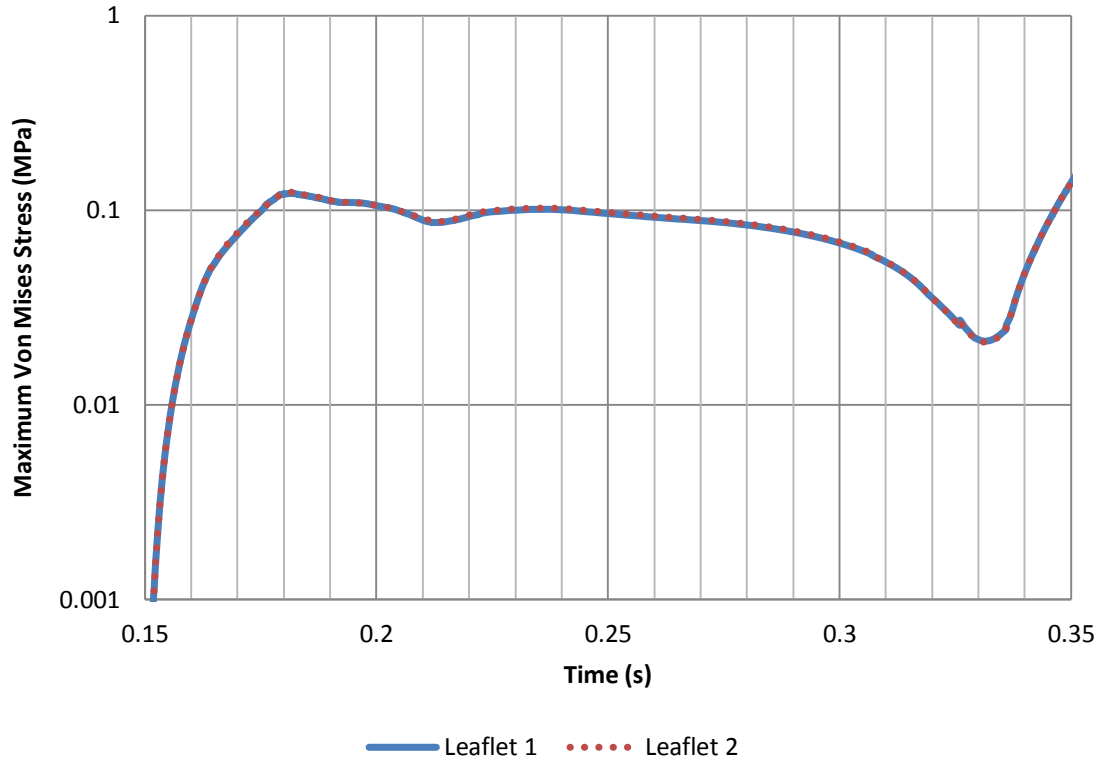
Figure 4.5 Maximum Von Mises Stress within Valve Leaflets for Rigid Wall Tissue Valve Model

4.2 Flexible Wall Bioprosthetic Tissue Valve

By removing the rigid arterial wall assumption applied to computational domain, additional investigation on flexible wall tissue valve model is secondly discussed.

4.2.1 Blood Flow Hemodynamics

The velocity contours for the flexible wall tissue valve are plotted in Figure 4.6 (a) and (b) with the shear stress contour plotted in Figure 4.6 (c) and (d). Similar velocity and shear stress distribution can be found after removing the assumption of rigid wall. The maximum velocity at $0.23\ s$ is slightly lower than rigid wall model given that the flow is ejecting at the center of the computational domain through intervalvular space. There is no significant recirculating flow within aortic root during this period given that only two

vortices are generated closer to aorta located near the side of aortic sinus. The shear stress distribution is also similar to rigid wall model given that the maximum magnitude of shear stress is approximately $357\ dPa$, which is also slightly lower than rigid wall model. At $0.35\ s$ during valve closure, the maximum velocity, with a magnitude of $1.0\ m/s$, is slightly higher than the rigid wall model due to the contraction of flexible wall. The vortices centers generated during peak-opening phase are suppressed and translated toward to the base of aortic sinus such that simple flow is generated with minimum vortices. Since velocity is higher and arterial wall is contracting during this period, the shear stress is also slightly higher with an approximate magnitude of $226\ dPa$ located at the tip of valve leaflet. Overall, the are only minor differences between rigid wall and flexible wall tissue valve models since arterial wall only experiences minimum deformation due to initial condition and computational constraints.

(a) 0.23 s

(c) 0.23 s

(b) 0.35 s

(d) 0.35 s
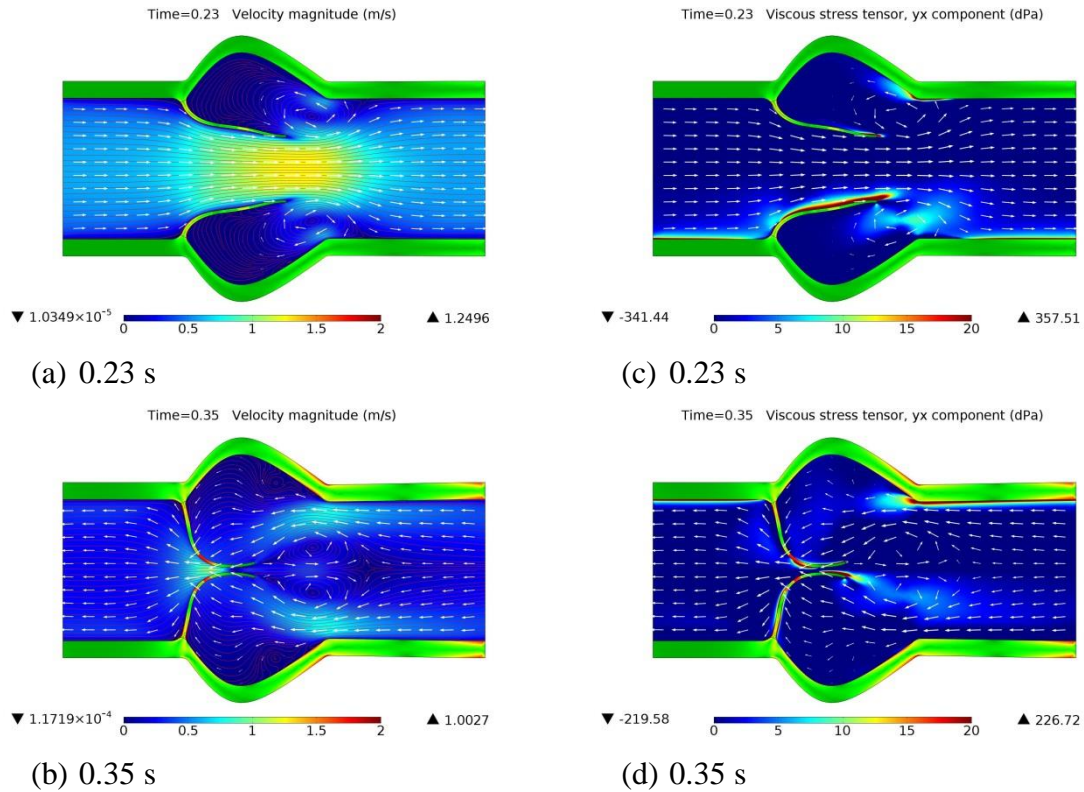
Figure 4.6 Isolated Time Frames during Different Cardiac Phases for Flexible Wall Tissue Valve

In addition to the velocity and shear stress contour plots shown above, the exact downstream velocity for peak-opening and end-opening period is plotted in Figure 4.7. Comparing with the results from rigid wall model discussed above, the peak downstream velocity is slightly smaller for flexible wall model with a magnitude of $1.02\ m/s$ at $0.23\ s$. The ejection width, defined by the diameter of central velocity jet, is approximately the same with a magnitude of $15\ mm$, comparing with rigid wall model. Given that the velocity within aortic root is approximately zero, recirculating flow is not presented at $8\ mm$ downstream, given that this is the widest cross section of computational domain. At $0.35\ s$ during leaflets final closure, the back flow velocity is larger than the rigid wall model with a peak velocity of $-0.4\ m/s$. Unlike the rigid wall model, there is no significant recirculation generated during this period; however, small back flow due to negative pressure is presented within aortic sinus.
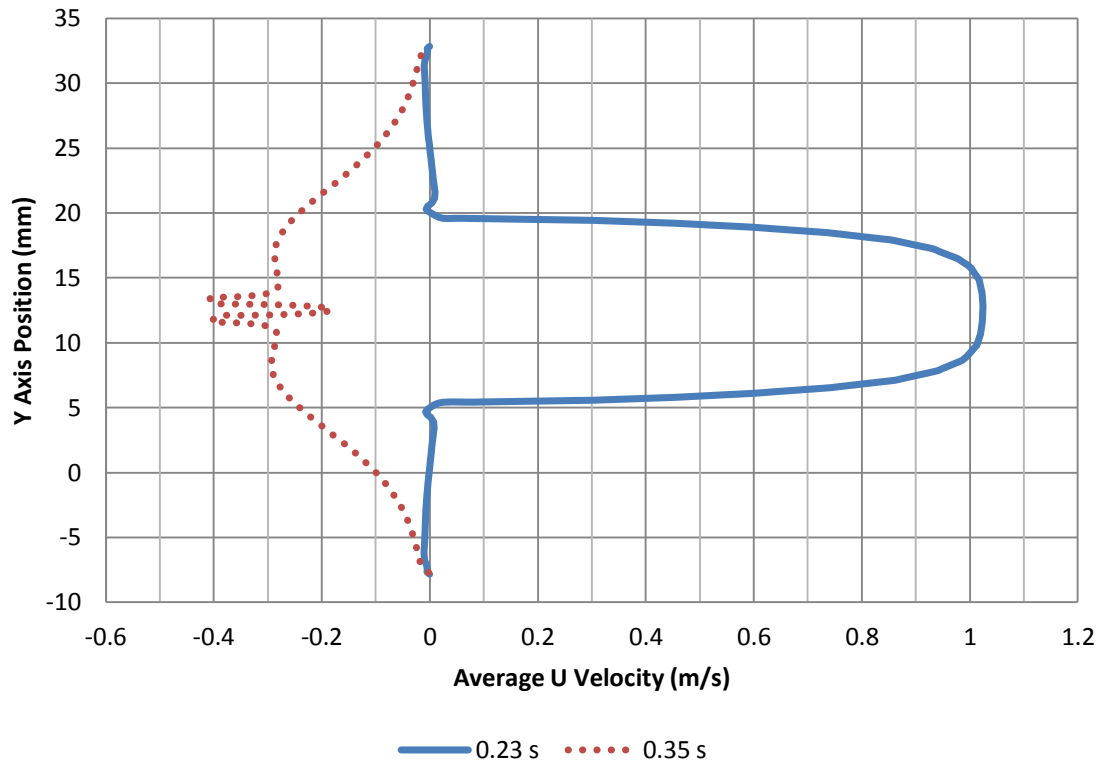
Figure 4.7 Velocity Distribution at $8\ mm$ Downstream for Flexible Wall Tissue Valve

Regarding the generation of shear stress along arterial wall, the maximum shear stress throughout the systolic period is shown in Figure 4.8. Similar to the results presented for the flexible mechanical valve, the shear stress profiles calculated have some degree of oscillatory and unsteadiness behavior due to the motion of both tissue valve leaflets and flexible arterial wall under pulsatile pressure. The maximum shear stress during the simulated period has a magnitude of approximately 500 dPa, which is relatively similar to rigid wall model. Given the magnitude of shear stress is smaller than the critical limit before blood cell damaging, the hemodynamic performance for the tissue valve during systolic period is indeed better than mechanical valve.
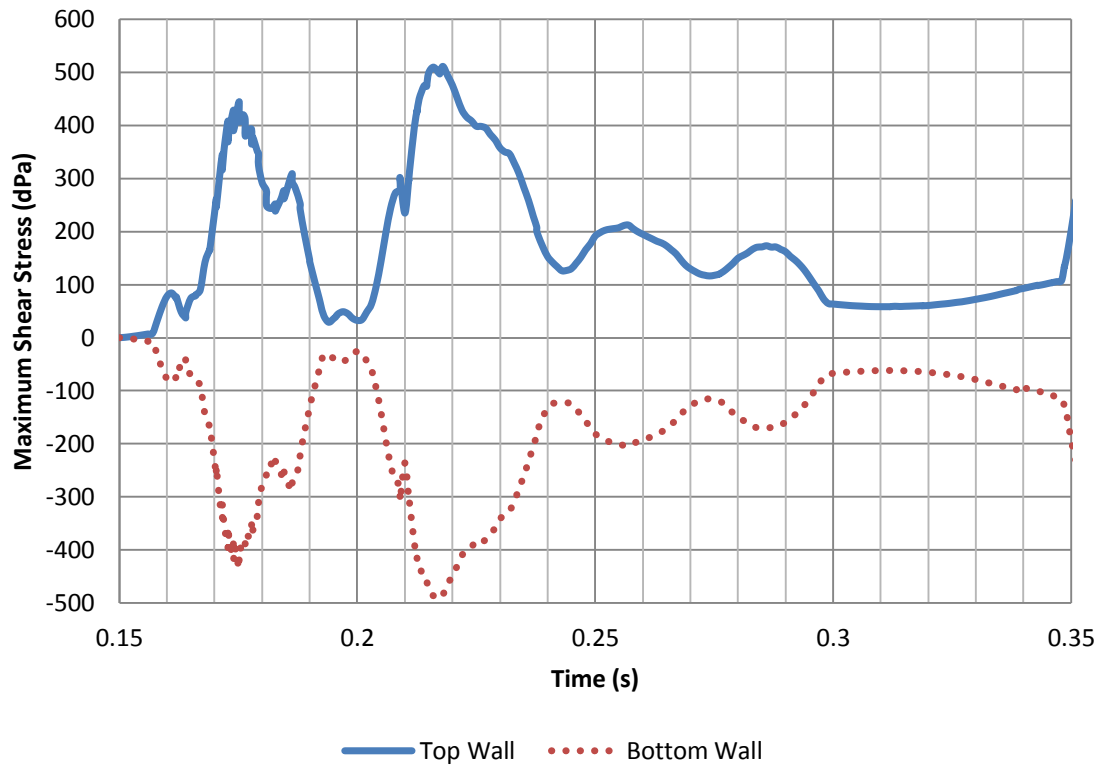
Figure 4.8 Maximum Shear Stress Along Aortic Wall for Flexible Wall Tissue Valve Model

4.2.2 Tissue Valve Leaflet Dynamics

Similar methodology used to process rigid wall tissue valve model can be applied for the flexible walls in order to analysis the leaflet dynamic. Maximum leaflet displacement relative to the center of the domain is shown in Figure 4.9. The maximum displacement of the leaflet is found at $0.2\ s$ with a displaced magnitude of $9\ mm$ away from center. The duration for leaflets to reach the peak opening is approximately $50\ ms$. The leaflets remain open for approximately $100\ ms$ until $0.3\ s$ with an approximate average displacement of $5\ mm$. In addition, the closure of the leaflet takes about $50\ ms$ before the end of the systolic period at $0.35\ s$. Nevertheless, the overall leaflet dynamics profile also has oscillatory behavior if compared with the rigid wall model.
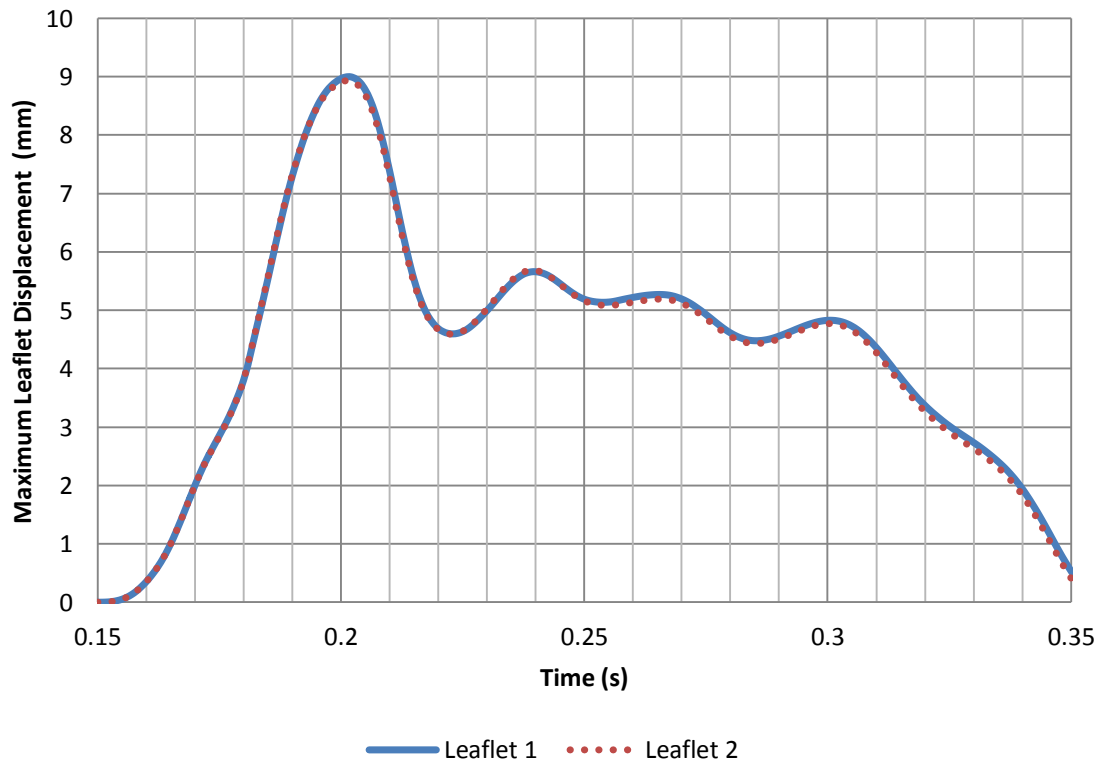
Figure 4.9 Flexible Wall Tissue Valve Leaflet Dynamics

Nevertheless, maximum von Mises stress is plotted in Figure 4.10 in order to investigate the structure behavior for flexible tissue valve. The magnitude for maximum stress during systolic period is roughly 0.1 MPa from $0.17\ s$ to $0.28\ s$. The peak maximum stress during the systolic period is approximately $0.154\ MPa$ at valve closure; however, as mentioned previously, the maximum von Mises stress would be greater when two leaflets are in contact during diastolic period. Overall, only minor differences are observed for the comparison of maximum von Mises stress between rigid wall and flexible wall tissue valve model. Given that both models have only systolic period simulated with minor changes on modeling parameters, minor differences between two models are expected. In order to improve and differentiate between rigid wall and flexible wall models, diastolic period may be included in the future since the back pressure may potentially affect arterial wall motion further.
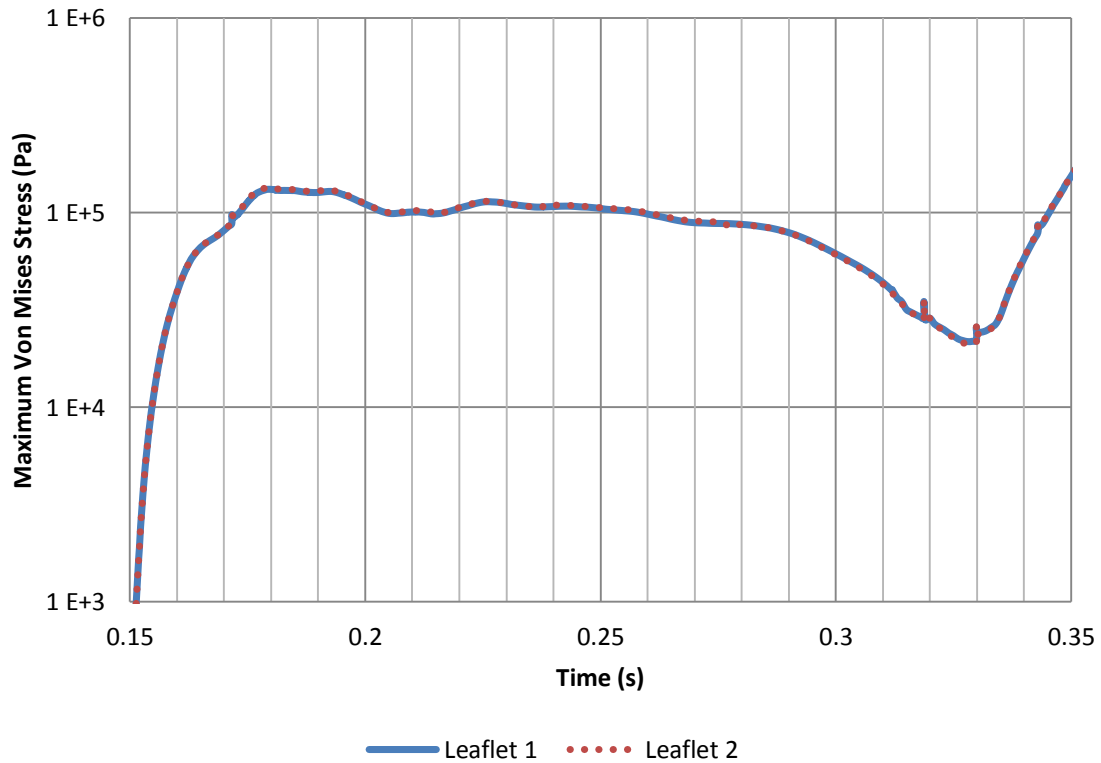
**Figure 4.10 Maximum Von Mises Stress within Valve Leaflets for Flexible Wall Tissue Valve Model**

4.3   Clinical Application

In order to extend the tissue valve model further such that clinical relevant problems can be investigated, the presented model can be modified with the change of tissue valve leaflets material properties. With the increase of tissue stiffness, aortic sclerosis due to valve leaflet calcification can be simulated. Since the models presented previously are simulating a healthy tissue valve with a tissue stiffness that is representing a general upper limit of approximately $2\ MPa$, any increase of stiffness above the limit would potentially leads to some degree of aortic sclerosis or stenosis.

With the healthy leaflet stiffness of $2\ MPa$ as baseline comparison, four additional leaflet stiffness configurations are investigated. Since most parameters in biological system have large variant, the additional stiffness configurations are segregated proportionally to be $4\ MPa$, $5\ MPa$, $10\ MPa$, and $20\ MPa$ in order to characterize minor, moderate, and severer sclerosis. The results for average velocity at $0.23\ s$ with all five configurations are shown in Figure 4.11 using the modified model with rigid wall assumption. Given that there is no significant difference between rigid and flexible wall model, rigid wall assumption is selected to reduce computational resource. The maximum velocity, as expected, are slightly higher for the minor, with leaflet stiffness of $4\ MPa$ and $5\ MPa$, and moderate sclerosis, with leaflet stiffness of $10\ MPa$. The maximum velocity for the severer sclerosis, however, is lower than the healthy configuration. This difference in maximum velocity is caused by the change in flow ejection width that is directly related to leaflet stiffness. Comparison for the ejection width can be done between each severity against the healthy model, which has a width of $15\ mm$, the minor, moderate, and severer sclerosis has a width of $12.5\ mm$, $10.5\ mm$, and $9.2\ mm$, respectively. Given that the difference in average peak velocity between each severity is limited, if assuming the volumetric flow rate is purely depend on the cross sectional area, which could be approximated using the ejection width, the cardiac output in percentage at the isolated time of $0.23\ s$, comparing with the healthy model, would be 69.4%, 49%, and 37.6% for minor, moderate, and severer sclerosis, respectively. Therefore, if flow profile is captured with imaging techniques, such as Doppler ultrasound, for patient with potential sclerosis,

the presented model may be used as a guideline on identifying level of severity more accurately.
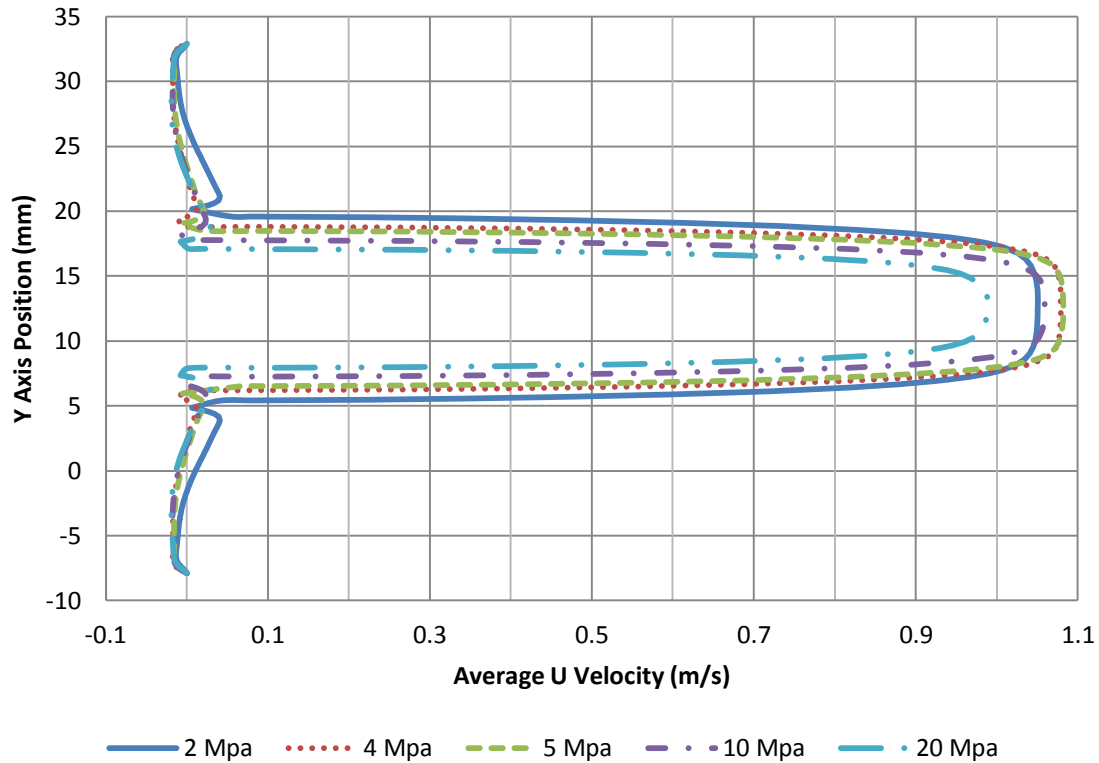
Figure 4.11 Average U Velocity at 0.23 s for Rigid Wall Tissue Valve with Different Valve Stiffness

In addition to the investigation on average velocity at peak-opening phase, the maximum leaflet displacement for each valve stiffness configuration can also be plotted, shown in Figure 4.12. Known that with the increase of leaflet stiffness would decrease leaflet deformation and displacement, the peak leaflet displacement for each model is $9.55\ mm$, $7.65\ mm$, $7.42\ mm$, $5.94\ mm$, and $5.29\ mm$ for the leaflet with stiffness of $2\ MPa$, $4\ MPa$, $5\ MPa$, $10\ MPa$, and $20\ MPa$, respectively. Also note that due to the increase of valve leaflet stiffness, the amount of time required for leaflet to reach maximum opening is decreasing from $0.2\ s$ to $0.186\ s$ for healthy model to severe

sclerosis. Moreover, the increase of valve leaflet stiffness also has an effect on the time of leaflet closure. The more sever the sclerosis is, the shorter systolic period would be. As shown in Figure 4.12, the final closure time for systolic period is decreased from $0.35\ s$ to $0.317\ s$ for healthy model to sever sclerosis.
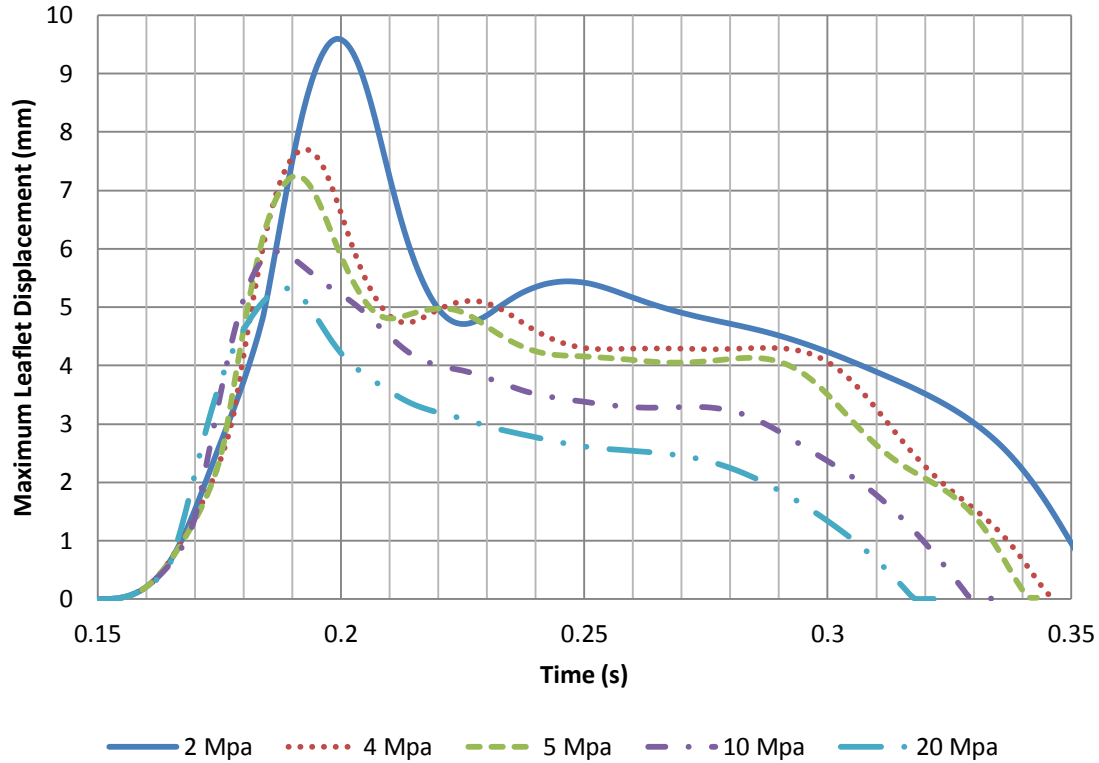
Figure 4.12 Leaflet Dynamics for Rigid Wall Tissue Valve with Different Valve Stiffness

Nevertheless, with the freedom to modify tissue properties, the flexible wall tissue valve can also be modified in order to investigate the effect of valve leaflet stiffening. The results for different leaflet stiffness with a healthy arterial wall are revealing difference in leaflet dynamics shown in Figure 4.13. Given that the healthy model with a prefix of "W20 V2 MPa", which stands for wall stiffness of 20 MPa and valve stiffness of 2 MPa, as baseline for comparison; a stiffer leaflet is showing suppression in leaflet displacement

oscillation. Due to the suppression of leaflet motion, vortices would potentially be suppressed such that flow transition and the recirculation of blood flow would be minimalized such that hemodynamic performance could drop and particle deposition might occur.
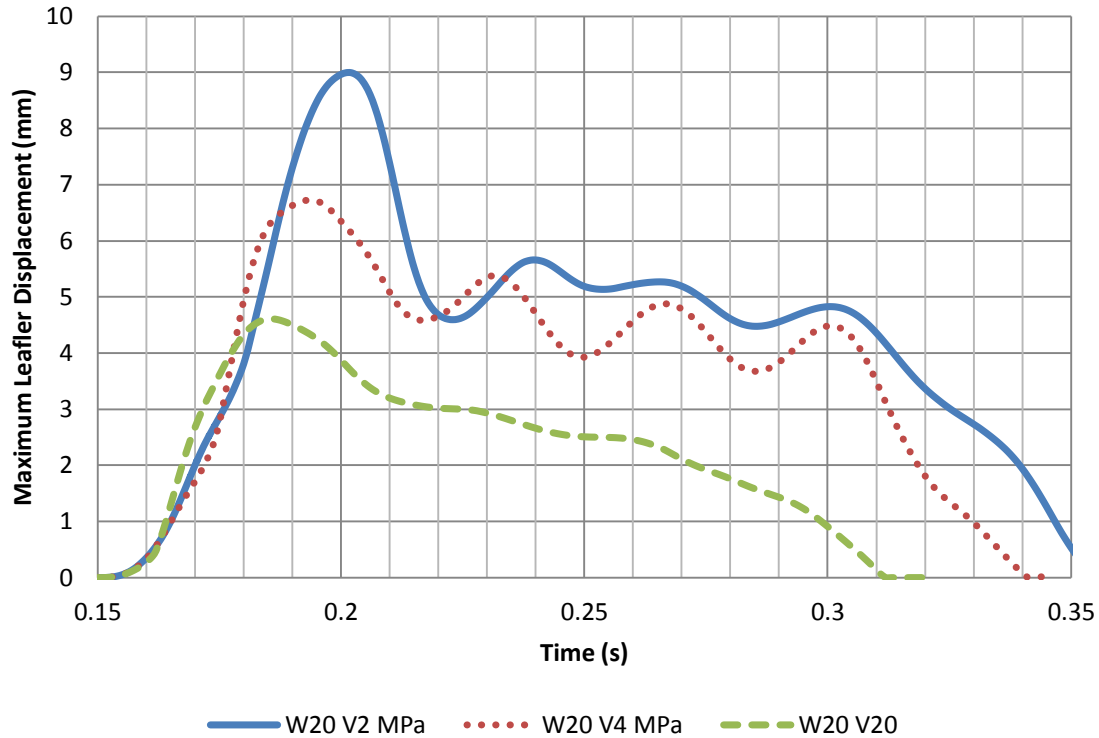
Figure 4.13 Leaflet Dynamics for Flexible Wall Tissue Valve with Different Tissue Stiffness

On the other hand, the stiffness of arterial wall can be adjusted with a healthy valve in order to investigate the effect of arterial wall stiffening, showing in Figure 4.14. Given that the healthy model of W20 V2 MPa is the comparison baseline, the arterial wall is either softening to 10 MPa or hardening to 40 MPa. With a less stiff arterial wall, indicated by W10V2 MPa, the leaflet motion appears to be more flexible as the displacement and oscillation is larger when comparing with healthy model. As expected, for a stiffer arterial wall, indicated by W40 V2 MPa, the tissue valve leaflet has less oscillations. Interestingly, the closure time of the tissue valve, as indicated in Figure 4.13

and Figure 4.14, is affected by the stiffness of valve leaflet instead of the stiffness of arterial wall. Nevertheless, the oscillations of valve leaflet are affected more by the stiffness of arterial wall instead of the stiffness of valve leaflet.
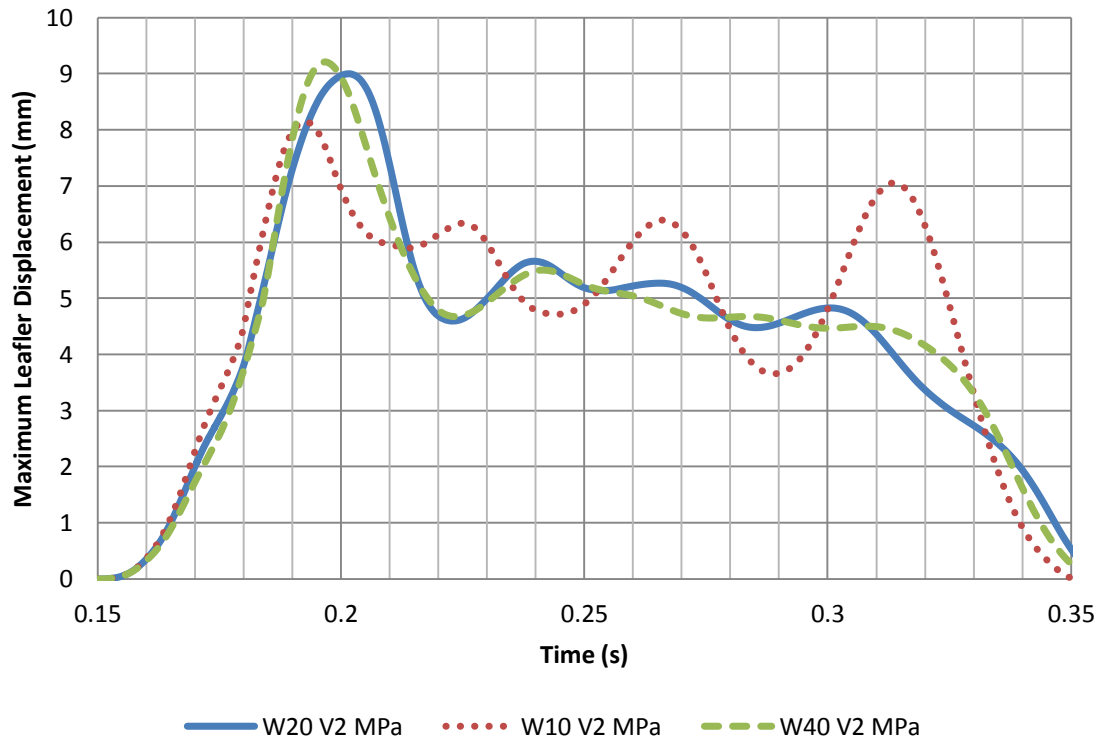
Figure 4.14 Leaflet Dynamics for Flexible Wall Tissue Valve with Different Wall Stiffness

**4.4	Chapter Summary**

In summary, two FSI models for bioprosthetic tissue valve are presented in this chapter, one with the assumption of rigid wall and the other with flexible walls. Based on the calculated velocity profile and shear stress distribution, the tissue valve indeed has a better hemodynamic performance than the bileaflet mechanical valve model presented in Chapter 3. Given the result presented for systolic period, the shear stress along the wall boundary is smaller than the critical value before blood cell damage; however, due to the computational restrictions, results during diastolic period cannot be calculated. In addition to the healthy models presented, investigations regarding the change in tissue properties are also conducted. It can be concluded that the increase in tissue stiffness would decrease hemodynamic performance dramatically as aortic sclerosis would lead to aortic stenosis. Moreover, the stiffening of arterial wall would suppress the generation of vortices by suppressing the oscillatory behavior of leaflet motion, which may lead to the decrease in blood recirculation and particle deposition. In addition, the stiffening of valve leaflet would lead to early valve closure and decrease valve performance. Therefore, the changes in tissue properties, either for arterial wall or valve leaflet, have a major impact on the hemodynamic performance for bioprosthetic tissue valve.

Chapter 5

Future Work and Conclusion

With the FSI models for both bileaflet mechanical valve and bioprosthetic tissue valve discussed in previous two chapters, the concluding remarks regarding the overall research objectives will be summarized. In addition, several computational constraints and limitations that are applicable to present models will be presented. Nevertheless, the future work that could be done in order to extend the present model further, including the improvement and limitations, will also be briefly discussed.

5.1   Conclusion

In conclusion, as the primary objective for this study is to construct a CFD model using FSI method in order to evaluate the hemodynamics of artificial heart valve in idealized aortic root geometry, four different FSI models are built in order to investigate the hemodynamic performance for both mechanical and tissue valve. With the secondary objective on verifications and validations, PIV experiments at ViVitro Lab are conducted in order to compare the constructed models using experimental data. In addition, the tertiary objective is to investigate clinically related issues with proposed models; several additional modifications are imposed such that clinical concerns can be addressed. Furthermore, numerical experiments are also conducted for each type of artificial heart valve in order to investigate the influence of the tissue properties to the hemodynamics around aortic valve. More specifically, the increase tissue stiffness, which leads to aortic sclerosis, results in different degrees of aortic stenosis.

5.2   Contributions

The following list summarizes the key contributions from this study:

- A fluid-structure algorithm with a fully-coupled, monolithic direct solver is used with large structure deformations handled by arbitrary Lagrangian-Eulerian formulation to increase model stability and accuracy.

- The additions of flexible arterial wall to the FSI models have found significant differences comparing with the rigid wall assumption.

- Results from simulations are validated with PIV experiments conducted by ViVitro Lab given that a minimum difference of 15% is found between the simulated results and experimental data.

- Clinical relevant scenarios are conducted for valve malfunction and aortic sclerosis. It is found that leaflet closure and oscillations depended on valve stiffness and wall stiffness, respectively.

- Parameters, such as shear stress, von Mises stress, and leaflet dynamics, are analysed for hemodynamic performance assessment and evaluation.

5.3   Clinical Aspects

The clinically related issues regarding the complications found in artificial heart valve are simulated with the FSI model constructed in this study. The achievements in the investigation of clinically relevant scenarios and the potential usage of current model for future work are listed as follows:

- Mechanical valve malfunction

    Patients received an artificial valve replacement would likely to have pannus formation around the implanted valve that may cause valve malfunction. It is found in the simulated models that a large vortex can be generated due to uneven opening of mechanical valve leaflets. The generated vortex can potentially cause additional complications that affect the accuracy of diagnosis.

- Bioprosthetic valve stiffness

    The changes in tissue stiffness for both valve leaflet and arterial wall have found that the stiffness of the valve leaflet alone would affect the time and duration of

valve leaflet opening. On the other hand, the stiffness of arterial wall alone would affect the oscillation and instability generated by the valve leaflets during systole. The investigations on clinically relevant cases have demonstrated both geometrical and material dependency on the hemodynamic performance of artificial heart valves.

- Patient-specific modeling

  Since computerized tomography (CT) scan is often used for visualizing the three dimensional structure of specific anatomical parts of a patient, the structure reconstructed from the scan can be transferred into a 3D patient-specific model, which can be integrated with current models in order to evaluate the hemodynamic performance for different types of artificial valve for different patients. The simulated result from the modeling of artificial valve can be used as an input parameter for the 3D reconstructed geometry in order to conduct further simulation on the effect of implanted valve.

- Artificial heart valve selection

  Currently, the artificial heart valve selection procedure for patients requires heart valve replacement is based on the patients' age and daily activities. Given that patients with higher age would have a relative higher risk of having a heart valve surgery, the selection procedure made by patients and surgeons is heavily based on the age of patients. With computational methods and patient-specific modeling, better predictions can be made based on the results of hemodynamic performance simulated.

- Additional suggestions and guidance

  Given that many types of data are collected from the FSI simulations, additional guidance and communication between clinicians and researchers can be established by compiling and translating information across different disciplines. For instance, the magnitude of shear stress along the wall boundaries of aortic root may provide guidance for anticoagulant intake. Also, velocity field and vortices formation from the simulated result may provide suggestions on artificial valve damage or flow regurgitation.

5.4   Model Constraints and Limitations

There are several key limitations regarding the computational models presented in this study listed as follows:

- Imposed zero initial condition introduces additional transition
- Frictionless joint for mechanical valve provides a free rotational pivot
- Blood properties are assumed to be Newtonian without considering shear thinning behavior
- Automatic re-mesh, required by large deformation, introduces additional interpolation
- Aortic wall properties are assumed to be isotropic elastic without considering viscoelastic behavior
- Computational domain requires to maintain continuous
- Curvatures of aortic root and tissue valve may not reflect all cases

5.5   Future Work

There are some additional improvements and applications that can be done to the current model, such as model improvement, design optimization, and patient-specific application.

In order to improve the current model, it is possible to eliminate several limitations discussed in precious section. For example, it is possible to extend the simulated time from one cardiac cycle to multiple cardiac cycles such that the effects from initial conditions could be minimalized. Also, the pivots for mechanical valve leaflet are constrained with applied moment when maximum and minimum leaflet angles are reached; an additional formulation can be integrated into the equation in order to account for frictional force. In addition, the topography for tissue valve can be parameterized such that the model can represent various types of valve. Nevertheless, the existing tissue valve model can easily be modified to investigate hemodynamics of transcatheter valve. Finally, the model can be transformed into 3D such at the solution along three axis can be calculated.

As the models presented in this study fully coupled the fluid and structure domain, a design optimization can be conducted. As most physical parameters are known or can be calculated as the result of FSI model, the structure of the artificial valve can be improved by redesigning the leaflet curvatures such that the flow resistance during valve opening can be minimalized. In addition, stress distribution within artificial valve leaflets can be used for the investigation of fatigue and fracture analysis.

Nevertheless, with the newly introduced transcatheter valve available as another surgical option, several clinically related cases for transcatheter valve can be investigated. Specifically, there are needs for improving the understanding of intervalvular leakage between the native or the implanted valve and the transcatheter valve. In addition, the selection guideline on valve size for transcatheter valve is yet to be determined.

Bibliography

[1] Rizzoli, G., Guglielmi, C., Toscano, G., Pistorio, V., Vendramin, I., Bottio, T., et al. (1999). Reoperations for acute prosthetic thrimbosis and pannus: an assessment of rate, relationship and risk. *Europen Journal of Cardio-thoracic Surgery, 16*, 74-80.

[2] Image retrieved from National Heart, Lung, and Blood Institute, U.S. Department of Health & Human Services, http://www.nhlbi.nih.gov/health/health-topics/topics/hhw/anatomy.html, Accessed on Aug 09, 2013

[3] Gott, V., Alejo, D., & Cameron, D. (2003). Mechanical heart valves: 50 years of evolution. *Ann Thorac Surg, 76*, S2230-9.

[4] Dasi, L., Simon, H., Sucosky, P., & Yoganathan, A. (2009). Fluid mechanics of artificial heart valves. *Clinical and Experimental Pharmacology and Physiology, 36*, 225-237.

[5] Grunemeier, G., Naftel, D., & Starr, A. (2000). Long-term performance of heart valve prostheses. *Curr Prpbl Cardiol, 25*, 76-154.

[6] Sun, J., Davidson, M., Lamy, A., & Eikelboom, J. (2009). Antithrombotic management of patients wth prosthetic heart valves: current evidence and future trends. *Lancet, 374*, 565-79

[7] Pibarot, P., & Dumesnil, J. (2009). Prosthetic heart valves: selection of the optimal prosthesis and long-term management. *Circulation, 119*, 1034-1048.

[8] Image retrieved from the Website of St. Jude Medical, http://www.sjmprofessional.com/Products/US/Heart-Valve-Replacement/St-Jude-Medical-Masters-HP-Series.aspx, Accessed on March 14, 2013

[9]   Kouchoukos, N., Masetti, P., Nickerson, N., Castner, C., Shannon, W., & Davila-Roman, V. (2004). The Ross procedure: long-term clinical and echocardiographic follow-up. *Ann Thorac Surg, 78*, 773-81.

[10]   Rahimtoola, S. (2003). Choice of prosthetic heart valve for adult patients. *JACC, 41*, 893-904

[11]   Weber, A., Noureddine, H., Englberger, L., Dick, F., Gahl, B., Aymard, T., et al. (2012). Ten year comparison of pericardial tissue valve versus mechanical prostheses for aortic valve replacement in patients younder than 60 years of age. *J Thorac Cardiovasc Surg, 144*, 1075-83.

[12]   Liao, J., Joyce, E., Merryman, W., Jones, H., Tahai, M., Horstemeyer, M., et al. (2012). The intrinsic fatigue mechanism of porcine aortic valve extracellular matrix. *Cardiovascular Engineering and Technology, 3*, 62-72.

[13]   Image retrieved from the Website of St. Jude Medical, http://www.sjmprofessional.com/Products/US/Heart-Valve-Replacement/Trifecta-Valve.aspx, Accessed on March 14, 2013

[14]   Leon, M., Smith, C., Mack, M., Miller, C., Moses, J., Svensson, L., et al. (2010). Transcatheter aortic-valve implantation for aortic stenosis in patients who cannot undergo surgery. *N Engl J Med, 363*, 1597-1607.

[15]   Rodés-Cabau, J., Webb, J., Cheung, A., Ye, J., Dumont, E., Feindel, C., et al. (2012). Transcatheter aortic valve implantation for the treatment of severe symptomatic aortic stenosis in patients at very high or prohibitive surgical risk. *JACC, 55*, 1080-90.

[16]   Webb, J., Altwegg, L., Boone, R., Cheung, A., Ye, J., Lichtenstein, S., et al. (2009). Transcatheter aortic valve implanttion impact on clinical and valve-related outcomes. *Circulation, 119*, 3009-3016.

[17] Image retrieved from the Website of Medtronic, http://wwwp.medtronic.com/newsroom/content/1260980989058.high_resolution.jpg, Accessed on March 14, 2013

[18] Iung, B., Baron, G., Butchart, E., Delahaye, F., Gohlke-Ba˙rwolf, C., Levang, O., et al. (2003). A prospective survey of patients with valvular heart disease in Europe: the Euro heart survey on valvular heart disease. *European Heart Journal, 24*, 1231-1243.

[19] Gorlin, R., & Gorlin, S. (1951). Hydraulic Formula for Calculation of the Area of the Stenotic Mitral Valve, Other Cardiac Valves, and Central Circulatory Shunts. American Heart Journal. *American Heart Journal, 41*, 1-29.

[20] Segal, J., Lerner, D., Miller, C., Mitchell, R., Alderman, E., & Popp, R. (1987). When should doppler-determined valve area be better than the Gorlin formula?: variation in hydraulic constants in low flow states. *JACC, 9*, 1294-1305.

[21] Burwash, I., Thomas, D., Sadahiro, M., Pearlman, A., Verrier, E., Thomas, R., et al. (1994). Dependence of Gorlin formula and continuity equation valve area on transvalvular volume flow rate in valvular aortic stenosis. *Circulation, 89*, 827-835.

[22] Burwash, I. (2007). Low-flow, low-gradient aortic stenosis: from evaluation to treatment. *Curr Opin Cardio, 22*, 84-91.

[23] Blais, C., Burwash, I., Dumesnil, J., Loho, N., Rader, F., Baumgartner, H., et al. (2006). Projected valve area at normal flow rate improves the assessment of stenosis severity in patients with low-flow, low-gradient aortic stenosis: the multicenter TOPAS(Truly or Pseudo-Severe Aortic Stenosis) study. *Circulation, 113*, 711-721.

[24] Chambers, J., Springings, D., Cochrane, T., Allen, J., Morris, R., Black, M., et al. (1992). Continuity equation and gorlin formula compared with directly observed orifice area in native and prosthetic aortic valves. *Br Heart J, 67*, 193-199.

[25] Grigioni, M., Daniele, C., Del Gaudio, C., Morbiducci, U., Balducci, A., D'Avenio, G., et al. (2005). Three-dimensional numeric simulation of flow through an aortic bileaflet valve in a realistic model of aortic root. *ASAIO Journal, 51*, 176-183.

[26] Dwyer, H., Matthews, P., Azadani, A., Jaussaud, N., Ge, L., Guy, T., et al. (2009). Computational fluid dynamics simulation of transcatheter aortic valve degeneration. *Interact Cardiovasc Thorac Surg, 9*, 301-308.

[27] Dwyer, H., Matthews, P., Azadani, A., Ge, L., Guy, T., & Tseng, E. (2009). Migration forces of transcatheter aortic valve in patients wth noncalcific aortic insufficiency. *J Thorac Cardiovasc Surg, 138*, 1227-33.

[28] Hsu, C. (2009). A study of sewing ring geometry on wall shear stress of implanting bi-leaflet aortic valves, using computational fluid dynamics. *Journal of Mechanics, 25*, 323-333.

[29] Sirois, E., & Sun, W. (2010). Computational evaluation of platelet activation induced by bioprosthetic heart valve. *Artificial Organs, 35*, 157-165.

[30] Sun, W., Li, K., & Sirois, E. (2010). Simulated elliptical bioprosthetic valve deformation: implicatons for asymmetric transcatheter valve deployment. *Journal of Biomechanics, 43*, 3085-3090.

[31] Dasi, L., Ge, L., Simon, H., Sotiropoulos, F., & Yoganathan, A. (2007). Vorticity dynamics of a bileaflet mechanical heart valve in an axisymmetric aorta. *Physics of Fluids, 19*, (067105)1-17.

[32] Sotiropoulos, F., & Borazjani, I. (2009). A review of state-of-the-art numerical methods for simulating flow through mechanical heart valves. *Med Bio Eng Comput, 47*, 245-256.

[33] Dimakopoulos, Y., Bogaerds, A., Anderson, P., Hulsen, M., & Baaijens, F. (2012). Direct numerical simulation of a 2D-stented aortic heart valve at

physiological flow rates. *Computer Methods in Biomechanics and Biomedical Engineering, 15*, 1157-1179.

[34] De Tullop, M., Pedrizzetti, G., & Verzicco, R. (2011). On the effect of aortic root geometry on the coronary entry-flow after a bileaflet mechanical heart valve implant: a numerical study. *Acta Mech, 216*, 147-163.

[35] Borazjani, I. (2013). Fluid-structure interaction, immersed boundary-finite element method simulations of bio-prosthetic heart valves. *Comput. Methods Appl. Mech. Engrg.*

[36] Luo, H., Mittal, R., Zheng, X., Bielamowicz, S., Walsh, R., & Hahn, J. (2008). An immersed-boundary method for flow–structure interaction in biological systems with application to phonation. *J Comput Phys., 227*, 9303–9332.

[37] Hong, T., Choi, C., & Kim, C. (2009). Characteristics of hemodynamics in a bileaflet mechanical heart valve using implicit FSI method. *PWASET, 37*, 679-684.

[38] Dumont, K., Vierendeels, J., Kaminsky, R., Van Nooten, G., Verdonck, P., & Bluestein, D. (2007). Comparison of the hemodynamic and thrombogenic performance of two bileaflet mechanical heart valves using a CFD/FSI model. *J Biomech Eng, 129*, 558-565.

[39] Redaelli, A., Bothorel, H., Votta, E., Soncini, M., Morbiducci, U., Del Gaudio, C., et al. (2004). 3-D Simulation of the St. Jude medical bileaflet valve opening process: fluid-structure interaction study and experimental validation. *J Heart Valve Dis, 13*, 804-813.

[40] Nobili, M., Morbiducci, U., Ponzini, R., Del Gaudio, C., Balducci, A., Grigioni, M., et al. (2008). Numerical simulation of the dynamics of a bileaflet prosthetic heart valve using a fluid-structure interaction approaches. *J Biomech, 41*, 2539-2550.

[41] Guivier, C., Deplano, V., & Pibarot, P. (2007). New insights into the assessment of the prosthetic valve performance in the presence of subaortic stenosis through a fluid-structure interaction model. *J Biomech, 40*, 2283-2290.

[42] Guivier-Curien, C., Deplano, V., & Bertrand, E. (2009). Validation of a numerical 3-D fluid-structure interaction model for a prosthetic valve based on experimental PIV measurements. *Med Eng Phys, 31*, 986-993.

[43] Choi, C., & Kim, C. (2009). Numerical analysis on the hemodynamics and leaflet dynamics in a bileaflet mechanical heart valve using a fluid-structure interaction method. *ASAIO J, 55*, 428-437.

[44] Makhijani, V., Yang, H., Dionne, P., & Thubrikar, J. (1997). Three-dimensional coupled fluid–structure simulation of pericardial bioprosthetic aortic valve function. *ASAIO J, 43*, M387-M392.

[45] Morsi, Y., Yang, W., Wong, C., & Das, S. (2007). Transient fluid-structure coupling for simulation of a trileaflet heart valve using weak coupling. *J Artif Organs, 10*, 96-103.

[46] Hou, G., Wang, J., & Layton, A. (2012). Numerical methods for fluid-structure interaction - a review. *Commun. Comput. Phys., 12*, 337-377.

[47] Stewart, S., Paterson, E., Burgreen, G., Hariharan, P., Giarra, M., Reddy, V., et al. (2012). Assessment of CFD performance in simulations of an idealized medical device: results of FDA's first computational interlaboratory study. *Cardiovascular Engineering and Technology, 3*, 139-160.

[48] Yeleswarapu, K., Antaki, J., Kameneva, M., & Rajagopal, K. (1995). A mathematical model for Shear-Induced Hemolysis. *Artificial Organs, 19*(7), 576-582

[49] Image retrieved from the Website of ViVitro Lab Inc., http://vivitrolabs.com/, Accessed on March 14, 2013

[50] Tan, F., Torii, R., Borghi, A., Mohiaddin, R., Wood, N., & Xu, X. (2009). Fluid-structure interaction analysis of wall stress and flow patterns in a thoracic aortic aneurysm. *International Journal of Applied Mechanics, 1*(1), 179-199

[51] Hron, J., & Turek, S. (2006). A monolithic FEM/Multigrid solver for ALE formulation of fluid structure interaction with application in biomechanics. *Lecture Notes in Computational Science and Engineering, 52*, 146-170.